Quantum dot-based Entangled-Light Emitting Diodes (E-LED) for quantum relays

Christiana Varnava

Robinson College

University of Cambridge

June 2017

This submitted dissertation is for the degree of

Doctor of Philosophy

Quantum dot-based Entangled-Light Emitting Diodes (E-LED) for quantum relays

Christiana Varnava

Abstract

Sources of entangled pairs of photons can be used for encoding signals in quantum-encrypted communications, allowing a sender, Alice, and a receiver, Bob, to exchange keys without the possibility of eavesdropping. In fact, any quantum information system would require single and entangled photons to serve as qubits. For this purpose, semiconductor quantum dots (QD) have been extensively studied for their ability to produce entangled light and function as single photon sources.

The quality of such sources is evaluated based on three criteria: high efficiency, small multi-photon probability, and quantum indistinguishability. In this work, a simple quantum dot-based LED (E-LED) was used as a quantum light source for on-demand emission, indicating the potential for use as quantum information devices. Limitations of the device include the fine-structure splitting of the quantum dot excitons, their coherence lengths and charge carrier interactions in the structure.

The quantum dot-based light emitting diode was initially shown to operate in pulsed mode under AC bias frequencies of up to several hundreds of MHz, without compromising the quality of emission. In a Hong-ou-Mandel interference type experiment, the quantum dot photons were shown to interfere with dissimilar photons from a laser, achieving high two-photon interference (TPI) visibilities. Quantum entanglement from a QD photon pair was also measured in pulsed mode, where the QD-based entangled-LED (E-LED) was electrically injected at a frequency of 203 MHz.

After verifying indistinguishability and good entanglement properties from the QD photons under the above conditions, a quantum relay over 1km of fibre was demonstrated, using input qubits from a laser source. The average relay fidelity was high enough to allow for error correction for this BB84-type scheme. To improve the properties of the QD emission, an E-LED was developed based on droplet epitaxy (D-E) QDs, using a different QD growth technique. The relevant chapter outlines the process of QD growth and finally demonstration of quantum entanglement from an electrically injected diode, yielding improvements compared to previous E-LED devices.

For the same reason, an alternative method of E-LED operation based on resonant two-photon excitation of the QD was explored. Analysis of Rabi oscillations in a quantum dot with a bound exciton state demonstrated coupling of the ground state $|g\rangle$ and the biexciton state $|XX\rangle$ by the external oscillating field of a laser, therefore allowing the transition between the two states. The results include a considerable improvement in the coherence length of the QD emission, which is crucial for future quantum network applications. We believe that extending this research can find application in quantum cryptography and in realising the interface of a quantum network, based on semiconductor nanotechnology.

Declaration

This dissertation is the result of my own work and includes nothing which is the outcome of work done in collaboration except as declared in the Preface and specified in the text. It is not substantially the same as any that I have submitted, or, is being concurrently submitted for a degree or diploma or other qualification at the University of Cambridge or any other University or similar institution except as declared in the Preface and specified in the text. I further state that no substantial part of my dissertation has already been submitted, or, is being concurrently submitted for any such degree, diploma or other qualification at the University of Cambridge or any other University or similar institution except as declared in the Preface and specified in the text. This dissertation contains less than 65,000 words including appendices, bibliography, footnotes, tables and equations and has less than 150 figures.

Christiana Varnava

2017

Acknowledgements

I am indebted to many people at Toshiba Research Laboratories and the Cavendish Laboratory for their help and expertise. First and foremost, I would like to thank Dr. Mark Stevenson for his guidance and the opportunity to work on the entanglement project. Dr. Andrew Shields and Prof. Richard Penty for supervising and financially supporting this project. Special thanks go to so many researchers at CRL: Joanna & Dave, who taught me how to make my tiny LEDs and gave me advice when fabrication troubles stroke, Ian and Peter for growing so many wafers, Tina, Jan, Anthony and Martin, amongst others, for assisting in various ways.

I must also acknowledge my fellow students, who have been very outgoing and made my time here so enjoyable, especially my cubicle partners Fred and Martin, for all the laughs and useful discussions. Also, thank you to all the lovely people who provided rays of sunshine in cloudy Cambridge with their company; Sin Lih, Antrea & Olympia to name a few, our friendship means a lot to me. And naturally, I would like to say thank you to my parents and my amazing, ever-expanding family for their unconditional love and valuable life lessons; you give meaning to everything I do.

Journal publications

1. '*An entangled-LED-driven quantum relay over 1 km'*
   Npj Quantum Inf., vol. 2, p. 16006, Mar. 2016.
   C. Varnava, R. M. Stevenson , J. Nilsson, J. Skiba-Szymanska, B. Dzurnak, M. Lucamarini, R. V. Penty, I. Farrer, D. A. Ritchie, and A. J. Shields.

2. *'Universal Growth Scheme for Quantum Dots with Low Fine-Structure Splitting at Various Emission Wavelengths'*
   Physical Review Applied
   Joanna Skiba-Szymanska, R. Mark Stevenson, **C. Varnava**, Martin Felle, Jan Huwer, Tina Müller, Anthony J. Bennett, James P. Lee, Ian Farrer, Andrey Krysa, Peter Spencer, Lucy E. Goff, David A. Ritchie, Jon Heffernan, and Andrew J. Shields

Conference proceedings

1. *'Quantum Teleportation with Light-emitting-diodes'*
   Frontiers in Optics 2015, OSA Technical Digest (Optical Society of America, 2015)
   R. M. Stevenson, **C. Varnava**, J. Nilsson, J. Skiba-Szymanska, B. Dzurnak, M. Lucamarini, R. V. Penty, I. Farrer, D. A. Ritchie, and A. J. Shields.

2. *'Growth scheme for quantum dots with low fine structure splitting at telecom wavelengths'*
   Proc. SPIE 10114, Quantum Dots and Nanostructures: Growth, Characterization, and Modeling XIV, 101140O (April 28, 2017)
   Tina Müller, Joanna Skiba-Szymanska, R. Mark Stevenson, **C. Varnava**, Martin Felle, Jan Huwer, Anthony J. Bennett, James P. Lee, Ian Farrer, Andrey Krysa, Peter Spencer, Lucy E. Goff, David A. Ritchie, Jon Heffernan, and Andrew J. Shields

Contributed Talks

1. *'An entangled-LED-driven quantum relay over 1 km',*
   International Conference on Quantum Cryptography, Tokyo 2015
   C. Varnava, R. M. Stevenson, J. Nilsson, J. Skiba-Szymanska, B. Dzurnak, M. Lucamarini, R. V. Penty, I. Farrer, D. A. Ritchie, and A. J. Shields.

Contents

List of Abbreviations

APD	Avalanche Photodiode
B.E.	Binding Energy
BSM	Bell-State measurement
D-E	Droplet Epitaxy
DBR	Distributed Bragg Reflector
E-LED	Entangled-Light Emitting Diode
EPC	Electrical Polarisation Controller
EPR	Einstein-Podolsky-Rosen
FSS	Fine structure splitting
HBT	Hanbury-Brown-Twiss
HWP	Half-wave plate
I.M.	Intensity Modulator
MBE	Molecular beam epitaxy
NV	Nitrogen Vacancy
PBS	Polarising beamsplitter
PNS	Photon number splitting
QBER	Quantum Bit Error Rate
QD	Quantum Dot
QKD	Quantum Key Distribution
S-K	Stranski-Krastanov
SEM	Scanning Electron Microscopy
SNR	Signal-to-Noise ratio
SPDC	Spontaneous Parametric Downconversion
SPS	single photon sources
SSPD	Superconducting single photon detectors
TAC	Time-to-Amplitude Converter
TPE	Two-photon excitation
TPI	Two-photon interference
WL	Wetting Layer
XX, X	Biexciton, Exciton

Chapter 1 Introduction

In the microscopic world, the world of tiny particles like photons, classical principles are not enough to describe the behaviour of matter. Quantum mechanics theory was developed as an attempt to interpret phenomena of this scale that seem to violate fundamental laws of classical physics. The beginning of the last century saw many physicists making contributions in the formulation of this theory: Einstein, Bohr [1], Heisenberg [2] and Schrödinger [3] amongst others. Different schools of thought gave different interpretation of quantum mechanics, with famous debates emerging from the disagreements. *Can the theory of quantum mechanics ever describe nature completely?* [4]. Our intuition about the state of the world supports the idea of local realism; *the moon exists even if we do not look at it*. The Einstein-Podolsky-Rosen trio rejected the idea of a system's physical properties being revealed upon measurement and suggested that a criterion of reality is required instead. For Schrödinger though, the complete knowledge of a whole system does not necessarily include knowledge of all its parts, and suggested that by interaction, systems can be *entangled*. Naively put, the subsystems possess correlated properties and knowledge obtained by measuring one of the subsystems can cause a change in the description of the other. These ideas might seem peculiar or abstract and even Einstein considered entanglement to be "spooky action at a distance" and discussed this "paradox" in the famous Einstein-Podolsky-Rosen paper in 1935 [4]. Putting aside the debates and philosophical implications of the concept at this point, quantum entanglement can actually be exploited for practical operations, opening the way for new fields and applications including quantum computing, cryptography and teleportation [5]. Before studying the phenomenon of entanglement though, we need to look at some basic quantum mechanics concepts.

1.1.1 Quantum bits & Superposition

In a quantum system, a single particle can be in a superposition state $|\Psi\rangle$:

$$|\Psi\rangle = a|0\rangle + b|1\rangle \qquad (1\text{-}1)$$

where a, b are complex coefficients. This simply means that the system has components of two logical states $(|0\rangle, |1\rangle)$ at the same time or is the sum of their probabilities of occurring. If one attempts to

measure a particle in a superposition state, the outcome will be uncertain. There is a probability of getting 0, equal to $|\langle 0||\psi\rangle|^2 = a^2$, or 1, equal to $|\langle 1||\psi\rangle|^2 = b^2$. The mere act of measurement will actually send the particle into one of these logical states and will be irreversible [6]. In quantum theory, the simplest quantum logic gate is defined as the qubit. Just as a classical computer makes operations using memory bits that can be either ones or zeros, a quantum computer manipulates qubits. The state of a qubit can be described by a superposition of ones and zeros, as in (1-1).

A qubit can find implementation in the form of a particle for example, that may be in a superposition of two discrete spin states, or a photon that may be in a superposition of two different polarizations. A two-level system producing discreet states can also supply us with qubits. There is a multitude of methods and material systems available: energy levels of trapped ions [7], nitrogen vacancy (NV) centres in diamond [8], photons from quantum dots [9] or energy levels in semiconducting circuits [10] are some of them. For the purposes of this thesis photons and their polarization were used to define the qubit states.

1.2 Entanglement

In a system with two qubits, each of which can either be in state 1 or 0, we can have four possible states: $|00\rangle, |01\rangle, |10\rangle$ and $|11\rangle$. Following from the superposition principle described above, the quantum state of both qubits can be expressed as the product of the two: $|\Psi\rangle = |\psi_1\rangle \otimes |\psi_2\rangle$ and hence as a linear combination of these states. A superposition state with only two of these logical states can be expressed as:

$$|\Psi\rangle = \frac{1}{\sqrt{2}}(|00\rangle + |11\rangle) \quad (1\text{-}2)$$

Such a state cannot be decomposed as a product of its two constituent qubits. The state is said to be entangled, which means that we cannot consider the qubits as having separate states, but rather a joint one. The above state, which is one of the four Bell states, will maintain the property of entanglement, even if the measurement basis is rotated. It was suggested by John Bell in 1964 that entanglement holds true independently of the spatial separation between the two qubits, with the idea of non-locality [11]. In the same paper, it was also shown that such states can violate the set of relations called Bell inequalities and are incompatible with any local hidden variable theories.

Many experiments since then have proved that Bell's inequalities can be violated and entanglement can be measured [12]. More recently, loophole-free Bell tests have been demonstrated by various groups

[13]–[15] by using well-separated setups and fast apparatus, putting an end to the question of local realism.

Almost a century after it was first introduced, quantum entanglement is at the heart of quantum information science. Applications like quantum computing [16] and quantum cryptography [17] and communication protocols like quantum teleportation, entanglement swapping and superdense coding are based on this illusive property that fundamentally challenges the perception of nature.

1.2.1 Generation of entangled photon pairs

There has been remarkable progress in the development of quantum light sources for quantum communication purposes and various sources of entangled photons, as well as several types of entanglement have been demonstrated. The sources usually rely on optical or electrical excitation and subsequent relaxation of states in a material, an atom, a molecule or a cavity and photons may be entangled in path [18], time [19] or polarisation [20] amongst others.

A typical way of achieving polarisation-entangled photons is by spontaneous parametric downconversion (SPDC) [21]. This refers to the nonlinear process of creating two photons from one pump photon. Using a nonlinear crystal, the pump photon from a laser is split into a pair of photons, whose combined energies and momentum are equal to the energy and momentum of the former. Polarisation entanglement is thus achieved and their individual states are in a superposition. However, the generation of entangled pairs with this method has poissonian characteristics, meaning that multiple pairs may be generated during the same cycle. The generation of more than one pair translates to causing errors when it comes to quantum information applications. Quantum dots in semiconductors are an alternative system of producing entangled pairs of photons that can be engineered to the specific requirements of an application. All the work in this thesis is based on quantum dots, which are explained in detail in section 1.4.

1.3 Quantum Information & Applications

The development of quantum mechanics theory has enabled new fields such as quantum computing and quantum communications to emerge. Computing devices based on the principles of quantum mechanics can provide solutions to tasks that have no efficient solution on a classical computer. Following from the notion of a qubit in 1.1.1, if a quantum computer has n qubits, it can hold a superposition of 2^n states. There exist algorithms where a single quantum computation with an input set to a

superposition could easily outperform a classical one. For instance, Shor's factorization algorithm [22] for factoring large integers, Grover's database search algorithm [23] or Simon's algorithm [24].

Quantum cryptography systems can similarly exploit the laws of quantum mechanics, namely entanglement, to enable unconditionally secure distribution of private information by transferring a quantum state from one node to another. The quantum key distribution protocol (discussed in more detail in 1.7) can enable two parties to communicate securely by allowing private key bits to be distributed between them over a public channel [25].

Quantum communications are expected to be applied to telecommunication applications and next generation networks. Establishing a quantum network consisting of multiple nodes requires distribution of entanglement over a distance. Schemes such as quantum repeaters or relays make use of entanglement, quantum memories and quantum teleportation in order to extend the distance and bit rate of quantum communications [26].

1.4 Photon emission from quantum dots (QDs)

The main focus of this thesis is on developing quantum light sources for use in quantum network applications. An ideal source would emit single photons on-demand, so that information can be encoded and used to generate secret keys, as described in 1.7. Semiconductor QDs are an attractive system for the generation of photonic qubits due to the fact that their excitonic transitions interact efficiently with light. The photonic emission of the dots can be enhanced by embedding them into various structures and devices such as LEDs, micropillars [27], microcavities [28], photonic crystals [29] or microdisks [30]. Features such as photon anti-bunching and discreet energy levels make QDs highly efficient single photon sources (SPS) for quantum information processing applications [31].

Semiconductor QDs are structures of the order of several tens of nanometres, which can confine charge carriers in three dimensions. Confining electrons or holes in a quantum box of finite potential causes their energy levels to have discreet, quantized values [32]. This useful effect has led to the integration of quantum dots in many electronic and photonic devices.

Various material systems exist, depending on application requirements, including: Ge/Si, InAs/GaAs and InP/GaAs. Growth and processing methods in the field have progressed and nowadays QDs can be grown by self-assembly [33], droplet epitaxy (DE) [34], or even by etching quantum well structures [35], amongst other methods. With regards to this project, we have been using Indium Arsenide quantum dots grown on Gallium Arsenide substrates by self-assembly and droplet epitaxy.

1.4.1 Stranski-Krastanov growth

The Stranski-Krastanov (S-K) method is a commonly used technique for growing self-assembled quantum dots. It relies on epitaxial growth, where an epitaxial film is deposited on a substrate of a different material with a smaller lattice constant. This process allows control of deposition at monolayer level.

Molecular beam epitaxy (MBE) can be used to deposit indium and arsenide atoms on a GaAs (001) substrate, in order to form self-assembled dots. The technique is illustrated in Figure 1.1. During the process, the first InAs deposition layers will be strained and will form the wetting layer (WL), as GaAs and InAs are lattice mismatched by 7% [36]. Once a certain thickness threshold is reached, islands will form on top of the wetting layer in order to reduce the strain in the crystal. The islands formed are crystallised into quantum dots by GaAs capping, and can be made very small in dimensions, compared to other growth methods. The art of growth takes many different parameters into account, as growth conditions greatly affect the optical properties of the quantum dots. Careful control over these conditions is required to achieve a certain shape, size, density or confinement potential of the dots.

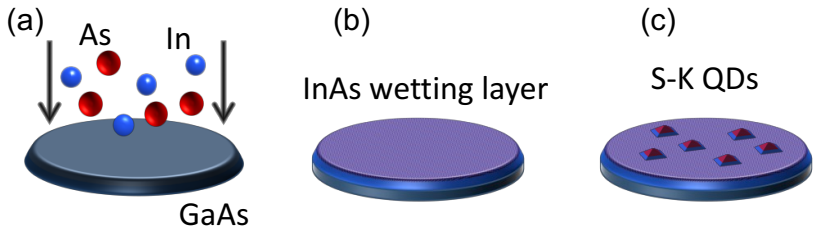

Figure 1.1: Self-assembled growth of quantum dots using MBE for the deposition of InAs on GaAs. (a) InAs is first deposited on a GaAs (001) substrate under vacuum conditions. (b) A strained 2-D layer forms on top because of the lattice mismatch between GaAs and InAs. (c) The strained crystal relaxes as 3D islands to reduce the strain, forming quantum dot structures.

1.4.2 Biexciton Cascade in InAs/GaAs QDs

Single InAs/GaAs quantum dots, grown by MBE as described above, can be excellent sources of entangled-photon pairs. A QD may be represented as a 3-D quantum well, formed using two different semiconductor materials with different bandgaps. The bandgap of InAs (0.42 eV at 0K) is smaller than the bandgap of GaAs (1.52 eV at 0K) [37]. As shown in Figure 1.2, a quantum dot can confine two electrons and two holes in three dimensions (refer to Figure 1.3 for possible carrier confinement configurations). Since the dimensions of a quantum dot are comparable to the de Broglie wavelength of

the carriers, discreet energy levels are formed. The interband transitions are easily probed on a spectrum, as in Figure 1.2 (b); the wetting layer emission is centred around 870nm, whereas the quantised levels of an ensemble of QDs are narrow emission lines around 885nm.

The biexciton cascade system can be excited optically or electrically, in order to study optically active QDs. Using a laser, for instance, we can create carriers in the wetting layer or in the higher QD states under above-band, non-resonant excitation. These will quickly relax into the lowest QD states. If the QD is placed in an LED structure, the creation of carriers occurs by electrical injection of current (see 1.5).

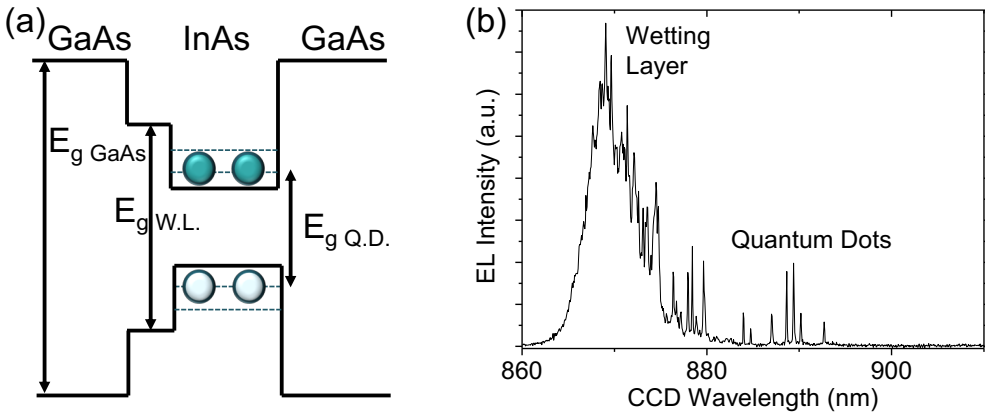

Figure 1.2: (a) Band-level energy diagram of an InAs/GaAs dot. The dot can capture two electrons (dark circles) and two holes (bright circles). The bandgap of GaAs ($E_{g\ GaAs}$=1.52eV). The bandgap of the quantum dot is around 1.40 eV and the bandgap of the wetting layer is slightly higher at 1.44 eV. (b) Emission spectrum of a typical sample grown by S-K MBE, corresponding to the bandgap transitions in (a). Emission from the GaAs layer (around 830nm) has been filtered out.

A schematic of the radiative biexciton cascade is shown in Figure 1.3(a). Once the dot captures two electrons and two holes, it will be in the biexciton state (XX). Recombination between an electron-hole generates the first photon and leaves the system in the exciton state (X). The remaining electron-hole pair recombines so that the second photon is emitted and the system decays to ground state [38]. Determined by the Coulomb interactions between holes and electrons, the exciton and biexciton photons will have different energies. When the quantum dot captures an equal number of electrons and holes, neutral exciton states can be observed, whereas for an unequal number, the transitions become charged. The types of possible transitions are illustrated in Figure 1.3(b).

The photon pair emitted from a single cycle of the cascade is entangled, as dictated by the angular momentum operators of the electrons and holes and their exchange interaction [39]. Depending on the projection of the charge spin on the growth (z) axis, the total z-spin may have four distinct values:

$|\pm 1\rangle$ and $|\pm 2\rangle$. We consider spin values for electrons: $S_e = \pm 1/2$ and for heavy-holes: $J_h = \pm 3/2$ [40]. The light-hole states are neglected in the analysis of self-assembled QDs because of the energy splitting between the energy levels of the heavy and light holes, which is caused by strain. Radiative decay occurs only when the electron and hole have opposite spins and these bright exciton photons are the ones we are interested in. Therefore, preservation of angular momentum dictates that for the degenerate $|\pm 1\rangle$ eigenstates the emitted photons will have σ^+ and σ^- polarisations so that they can be described by the polarisation-entangled state $\frac{1}{\sqrt{2}}(|R_X L_{XX}\rangle + |L_X R_{XX}\rangle)$. In this expression, the two-photon state is described by a superposition of cross-circularly polarised photons, where *R* and *L* represent the right-hand and the left-hand circular polarisations, respectively. In reality, quantum dots are asymmetric in structure and may be elongated along one of the two crystal axes. This introduces a mixing in the electron spin states and the bright exciton eigenstates become $|H\rangle = (|+1\rangle + |-1\rangle)/\sqrt{2}$ and $|V\rangle = (|+1\rangle - |-1\rangle)/\sqrt{2}$ [39]. Consequently, the emission can follow two energetically distinct paths with polarisation parallel to the [110] or [1-10] crystal axis, labelled as H or V in Figure 1.3 (a). The difference in energy between the H and V emission paths is defined as the fine structure splitting (FSS) denoted by s.

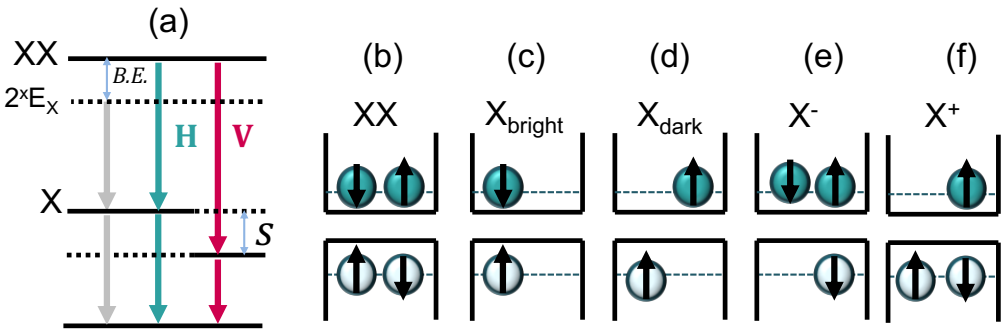

Figure 1.3: (a) The biexciton cascade. The entanglement of the emitted photon pair X and XX is compromised because of the splitting in energy *S* of the two biexciton state decay paths H and V. Binding Energy (B.E) is defined as the spectral difference between an X and an XX photon, which is determined by Coulombic interactions between the confined electrons and holes. B.E. can be either positive or negative. (b)-(f) Possible carrier confinement configurations in a dot. Arrows indicate the carrier spin direction. The biexciton XX state has two electron-hole pairs of opposite spins before the first recombination. After the biexciton photon is emitted, the dot has an electron-hole pair of opposite spins forming the bright exciton state. For parallel-spin carrier recombination, no radiative emission is observed. In the case that the dot captures a free electron or hole, the charged exciton states X^- and X^+ are observed.

1.4.3 Fine-structure splitting & entanglement

As mentioned above, the presence of fine-structure splitting arises from the morphological properties of the quantum dot. The InAs quantum dots may be asymmetric, lifting the degeneracy of the bright exciton level [41] by electron-hole exchange.

The quantum dot is initially in the biexciton state, with two holes and two electrons. Upon the first electron-hole recombination, the biexciton photon is emitted and the state is projected into the superposition $|\Psi^+\rangle = (|H_{XX}|H_X\rangle + |V_{XX}|V_X\rangle)/\sqrt{2}$. At a finite time τ later, the second photon will be emitted and, if the two states are energetically different, they will have a phase difference of $s\tau/\hbar$, so that the state of the entangled photon pair is described by:

$$|\psi\rangle = \frac{1}{\sqrt{2}}(|H_{XX}|H_X\rangle + e^{is\tau/\hbar}|V_{XX}|V_X\rangle), \quad (1\text{-}3)$$

where s is the energy difference between the two states due to the fine structure splitting (FSS) [42], [43]. The superposition has a time-dependent phase $s\tau/\hbar$, while the intensity of the photon pair decays with delay τ. Since the superposition is averaged over τ, the terms with opposite phases cancel out, reducing the observed entanglement. Therefore, the presence of finite *S* will result in reduced entanglement fidelity, which is undesirable for our quantum applications [22], [21].

It is thus important to be able to minimise the FSS in our quantum dots and several strategies have shown that it is possible to tune this parameter. For self-assembled InAs on GaAs quantum dots grown by MBE, there exists a relationship between the mean FSS and the emission wavelength of the excitons, which shows a minimum occurring at 885nm [45]. This approach is undertaken for the dots grown for this project. Naturally, the minimum refers to an ensemble of dots and a variance in the mean FSS exists on our samples. It is also possible to tune the magnitude of the splitting by applying an in-plane magnetic field [46]. Similarly, the FSS can be minimised by applying an external electric field [47], but that would require AlGaAs barriers to be grown in the structure, which are not compatible with an electrically-driven device. Other people have reported applying strain fields [48] and piezoelectric [49] or stress devices [50]. Strain-free quantum dots grown by droplet epitaxy have also demonstrated small FSS [51]. This growth method will be explored in Chapter 5 as well.

1.5 The Entangled-Light Emitting Diode (E-LED)

The future of quantum information applications depends to a great extent on the availability of small and compact optics components and devices required to generate entangled pairs of photons. The E-LED used for the optical experiments in this thesis was developed by Toshiba Research Europe and the Cavendish Laboratory [52]. This was the first demonstration of an electrically-driven, solid-state entangled pair emitter based on quantum dots following from an earlier design from the same group [53]. The simple design has the biexciton cascade from a quantum dot embedded in a p-i-n junction and can generate entangled-photons on demand, as described by Benson et al [54]. Electrical triggering will remove the need for optical pumping using lasers and will enhance the practicality of a large-scale implementation. Up to date, only one more group has recently demonstrated a similar device [55]. The requirements for an ideal source for quantum communication schemes can be summarised as 1) high emission intensity, 2) single-photon character, 3) high photon indistinguishability and 4) high entanglement fidelity. In this context, the crucial parameters that characterise emission and which we will seek to improve are the single photon rates, the $g^{(2)}(\tau)$ function, the coherence time and degree of entanglement of the emission respectively.

1.6 Quantum teleportation

In quantum terms, the operation of copying an unknown quantum state is not possible, as stated by the 'no-cloning' theorem [56]. An equivalent operation, where a qubit is destroyed in order to appear at another location, is fancily termed as quantum teleportation. Any quantum communication scheme would require interacting qubits to be teleported in order to transfer information and build logic gates [57]. Quantum teleportation, first proposed by Bennett et al in 1993 [58], allows transfer of an arbitrary input quantum state between two non-local systems by reconstructing it using non-classical EPR correlations and classical information. Two remote parties, Alice and Bob, share two qubits that are in a maximally entangled state $|\Phi^+{}_{23}\rangle$. Alice also has an input qubit in a state $|\psi_1\rangle = \alpha|H\rangle + \beta|V\rangle$ that she wants to send to Bob. The entire system can be described by $|\psi_1\rangle|\Phi^+{}_{23}\rangle$. She then performs a joint measurement or Bell-state measurement (BSM) on the input qubit and her share of the Bell pair (ancilla photon). The measurement will project the two photons onto one of the four entangled Bell states:

$$|\Phi^{\pm}\rangle = \frac{1}{\sqrt{2}}(|HH\rangle \pm |VV\rangle) \qquad (1\text{-}4)$$

$$|\Psi^{\pm}\rangle = \frac{1}{\sqrt{2}}(|HV\rangle \pm |VH\rangle)$$

The system state at this point can be described by

$$|\Psi_{123}\rangle = (\alpha|H_1\rangle + \beta|V_1\rangle) \otimes \frac{1}{\sqrt{2}}(|H_2H_3\rangle \pm |V_2V_3\rangle) \quad (1\text{-}5)$$

$$= \frac{1}{\sqrt{2}}(\alpha|H_1H_2H_3\rangle + \beta|V_1H_2H_3\rangle + \alpha|H_1V_2V_3\rangle + \beta|V_1V_2V_3\rangle) \quad (1\text{-}6)$$

$$= |\Phi_{12}{}^{\pm}\rangle(\alpha|H_3\rangle \pm \beta|V_3\rangle) + |\Psi_{12}{}^{\pm}\rangle(\alpha|V_3\rangle \pm \beta|H_3\rangle) \quad (1\text{-}7)$$

It is obvious from (1-7) that Alice's choice of one of four measurement bases (first half of the terms) will send Bob's qubit with index 3 in one of four states that can be related to the input by a unitary transformation. Alice's measurement destroys the initial information of the input state $|\psi_1\rangle$ and she can classically inform Bob of the outcome. Note that this fact prevents any faster than light information transmission. Bob can easily recover the initial state by applying the appropriate logical operation on his qubit.

The schematic in Figure 1.4 shows a simple illustration of the experimental implementation of quantum teleportation that will be discussed in Chapter 4. Note that the setup does not allow for a full BSM, namely not all four Bell states can be distinguished by measurement. In fact, it is impossible to detect all four Bell states using linear optics, i.e. waveplates and beamsplitters [59]. Here, the entangled photons 2 and 3 are created using an electrically biased E-LED. Photons 1 and 2 are projected onto an entangled state by superposing them on a beamsplitter, where they will interfere if they are indistinguishable. The outputs of the beamsplitter are directed to polarisation-resolving detectors, which will make the two photons to collapse onto a Bell state when registering simultaneous coincidences. Note that for the implementation in chapter 4, coincidences at one of the beamsplitter arms signalling bunching of photons are used for the Bell state measurement (BSM). It is obvious from the arrangement that the indistinguishability between photons 1 and 2 is a crucial element for the success of the scheme. This will be explored further in Chapter 3, as the two-photon interference of two independent sources will be assessed.

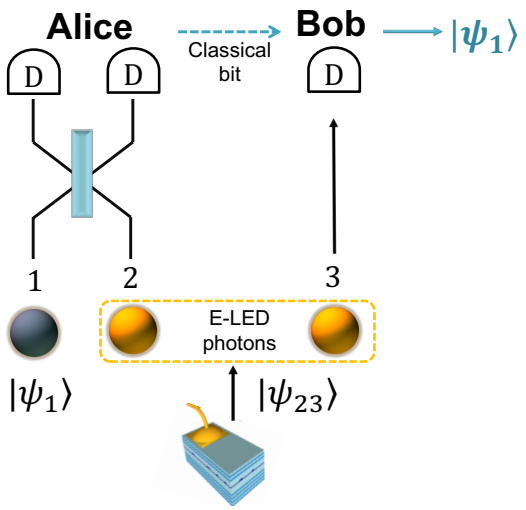

Figure 1.4: Quantum teleportation schematic. The input qubit is at port 1 of the beamsplitter and the entangled photon pair is at ports 2 and 3, which can be locally separated. Target photon is at 3. A Bell state measurement is performed by Alice on qubits 1 and 2. Using a classical bit to apply some logical transformation to his measurement, Bob can acquire the initial state.

1.7 Quantum Cryptography

Quantum teleportation would be required in any implementation of a future quantum network. The nodes in such a network generate and distribute entanglement to other nodes for the implementation of cryptographic protocols. Quantum Key Distribution (QKD), which is a standard form of quantum cryptography, is one of the applications that have emerged with the field of quantum information. QKD takes advantage of quantum mechanics to enable unconditionally secure distribution of private information.

In QKD, as proposed by Ekert [60], key generation and security verification are achieved by quantum entanglement and by completeness of quantum mechanics. Assume we have a network in which Alice wants to communicate with Bob and where an eavesdropper (Eve) is present. Alice and Bob ensure security of their communication by exchanging keys. If Eve attempts to extract information, then the state of the system will be altered, as dictated by laws of quantum physics. In this case Alice and Bob discard their keys. The original QKD BB84 protocol [17] requires single photon sources for the implementation of a QKD system however, other protocols exist that show security can be achieved even with non-ideal quantum light sources. The principle is that photon polarisation is used to encode binary information, so that Alice and Bob can exchange a key. Alice can choose two polarisation bases to send random strings of qubits in, for example rectilinear and diagonal. In rectilinear basis, a horizontally-

polarised photon ↔ would correspond to binary 0 and a vertically-polarised photon ↕ would correspond to 1. Similarly, in diagonal basis a 45-degree polarised photon ↗ and a -45-degree photon ↘ would correspond to binary 0 and 1 respectively. The diagonal basis states can also be expressed in terms of the rectilinear basis vectors as:

$$|D\rangle = \frac{1}{\sqrt{2}}(|H\rangle + |V\rangle) \qquad (1\text{-}8)$$

$$|A\rangle = \frac{1}{\sqrt{2}}(|V\rangle - |H\rangle) \qquad (1\text{-}9)$$

where $|D\rangle$ encodes a binary 0 and $|A\rangle$ encodes a binary 1. Bob makes a random basis selection for measuring each arriving photon. If the basis selection is aligned with Alice's for that particular qubit, Bob will see the correct 0 or 1. For the rest of the measurements (half the qubits) Bob destroys the encoded information. Following certain steps of the protocol, Alice and Bob can then exchange messages over a public channel and determine whether their communication has been undisturbed or not. An eavesdropper cannot avoid detection, as the errors introduced by her measurement will be revealed when Alice and Bob publicly compare a small part of the key.

Most of the QKD schemes that exist nowadays require single photon states as information carriers. In the absence of a true single-photon source, QKD implementations usually use weak light pulses, where each pulse has a non-zero probability of multi-photon emission, giving the possibility to an eavesdropper to 'steal' a photon and avoid detection. The photon number splitting (PNS) attack is based on this situation, where the security of QKD may be compromised and an eavesdropper may obtain the key. The recent development of decoy-state protocols [61], [62] has improved the security for attenuated laser based schemes; however, analysis shows that a true single-photon emitter still gives the advantage of extending the distance of secure QKD with higher efficiency [63], [64].

Since optical fibres are used to transmit the photons, optical losses are a main limiting factor in the achievable communication distance. Distribution of entanglement over longer distances is possible with the use quantum of repeaters and quantum relays [65], thereby dictating that future network implementations will involve multi-node communications. Subsequently, quantum teleportation and entanglement swapping with single-photon emitters are important building blocks for multi-partite network configurations.

Finally, it is fitting to note that generation of single photons at specific timing is important for practical QKD or quantum networking based on photonic qubits [31]. A compact, on-demand single photon source can enable the large-scale implementation of a quantum network.

1.8 Objectives of the project

The chapters in this thesis will demonstrate how the existing E-LED structure, grown with S-K quantum dots, can be used in standard quantum network applications. Based on a new device design, the capabilities of the structure as a pulsed single-photon emitter will be explored in chapter 3. A two-photon interference setup demonstrates how photons from the E-LED can interfere with laser photons in pulsed mode, which is an underlying requirement for logical operations in quantum communications. In chapter 4, a proof of principle quantum relay setup enables teleportation of weak laser states over a kilometre of fibre, demonstrating the potential of the device in a quantum network of more than 2 nodes.

The two last chapters seek to improve the performance of the existing device. Two types of approach can be followed: a different growth strategy, which changes the fundamental character of the quantum dots, or a different triggering method, which changes the excitation conditions around the quantum dots. An alternative method (i.e. droplet epitaxy) of quantum dot growth will be explored in Chapter 5. The simplicity of the E-LED device design allows for easy adoption and a new type of an improved entangled-photon emitter is developed. Chapter 6 will be dedicated to experimenting with a different approach to generating photons. The electrical injection capabilities of the device are pushed aside, so that resonant two-photon excitation can be used to optically excite the quantum dots. This strategy also allows for direct comparison with other published work, since this is quite a standard approach in similar research groups.

Chapter 2 Methods

2.1 Introduction

This chapter will present the experimental methods and processes used during this project. The Entangled-Light Emitting Diode (E-LED) used for the experiments will be presented, as well as the fabrication methods employed to process the samples into devices. Finally, the basic experimental setups for device characterisation and optical measurements will be explained.

2.1 Entangled-LED operation

The E-LED is essentially a p-i-n heterostructure, as shown in Figure 2.1. InAs QDs are placed in a 2λ-cavity within the intrinsic region of the semiconductor structure, which is approximately 400nm thick. The thickness of this layer is crucial, as a short intrinsic region would allow electron tunnelling from the n-doped region into the dots during the biexciton cascade decay. The consequence of this effect is charging of the neutral X state and loss of polarisation entanglement. In order to optimise photon collection, the structure has sixteen GaAs/AlGaAs distributed-Bragg-reflector (DBR) repeats below the InAs/GaAs quantum dot layer and five above it.

As explained in the previous chapter, a requirement for entangled photon pairs is for the quantum dots to exhibit a small fine-structure splitting. It has been previously observed that the FSS of quantum dots grown by MBE is wavelength-dependent and minimises around 885 nm [66]. For this reason, the quantum dot layer is engineered accordingly during growth. The devices made for this project were designed to be operated under pulsed conditions and made to be smaller than in previous reports. The assumption here was that a smaller device capacitance would allow faster switching between the on and off state of the diode. A single diode is just 220x110 μm in size and has a density of the order of 1 QD μm^{-1}.

The emission of polarization-entangled photon pairs is achieved through the biexciton cascade. Under cryogenic conditions and electrical injection of carriers, a single quantum dot may capture two electrons

and two holes. This biexciton state then decays to the ground through two different polarization paths. In the case of the fine structure splitting of the dot being zero, the two decay paths give two photons that are polarization-entangled according to:

$$\Psi = \frac{1}{\sqrt{2}}(|RL\rangle + |LR\rangle) \qquad (2\text{-}1)$$

The two-photon Bell state describes the exciton and biexciton states being circularly polarized, with R and L corresponding to right and left-circular polarisations. The current E-LED design and the potential to act as an on-demand source of entangled photon pairs was the motivation to investigate the mechanisms of pulsed mode operation.

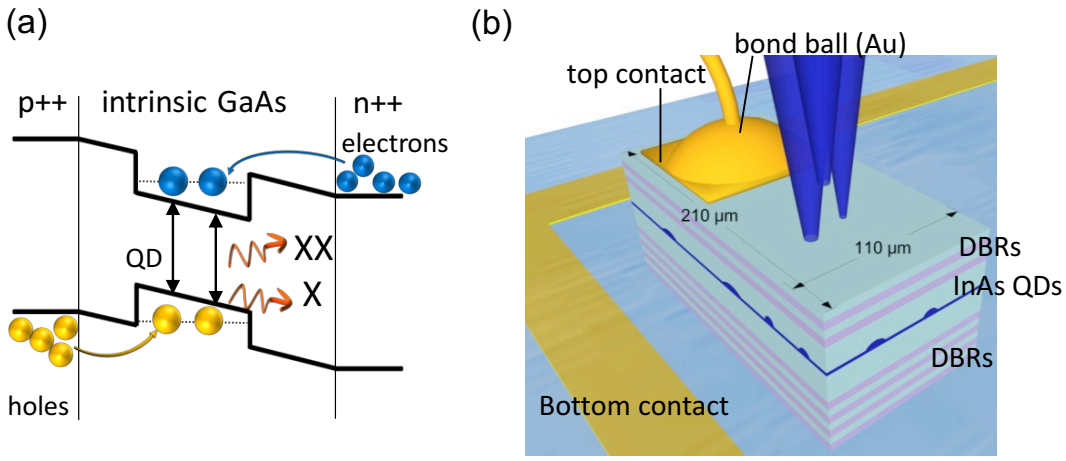

Figure 2.1: E-LED schematic diagram [52]. Positively-biased p-i-n diode causes QDs to be populated and results in entangled photon pair emission (X, XX). The diode consists of the two doped p- and n-regions, and an intrinsic region, where the QDs are embedded in. A built-in electric field exists across the intrinsic region when no bias is applied. The potential barrier is lowered with a positive applied bias across the diode. Current flow and carrier injection occur under flat-band regime, which occurs around 1.5V at low temperature (5K). (b) Side view of a single diode mesa. InAs QDs sit inside a cavity with top and bottom DBR mirrors. A top contact (p-layer) and a bottom contact (n-layer) need to be deposited in order to make electrical connections (refer to Figure 2.2 for real-life devices).

2.2 Fabrication of devices

The fabrication of fully operating devices for use in an optics laboratory was implemented using standard cleanroom processes. The growth of the semiconductor structures was done by Cavendish Laboratory. The initial p-i-n structure is a bare wafer, which then needs to be processed, in order to produce

several packaged devices. Some of the basic processes are wet-etching, photolithography, metal contact deposition by evaporation and finally bonding.

The first step is to create individual diodes by defining mesas on the structure, so that a top and a bottom electrical contact can be added. This is achieved by etching the initial piece of wafer using a sulphuric acid solution. The rate of etching must be calibrated in order to reach the correct etch depth for the bottom contact. Creating patterns on a sample is achieved with photolithography, where a mask with particular metal film patterns is exposed onto the sample. The sample is first covered in photoresist and after careful alignment with a mask the desired pattern is exposed using high-intensity UV light. Consequent evaporations or etching steps will only apply to the patterned areas that are not covered in photoresist. The current E-LED design requires a top and a bottom electrical contact to be made, corresponding to the p- and n- doped regions, as shown in Figure 2.2 (b). The standard procedure for the fabrication of such a device will require at least 3 photolithography steps: one for defining mesas and one for each contact deposition. A square strip running around all the mesas forms the bottom contact, common for all the diodes. The top contact is a square covering almost half the area of the mesa, enough to accommodate a metal bond. The design allows many individual devices to be accessed separately, while their small area size allows for more uniform current distribution. The bottom contact sits on the n-doped layers and therefore an ohmic contact is formed using a gold/germanium/nickel (AuGeNi) alloy as the metal. Firstly, the metal is evaporated under vacuum conditions on the sample. A lift-off step follows, which removes the metal layer sitting on photoresist, only allowing the bottom contact pattern to be covered in metal. Finally, the metal is annealed at 430 °C, to make the alloy diffuse into the semiconductor layers. The top contact sits on the p-doped layer and thus a layer of gold/titanium (Au/Ti) is a more suitable combination to form a junction. This metal is not annealed after evaporation, so that atoms do not diffuse down to the dot layer.

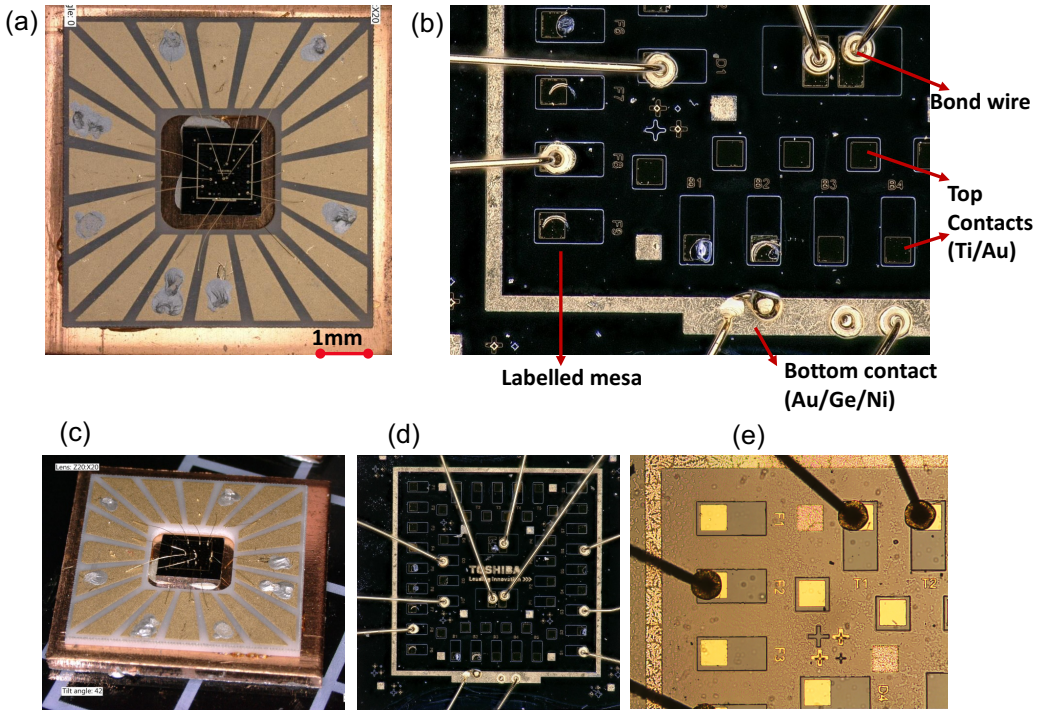

Figure 2.2: (a) Microscope image of a packaged device. The device sits on a copper block and bond wires connect the individual mesas to the bond pads. The cryostat copper wires are attached to the bond pads with silver paint. (b) Magnified microscope image of the chip. The individual mesas are labelled and some of them are bonded to the pads. There is one common bottom contact for all the mesas in the form of a surrounding square. (c) Side view of (a). (d) Full image of (b). (e) Bright field image of the device.

2.3 Cryostat setup

A schematic of the experimental setup used for sample characterisation in the lab is shown in Figure 2.4. Quantum dot emission was extensively characterised using various spectroscopy methods. Because of the material of the devices, carrier confinement and single-photon emission is possible only at low temperatures, of the order of 5 K. Most of the experiments in this thesis were carried out at around 19 K, at which temperature the electrical injection and photon collection was improved, unless stated otherwise. To reach such low temperatures, a cryostat system is required to cool the sample using liquid Helium. A continuous-flow cryostat is used primarily for characterisation of the samples, as shown by Figure 2.4. The sample is mounted on a cold finger using silver paint to provide good thermal contact and may be electrically connected to external power supply equipment. A downside of this arrangement is that the copper wires inside the cryostat may provide a heat conduction path from the outside. The setup includes various mechanical stages and piezo controllers for movement on the sample in the X,

Y and Z planes. For experiments requiring longer cooling cycles, a second cryostat system is used, illustrated by Figure 2.3. The second system consists of a helium dewar insert, on which optics can be easily mounted, providing increased sample stability and isolation from pump vibrations. The insert is attached to the top of the Helium dewar and the sample cools down by Helium vapour. An electronic heater provides control over the sample temperature. The sample sits on piezo stage mounts, which give movement control in all three directions with very high precision (nm). Light is collected from the top, in a similar fashion to the continuous-flow system (see below). A more detailed analysis of the set of optics is given in Chapter 4, as it was adjusted specifically for the Quantum Relay experiment.

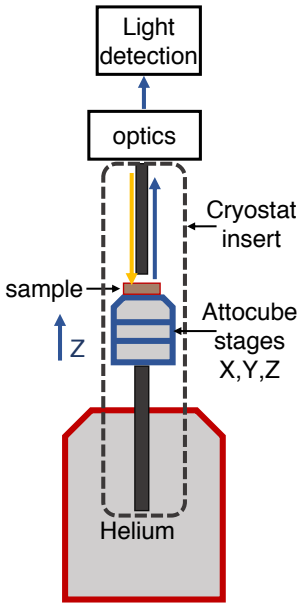

Figure 2.3: "DStat" cryostat system. This cryostat setup was used for experiments due to its very low vibrational levels.

2.3.1 Quantum dot spectroscopy & imaging system

The imaging system in the laboratory is mostly fibre-based and is very convenient in the sense that individual dots can be directly located and thus, spectrally isolated. A magnifying microscope objective lens is used to image a single mesa (220x110 μm) at a time. Luminescence from the sample exits the cryostat window, goes through a lens objective and is collected by an 11 mm collimated fibre. A small fraction of the light (2%) is directed to the camera for imaging. A broadband LED source (940 nm or 790 nm) can be used to image the device, as the reflected light will go through the same path. If emission from the device is present, an optical filter centred at the dot wavelength (885 nm or 900 nm) can be used to isolate specific wavelength emission and therefore allow us to image emission from

single dots, as in Figure 2.4 (b). The camera images can be used to map the individual dots from each device for easy identification. The rest of the emission will be guided through various optical components to the spectrometer for spectral analysis.

The collection spot has a small area of ~1.14 μm² on the sample and is then coupled into a single-mode (SM) or polarisation-maintaining (PM) fibre with a 5 μm core. Emission spectra are acquired by a spectrometer, which has a coarse grating (600 lines/nm) and a fine grating (1800 lines/nm). A charged coupled device (CCD), cooled with liquid nitrogen, is used as a sensor array to detect the light from the gratings. Depending on the nature of the measurement, other optics such as half-wave plates or polarisers can be easily included in this setup.

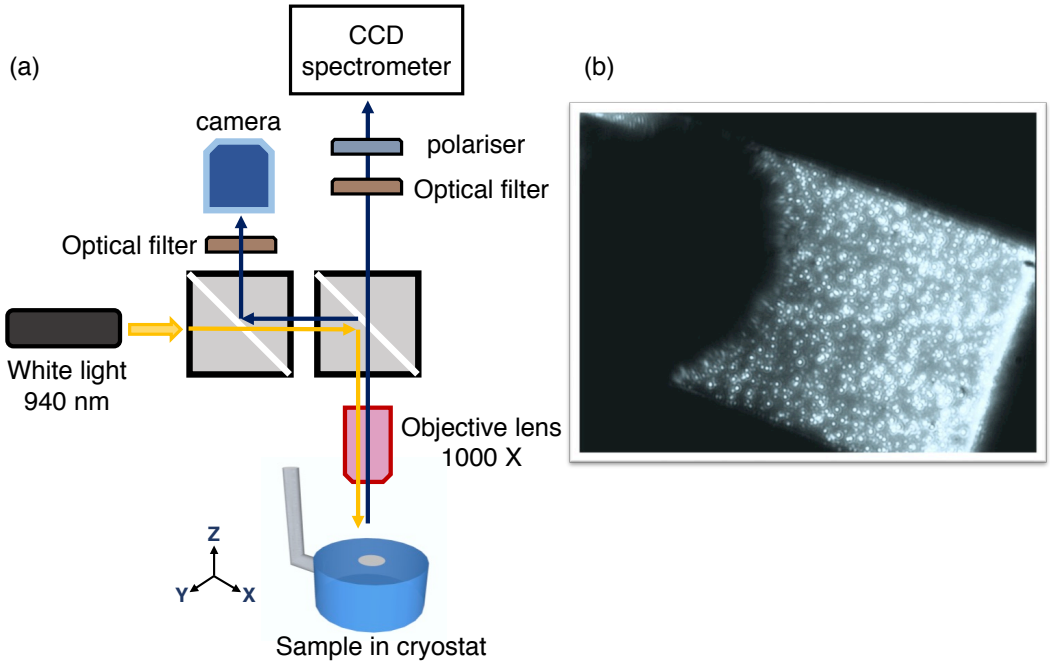

Figure 2.4: (a) Cryostat and optics setup with imaging system in the laboratory. (b) Camera image of single diode mesa. Here, only emission from around 885 nm goes through to the camera sensor and that is how single bright spots corresponding to dots can be observed. The rest of the emission from the sample i.e. from the wetting layer is suppressed.

2.3.2 Electroluminescence

The E-LED device used for the experiments is designed to operate under electrical injection conditions. Carriers are injected into the QDs through non-resonant electrical excitation when the diode is biased beyond its turn-on voltage. The turn-on voltage corresponds to the built-in electric field

(~1.5 V) across the intrinsic region. At forward bias, the energy bands of p- and n- doped regions are aligned and carriers relax into the lower energy levels of the quantum dots.

Figure 2.5 shows the voltage bias dependence of emission intensities for exciton and biexciton photons. In general, the exciton emission should show a linear dependence on power, before saturation. The biexciton emission should show a super-linear dependence, as two electron-hole pairs are required for this state. Beyond saturation, the exciton intensity will decrease as the X decay rate will be slower than the electron-hole pair capture rate. For this particular dot, the exciton sits at a higher energy level than the biexciton, indicating that the binding energy is positive. Photon emission characteristics and properties greatly depend on current injection conditions, as will be shown in the next chapters.

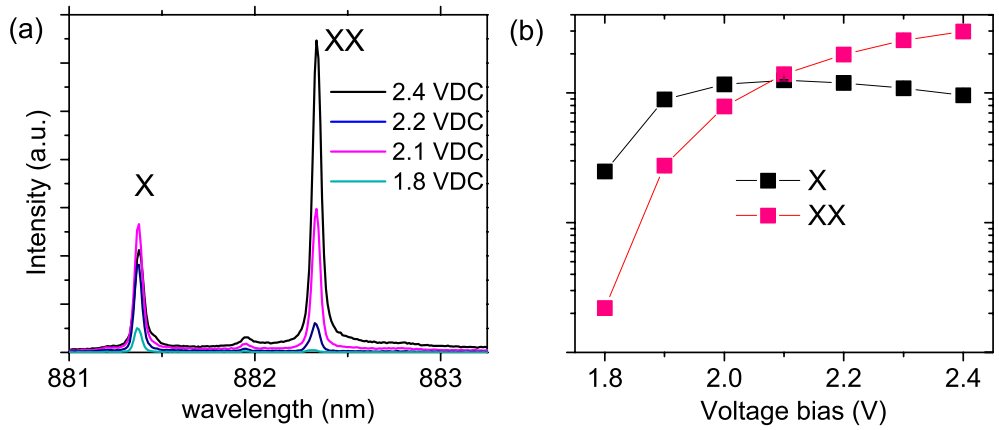

Figure 2.5: (a) Spectrum of a quantum dot with positive binding energy over a range of bias voltage. (b) Voltage bias dependence of the intensity for the biexciton and exciton emission lines.

2.4 Coherence time measurements

The experiment in chapter 3 will show how two single photons can interfere on a beamsplitter, which is a required operation in a teleportation protocol. In order for the two photons to interfere maximally, they have to be maximally indistinguishable [67]. One of the main limitations in measuring indistinguishable photons is their coherence time. Due to dephasing processes that take place at the atomic level, the time during which measurements can take place is compromised. Taking both the radiative decay time τ_r and the pure dephasing time τ_d into account, the effective coherence time τ_c is defined as [32]:

$$\frac{1}{\tau_c} = \frac{1}{2\tau_r} + \frac{1}{\tau_d} \qquad (2\text{-}2)$$

Ideally, we would like the radiative process to be homogeneously broadened only by spontaneous emission and $T_2 \gg \tau_r$, so that the photons are Fourier-transform limited. In reality, this is not the case, as the QD carriers are affected by Coulombic interactions with carriers from the wetting layer, nearby defects or other quantum dot charges, which induce a small spectral Stark shift. As a result, the dephasing time becomes much shorter than the radiative lifetime. The reason is the time-varying Stark shift of the emission energy. Linewidth broadening or spectral diffusion is also a result of incoherent excitation i.e. p-shell or wetting layer excitation and consequent relaxation through phonon emission [5],[6].

A simple way to assess the coherence times of the X-XX pair is to perform first-order coherence function measurements. A Michelson interferometer is used for this purpose, in a setup shown in Figure 2.6.

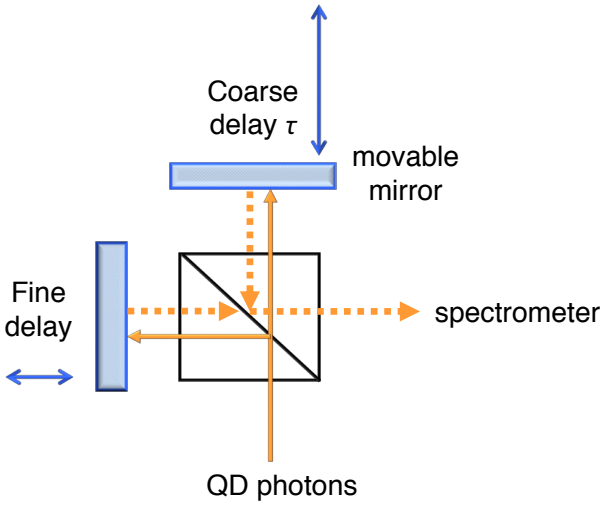

Figure 2.6: A Michelson interferometer setup for measuring the first-order coherence function of a single photon source. The light from the QD passes through a beamsplitter and is directed to two different arms. The recombined beams produce an interference pattern that can be detected by the spectrometer (Figure 2.7 (a)).

The incoming QD light is considered as a light field of the form $\sqrt{I_0}e^{i\omega_0 t}$, where ω_0 is the central frequency of the emission. The wave packet is split into two paths by a 50:50 beamsplitter. At the end of the two arms there is a fine delay stage and a coarse delay stage. The coarse delay stage is a motorised stage that has been calibrated to add up to 800 ps of delay to the light path, whereas fine delay stage is a piezo stage allowing for small delay steps (0.1 μm) along the second path. The reflected light from both arms interferes at the beamsplitter and exits the interferometer. We can then consider the interference of two waves of equal intensities propagating from the two different arms with a phase difference [70]. The detected intensity *I* is given by

$$I = \langle |E(t)|^2 \rangle + \langle |E(t+\tau)|^2 \rangle + 2Re\langle E^*(t+\tau)E_1(t+\tau) \rangle$$

$$= \langle |E(t)|^2 \rangle + \langle |E(t+\tau)|^2 \rangle + 2\langle E^*(t+\tau)E_1(t+\tau) \rangle \cos(\omega\tau) \quad (2\text{-}3)$$

The electric field is related to the measured intensity as $|E(t)|^2 = I(t)$ and the first-order coherence function $g^1(\tau) = \langle E^*(t+\tau)E_1(t+\tau) \rangle$ is related to the last term, so that the detected intensity is analogous to:

$$I_{out} \propto 2I[1 + g^1(\tau)\cos(\omega\tau)] \quad (2\text{-}4)$$

Varying the time delay τ of the paths produces interference fringes of period ω_0, which can be observed by recording spectra as in Figure 2.7 (a). The decay of the contrast between the maxima and minima as a function of path delay τ can be used to determine the coherence time τ_c. The interferogram produced from the spectra can be studied in order to determine the single-photon interference visibility as a function of coarse delay time, defined by:

$$V(\tau) = \frac{I_{max} - I_{min}}{I_{max} + I_{min}} \sim g^1(\tau) = e^{-\frac{|\tau|}{\tau_c}} \quad (2\text{-}5)$$

where I_{max} and I_{min}represent the maximum and minimum intensities of the interference pattern observed. The shape usually resembles an exponential decay, but can also have a Gaussian profile or a combination of the two (Voigt). We usually approximate the interference visibility decrease with an exponential or Gaussian function and determine τ_c from the fitting of the curve. For an exponential, the τ_c corresponds to where the visibility falls to 1/e of the initial value. Figure 2.7 (b) shows interferograms used to measure the coherence times of an exciton and a biexciton photon, fitted with Gaussian profiles. The method is equivalent to Fourier transform spectroscopy, as the energy spectra are transposed to time domain interferograms.

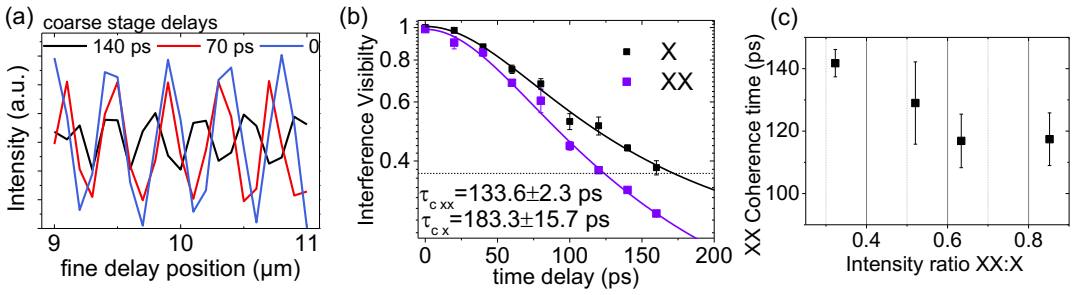

Figure 2.7: (a) Typical interference fringes for different relative delays between the two optical paths. At τ=0 the visibility is maximum (1) as the two beams interfere perfectly. For a stage delay corresponding to 140ps of path difference the interference is degraded and the difference between maximum and minimum intensities is reduced. (b) Coherence time measurement for an X-XX pair extracted from Gaussian fittings to the visibility function over time delay. The dotted line shows the function $V = 1/e$. (c) Biexciton coherence times as a function of the XX:X intensity ratio.

As explained above, the coherence time is strongly dependent on the dot environment and the electric field fluctuations around it that cause spectral diffusion. This is not only related to the sample structure but also to the way of excitation and hence the way charge carriers are created around the dots [71]–[73]. Figure 2.7 (c) illustrates the effect of increased current injection on the measured coherence time of the biexciton photon for an S-K QD. With increasing excitation power τ_c degrades, manifesting as a broadened linewidth. In general, the effective coherence length of the excitons depends on a combination of excitation conditions, sample temperature and substrate quality. As a result, optimum emission conditions need to be investigated and tuned.

2.4.1 Fine-structure splitting measurements

As explained in Chapter 1, for ideal quantum dots, the entanglement of the biexciton cascade photons is described by the entangled state in (2-1). For real, asymmetric quantum dots, however, we need to consider the phase evolution of the system during the decay, which results in the presence of fine-structure splitting. Polarisation-resolved spectroscopy can reveal such information simply by adding a half-wave plate and a linear polariser to the setup, as shown in Figure 2.8. Horizontally or vertically polarized light from the dots can be measured by mechanically rotating the half-wave plate, allowing the detection of any energetic splitting between the two decay paths. The light is guided in a PM fibre and the polarisation is "selected" with a linear polariser aligned to one of the polarisation modes before the spectrometer slit entrance. For example, if the measurement when the HWP is at an angle φ to the polariser reveals the horizontal component of the emission, then the measurement at angle φ+45° will reveal the vertical component of emission.

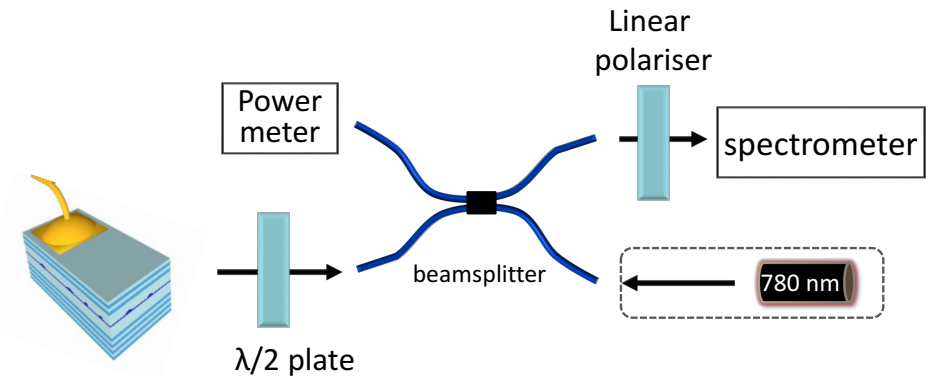

Figure 2.8: Setup for polarisation-resolved spectroscopy and fine-structure splitting measurements. A motorised half-wave plate is inserted before the QD emission is coupled into fibre. A rotation of the waveplate by 90° is enough to allow the vertical and horizontal components of the emission to be resolved. PM fibre is used with a linear polariser to select one mode only. Optionally, a laser can be used to optically excite samples without electrical contacts, as described in 2.4.2.

Rotating the HWP over different angle steps can allow the different polarisation components to be spectrally detected at a time. The energy difference between the horizontal and vertical components of dot emission will manifest as different spectral wavelengths for each case, but usually this energy splitting is smaller than the spectral resolution (~30 μeV) and cannot be spectrally resolved. Instead, the wavelength of emission can be extracted by fitting Lorentzians to the exciton and biexciton emission lines. The binding energy of the exciton-biexciton pair is then probed and plotted over several HWP angle steps, as shown in Figure 2.9. The difference in energy between the exciton and biexciton emission (binding energy) will vary sinusoidally and will be maximum when the light is detected at one of the two linear eigenstates (H or V). The fine-structure splitting can thus be extracted from the sinusoidal fit, as shown in (a).

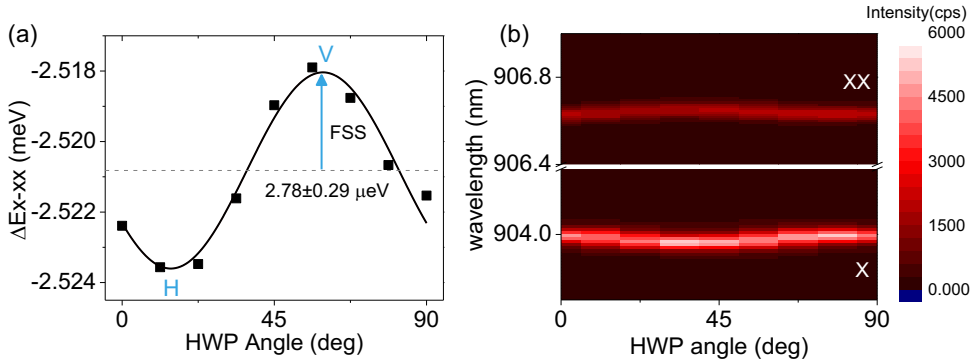

Figure 2.9: Typical FSS measurement using a half-wave plate. (a) The difference in spectral energy varies with the HWP rotation, shifting from the H to V linear polarisations of the dot axes. (b) For FSS comparable to the spectrometer resolution, the energy shift is easily observed from X and XX emission lines.

2.4.2 Micro photoluminescence (micro-PL)

Although the E-LED is used primarily under electrical conditions, PL measurements are sometimes needed. PL spectroscopy is useful for characterising calibration or test samples that have no electrical contacts, in order to identify spectral characteristics of emission such as dot density, emission wavelength or injection properties. The setup arrangement is adjusted at the beamsplitter to include a laser input as shown in Figure 2.8. Spectra can be obtained by above band excitation with a CW laser or a pulsed laser emitting at 780nm. Laser light goes through a 95:5 beamsplitter and excites a small area on the sample through the 5% port. The collected light goes through the same port and couples to the efficient 95% port before reaching the spectrograph. An optical filter centred at the quantum dot wavelengths can be used to filter out laser spectra.

2.5 Time-Resolved Spectroscopy

In order to study the emission properties in the time-domain, photon correlations can be recorded. Single-photon detectors with the photon counting software and electronics are used to detect photon coincidences. For these measurements, either silicon Avalanche Photodiodes (APDs) with a resolution of ~400ps or superconducting single photon detectors (SSPDs) with a resolution of ~60ps can be used. Using higher resolution detectors has great advantages for measuring photon coincidences; however, the SSPDs have a low efficiency of the order of 31% and require liquid helium for operation, whereas APDs operate at room temperatures.

2.5.1 Second-order autocorrelation function

To characterise the single-photon character of the emission from a single QD, we can measure the normalized second-order correlation (autocorrelation)

$$g^{(2)}(\tau) = \frac{\langle I(t)I(t+\tau)\rangle}{\langle I(t)\rangle^2} \qquad (2\text{-}6)$$

The function measures the light intensity $\langle I(t)\rangle$ at two different time points, using a Hanbury-Brown-Twiss setup, as shown in Figure 2.10 [74], [75]. The light from the quantum dot is spectrally filtered using a transmission grating and the exciton and biexciton photons are collected separately. Photons from either emission state are divided at a 50:50 beamsplitter and the two output paths are subsequently fed to two different detectors. These outputs are then used to control the start and stop signals on the correlation module. Only the time differences between the detection events are registered in order to generate a histogram of coincidence events; the hardware has a TAC (Time to Amplitude Converter) and negative correlations can be observed by adding some delay to the STOP (sync) signal.

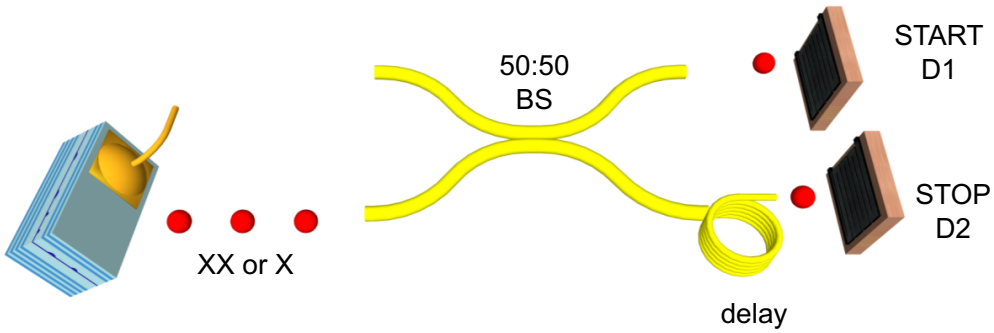

Figure 2.10: Hanbury-Brown-Twiss (HBT) setup for $g^{(2)}$ measurement. A beamsplitter divides the incident optical field with and the outputs are sent to detectors D1 and D2. Coincidences are registered when both detectors click and the correlation describes the time-dependent probability of two photons being emitted from the source.

The photons arrived at the detectors separate from each other, exhibiting the phenomenon of anti-bunching. Experimentally, anti-bunching can be observed by measuring the autocorrelation function, as shown in Figure 2.11 (a), where a dip can be observed around $\tau = 0$. For an ideal single photon emitter, the probability of multi-photon emission is zero and $g^{(2)}(\tau = 0) = 0$, as the two detectors cannot both click at τ=0. In reality, the $g^{(2)}$measurement is limited by the timing resolution of the detectors. Away from $\tau = 0$ the $g^{(2)}$ rises to 1.

Figure 2.11 (b) and (c) show autocorrelation measurements for biexciton photons under pulsed excitation. In (b) the photons come from an E-LED under AC bias at a frequency of 203 MHz and a pulse width of 490 ps. The photons in the pulsed excitation case are emitted in different cycles and are separated from each other in time. A dip in the central pulse peak is observed, indicating suppressed multi-photon probability. The non-zero probability of detecting a biexciton photon around $\tau = 0$ indicates repopulation of the QD by carriers before an exciton can be emitted. This behaviour is usually observed at high bias driving conditions, when a lot of charge carriers are created around the dot. Figure 2.11 (c) was obtained from a Droplet-Epitaxy QD sample under optical excitation. In contrast to (b), the central peak is almost absent, as the excitation pulse is very short (fs).

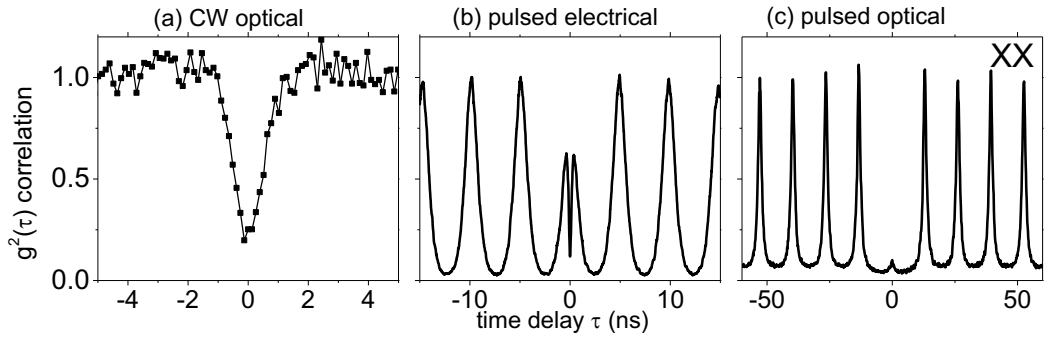

Figure 2.11: Autocorrelation function measured for biexciton photons under different excitation conditions. (a) DC excitation. Clear anti-bunching is observed at $\tau = 0$. (b) AC bias electrical injection. (c) Narrow pulse optical excitation. There is almost complete absence of counts around the $\tau = 0$ peak.

2.5.2 Characterising Entanglement

Entangled-pair emission from a quantum dot can be characterised by polarised second-order correlation measurements. The setup is illustrated in Figure 2.12, where the polarisation bases are calibrated using linear optics components. In an ideal case, the exciton-biexciton pair would be projected into the Bell state $|\Psi^+\rangle$ which can be expressed in any polarisation basis on the Poincare sphere. For the purposes of this thesis, the three orthogonal bases used are: the rectilinear, diagonal and circular, with their respective state vectors, so that

$$|\Psi^+\rangle = \frac{1}{\sqrt{2}}(|H_{XX}H_X\rangle + |V_{XX}V_X\rangle) = \frac{1}{\sqrt{2}}(|D_{XX}D_X\rangle + |A_{XX}A_X\rangle)$$
$$= \frac{1}{\sqrt{2}}(|R_{XX}L_X\rangle + |L_{XX}R_X\rangle) \qquad (2\text{-}7)$$

The fidelity f of the photon pair to this state is used as a criterion for entanglement. In the case of unpolarised light, the fidelity can be calculated by averaging the degree of correlation over the Bloch sphere in three orthonormal bases: the rectilinear (states H/V), the diagonal (states D/A) and the circular (states R/L) [38], [76], [77]:

$$f = (1 + C_{HV} + C_{DA} - C_{RL})/4 \quad (2\text{-}8)$$

where $C_{a\bar{a}}$ denotes the degree of correlation in the different polarisation bases.

$$degree\ of\ correlation\ C_{a\bar{a}} = \frac{g_{aa}^2 - g_{a\bar{a}}^2}{g_{aa}^2 + g_{a\bar{a}}^2} \quad (2\text{-}9)$$

From (2-8), it is obvious that the X-XX photon pair would be co-polarised in the rectilinear and diagonal bases, whereas in circular they would be cross-polarised. We assume that emission from our QDs is unpolarised, and the decay path of the biexciton cascade is random. The fidelity can vary from 0.25 for uncorrelated sources to 1 for perfectly entangled photons. The presence of a large fine structure splitting lowers the value of f, as in (1-3) and reduces the wavefunction to a classically-correlated state. In this case, the fidelity has an upper threshold of 0.5. Therefore, a measurement of f>0.5 indicates entanglement between the photon pair. Calculation of entanglement fidelity will be shown in Chapter 4 for an S-K QD and in Chapter 5 for a D-E QD.

The fidelity of the photon pair emitted by the quantum dot to the maximally entangled state Ψ^+ can be determined by measuring second-order correlations in the three polarisation bases. The angle of the rectilinear basis (HV) of the dot emission is identified using a linear polariser. The diagonal basis DA is found at 45° degrees to the HV angle or by adding a half-wave plate at 22.5° to the HV in front of the linear polariser. Similarly, the circular basis RL can be calibrated using a quarter-wave plate at 45° to the HV, in front of the linear polariser. The elliptical basis is found in-between DA and RL on the Bloch sphere, equivalent to 22.5° (λ/4-plate) to the HV.

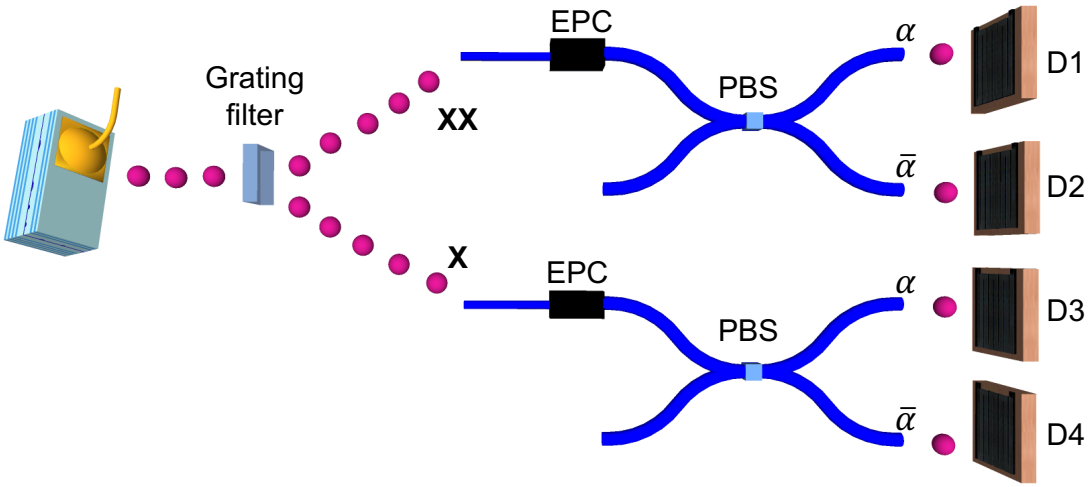

Figure 2.12: Polarisation correlation measurement setup for characterising entanglement. Individual bases are calibrated with a linear polariser and wave plates with Electrical Polarisation Controllers (EPC). The light from the QD is filtered using a grating and the X-XX lines are collected separately. A pair of detectors detects orthogonal modes $a, \bar{a}$ for each photon. PBS: polarising beamsplitter.

Chapter 3 Pulsed two-photon interference

3.1 Introduction

Indistinguishable photons present a fundamental requirement for scalable quantum computing operations [31] and communications protocols based on quantum interference phenomena. More specifically, two-photon interference is a requirement for Bell state projections and hence for the implementation of the quantum teleportation protocol [78] illustrated by Figure 1.4 and further explored in Chapter 4. Observation of interference, where two photons are incident on a beamsplitter, has been used to assess the indistinguishability of single photons in the past [9], [79], [80].

Semiconductor QDs are a promising example of sources that can generate single, indistinguishable photons for quantum information applications. Two-photon interference (TPI) from separate QDs has been shown previously [81], where electrically tuneable devices were excited optically. TPI from optically excited QDs [82] and quasi-resonantly excited QDs [83] have also been reported. Interference of two independently generated single photons has also been studied, as future quantum networks would employ distributed sources: indistinguishability between a QD photon and an SPDC photon [84] and interference between a laser and a QD photon [85] [86]. Given that communications schemes and QKD applications generally employ weak coherent pulses as sources, arrangements where a laser can be used as an input source made to interact with entangled photons are of practical interest. For this thesis, two-photon interference between a laser photon and an E-LED photon from a quantum dot under pulsed injection mode is demonstrated, as a requirement for the quantum relay experiment in Chapter 4.

3.2 Photons on a beamsplitter

A crucial component for the observation of quantum interference is the beamsplitter. A photon incident on a beamsplitter may either be reflected or transmitted. Figure 3.1 shows the possible outcomes

when two photons are incident on a beamsplitter with two input ports and two output ports beamsplitter: (a) both photons are transmitted, (b) both photons are reflected, (c) photon at 1 reflected and photon at 2 transmitted and (d) photon at 1 transmitted and photon at 2 reflected. Classically, finding one photon in each output port has 50% probability of occurring. In quantum mechanics terms, this is not the case. Assuming a lossless beamsplitter, the reflection and transmission probability amplitudes are $\pi/2$ out of phase. This probability becomes 0 in quantum terms, as the probability amplitudes for cases (a) and (b) have a phase difference of -1 (i^2) and cancel out [67]. Following from the two-photon interference analysis by [87], the effect can be modelled as wave packets in the following way: The two single photons enter the beamsplitter ports 1 and 2 and the initial state can be described as

$$|\Psi_i\rangle = |1_1 1_2\rangle = a_1^\dagger a_2^\dagger |0\rangle, \quad (3\text{-}1)$$

where $a_{i=1,2}^\dagger$ are the photon-creation operators on the vacuum state $|0\rangle$. The effect of the 50:50 beamsplitter can be described by the unitary transformation

$$\begin{pmatrix} a_1^\dagger \\ a_2^\dagger \end{pmatrix} = \frac{1}{\sqrt{2}} \begin{pmatrix} 1 & 1 \\ 1 & -1 \end{pmatrix} \begin{pmatrix} a_3^\dagger \\ a_4^\dagger \end{pmatrix}, \quad (3\text{-}2)$$

where $a_{i=3,4}^\dagger$ are the photon-annihilation operators on $|\Psi_i\rangle$. The initial state in (3-1) can be expressed as

$$\begin{aligned} |1_1 1_2\rangle &= \frac{1}{2}(a_3^\dagger + a_4^\dagger)(a_3^\dagger - a_4^\dagger)|0\rangle = \frac{1}{2}\left(\left[a_3^\dagger\right]^2 - \left[a_4^\dagger\right]^2\right)|0\rangle \\ &= (|2_3 0_4\rangle - |0_3 2_4\rangle)/\sqrt{2} \quad (3\text{-}3) \end{aligned}$$

The result in (3-3) shows that the two photons will either exit port 3 or 4 together. The final superposition also shows how the beamsplitter can be used for entangling operations.

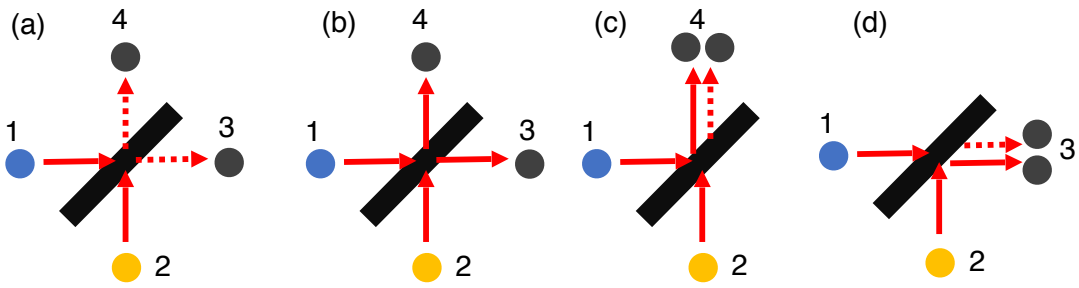

Figure 3.1: The four possible outcomes at the outputs when two photons are incident on a beamsplitter: (a) both transmitted, (b) both reflected, (c) and (d) one reflected and one transmitted. In cases (a) and (b) the two photons exit from different output ports. In cases (c) and (d) the two photons exit together. Solid (dashed) lines indicate reflected (transmitted) beams.

3.3 Theoretical background

As a requirement for quantum teleportation schemes, it is important to explore the effect that certain variables have on TPI, so that it can be optimised throughout the quantum relay experiment in Chapter 4. Here, a laser photon and a photon from a quantum dot under pulsed injection mode will be made to interfere. Contrary to the simple expressions given above, these photons are not pure states nor perfectly indistinguishable. A better understanding of the effect of various parameters can be obtained by modelling the two-photon interference between laser and QD photons. In this analysis, the QD photon is approximated as an exponential-decay wave packet, while the laser is assumed to have a Gaussian shape in the time domain. Other similar experiments have taken other approaches in the analysis of the electric field [81]. In reality, the quantum dot photons have a Voigt curve shape with both Gaussian and exponentially decaying components, as shown from the time-resolved measurements in Figure 2.7 (b), but the approximation will suffice for the purposes of this model.

A laser photon and a QD photon are incident on a beamsplitter as in Figure 3.2. A high degree of interference can be achieved if the wave packets overlap in space, frequency, time and polarisation [67]. Ideally, the photon sources need to be Fourier transform-limited so that the spectral linewidth $\Gamma = \hbar/\tau_r$ is defined by the radiative lifetime only [88], in which case maximum interference visibility is obtained from the overlapping wave packets. In reality, decoherence processes dictate the effective coherence length of the QD emission, as in (2-2), and the TPI visibility is directly related to τ_c, as will be shown later. For this reason, a biexciton photon will be used for the TPI beamsplitter operation, since it has a longer coherence length than its entangled pair. The incoming photon wave packets are in the form of a train of pulses (see time-resolved correlations in Figure 3.7 and Figure 3.8 (b)). The

analysis for the interfering wave packets however, will be limited to a single cycle in time. In mathematical terms, both the exponential decay and the Gaussian have a finite width and amplitude, determined by the source's physical properties. These parameters are derived from the excitation and recombination processes that occur in the diode. The biexciton photons are defined by (3-5) as an exponential decay function with a decay constant defined by the effective coherence time τ_c of the biexciton photon. Similarly, a Gaussian function of width σ is defined in (3-6) to represent the laser photons.

Another variable to take into consideration is the difference in time between the two emission events, denoted by $\delta\tau$ in Figure 3.2. This produces an uncertainty in the time when the two photons arrive at the beamsplitter and consequently affects the overlap and interference of the wave packets. The time difference between the two photon detections at detectors D1 and D2 is denoted by τ and should also be considered.

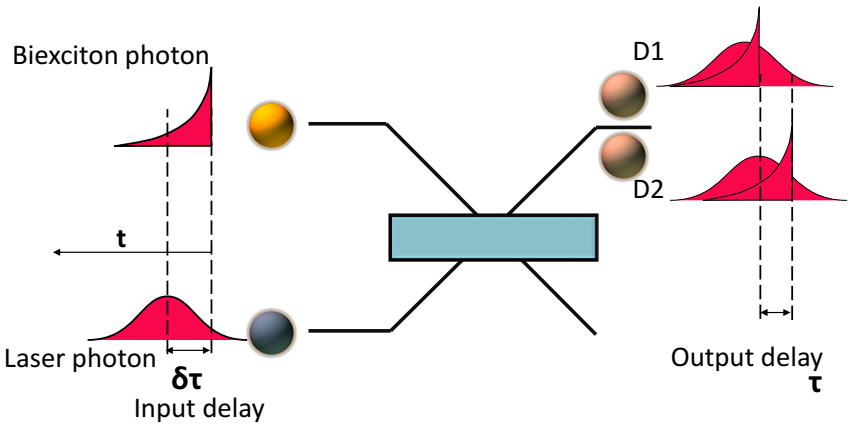

Figure 3.2: Laser photons: modelled as Gaussian wave packets, Q.D. Photons: modelled as exponentially-decaying wave packets. D1 & D2 are detectors at one of the beamsplitter outputs.

Following analysis from [81], [87], [89], the single photons arriving at the beamsplitter may be described by spatio-temporal modes of the form:

$$\zeta_i(t) = \varepsilon_i(t)\varphi(t) \quad (3\text{-}4)$$

where $\varepsilon_i(t)$ describes the amplitude envelope of the wave packet and $\varphi(t)$ represents the random phase fluctuations.

$$\zeta_1(t) = \frac{e^{\frac{-t}{2\tau_r} - i\omega_1 t - i\varphi(t)}}{2\tau_r}, \quad t \geq 0$$

$$\zeta_1(t) = 0, \quad t < 0 \quad (3\text{-}5)$$

$$\zeta_2(t) = \frac{e^{\frac{(t-\delta\tau)^2}{2\sigma^2} - i\omega_2 t}}{\sqrt{2\pi}} \quad (3\text{-}6)$$

where ω_1 and ω_2 are the central frequencies of the emitted photons, τ_c is the coherence time of the biexciton and σ is the width of the laser photon wave packet. The modes are normalised and defined as above so that $\int \varepsilon_\kappa(t)dt = 1$.

Contrary to a conventional 50:50 two-photon interference experiment, only one of the outputs of the beamsplitter is considered in the analysis and the interference effect is observed as bunching of photons instead of anti-bunching. The amplitudes corresponding only to the two cases where one photon is reflected and the other one transmitted (see Figure 3.1) are considered. The result is constructive interference of these two indistinguishable events and leads to a coincidence. Therefore, two photons at the beamsplitter output will indicate two-photon interference and bunching of photons at the detectors is expected. Assuming that one photon only from each source meet at the beamsplitter, the joint detection probability can be defined as in [87]. The two detectors in this setup measure coincidences in the same arm of the beamsplitter at time t and $t+\tau$ and therefore the minus sign in this expression is replaced with a plus sign. Integrating over detection time differences τ and time between emissions $\delta\tau$, the joint detection probability of detecting two photons at the same port of the beamsplitter is given by:

$$P(\tau, \delta\tau) = \int dt |\zeta_1(t)\zeta_2(t+\tau) + \zeta_2(t)\zeta_1(t+\tau)|^2 \quad (3\text{-}7)$$

$$P(\tau, \delta\tau) = \int dt \, [\zeta_1(t)\zeta_1^*(t)\zeta_2(t+\tau)\zeta_2^*(t+\tau) + \zeta_2(t)\zeta_2^*(t)\zeta_1(t+\tau)\zeta_1^*(t+\tau) + \zeta_2(t)\zeta_1^*(t)\zeta_1(t+\tau)\zeta_2^*(t+\tau) + \zeta_1(t)\zeta_2^*(t)\zeta_2(t+\tau)\zeta_1^*(t+\tau)] \quad (3\text{-}8)$$

We consider the dephasing process φ(t) associated with ζ_1 to be time invariant so that $\langle e^{i\varphi(t)} e^{-i\varphi(t+\tau)} \rangle = e^{-|\tau|/T2}$ [90]. Using the expression $\frac{1}{\tau_c} = \frac{1}{2\tau_r} + \frac{1}{\tau_d}$ from Chapter 2, integration over $\int dt \, \zeta_1 \zeta^*_{1(\tau)}$ in the last two terms in (3-8) is proportional to $e^{-\frac{|\tau|}{\tau_c}}$, showing that the coherence length of the dot photon is a crucial parameter of the probability.

Experimentally, we measure two correlations: $g_{||}^{(2)}$ from the photons that have left the same arm of the beamsplitter and have the same or parallel polarisation and $g_{\perp}^{(2)}$ from the photons that do not interfere. The probability of joint detection for co-polarised photons also needs to account for accidental coincidences from two laser photons or two biexciton photons and following analysis from [80], [85], [91] the calculated correlation becomes:

$$g_{||}^{(2)}(\tau) = \frac{(1+\cos(\Delta\omega\tau)e^{-\frac{|\tau|}{\tau_c}})\cdot 2n\alpha^2+n^2 g_B^{(2)}(\tau)+\alpha^4}{(n+\alpha^2)^2} \quad (3\text{-}9)$$

where $\Delta\omega = \omega_2 - \omega_1, n$ & α^2 are the biexciton and laser photon intensities respectively and $g_B^{(2)}$ is the autocorrelation function of the biexciton emission. From the interfering term of the function, an oscillatory behaviour or quantum beat is expected in the presence of a frequency difference between the two photons. This phenomenon will be verified experimentally in 3.6.2. The exponential coefficient describes how the interference is limited by the coherence length of the biexciton photon. The second term refers to the probability of having coincidences from two dot photons and is directly related to the autocorrelation function of the biexciton.

Similarly, orthogonally-polarised photons give the correlation

$$g_{\perp}^{(2)} = \frac{n^2 g_B^{(2)}(\tau)+\alpha^4+2n\alpha^2}{(n+\alpha^2)^2} \quad (3\text{-}10)$$

No interference i.e. bunching of the photons is expected from this correlation, since the photons will be distinguishable. The correlation will display a dip at $\tau=0$ due to the anti-bunched nature of the quantum dot emission. The quality of the two-photon interference between the two light sources can be quantised by defining the visibility V:

$$V_{TPI}(\tau) = \frac{g_{\parallel}^{(2)}(\tau)-g_{\perp}^{(2)}(\tau)}{g_{\perp}^{(2)}(\tau)} \quad (3\text{-}11)$$

where $g_{\parallel}^{(2)}(\tau)$ and $g_{\perp}^{(2)}(\tau)$ are the interfering co-polarised photon and non-interfering cross-polarised photon correlations, respectively. High contrast between the second-order correlations representing the co- and cross- polarised traces indicates high interference visibility.

3.4 Modelling of two-photon interference

It can be shown that interference can be achieved despite the two photons coming from two dissimilar sources using a numerical model based on the analysis above. The term $g_B^{(2)}$ was obtained experimentally under an electrical bias at 203 MHz frequency and the correlations were convolved with the detectors' response function. Figure 3.3 shows the result of two-photon interference, where the plots represent a full bias period. In (a) the correlations $g_{\parallel}^{(2)}(\tau)$ and $g_{\perp}^{(2)}(\tau)$ are plotted against detection time τ. The correlation traces peak around $\tau=0$ as a result of the pulsed character of the sources. The

cross-polarised trace follows the biexciton $g_B^{(2)}$ profile with a dip at τ=0 and coincidences around it due to dot re-filling. The co-polarised trace displays a peak at τ=0, which represents the coincidences due to two photons interfering and exiting the beamsplitter together. The contrast between the two traces occurs because of the interfering term in $g_{\parallel}^{(2)}(\tau)$. The calculated TPI visibility is plotted in (b) and exceeds 0.5. TPI is only observed around τ=0 and the visibility width is limited by τ_c, as expected.

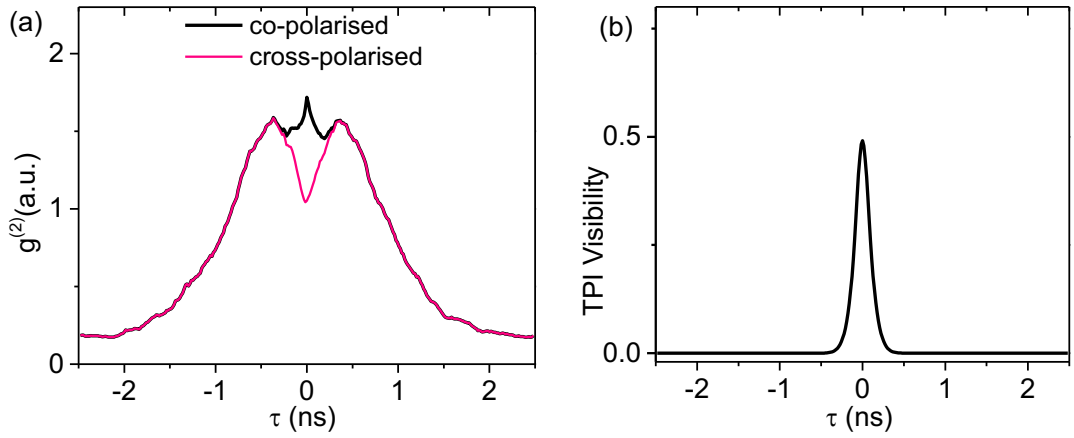

Figure 3.3: Modelling of two-photon interference between a laser and a biexciton photon with equal intensities. Input parameters: σ=140 ps, τ_c=140 ps, Δω=0; pulse period=4.96 ns. (a) Correlation traces for the co-polarised interfering photons and the cross-polarised photons. (b) Corresponding TPI visibility derived from (a).

3.4.1 TPI & energy detuning

The expression in (3-8) includes the term $cos(\Delta\omega\tau)$, which is dependent on the energy detuning Δω between the two sources. As a result, a non-zero frequency difference between the two photons will manifest as a quantum beat signal in the $g_{\parallel}^{(2)}(\tau)$ correlation. As with other analyses [80], TPI and two-photon coalescence can still be observed at τ=0 even if the photons are distinguishable in frequency. Figure 3.4 (a) shows the expected second-order correlations when Δω=10 & 30 μeV, where bunching of photons is expected at zero delay. With increasing Δω the beat signal oscillates faster and the bunching peak becomes narrower. The calculated TPI visibility for a range of Δω is shown in (b). In the case of increasing frequency difference between the two photons, the visibility peak drops, as it is limited by the resolution of the detectors.

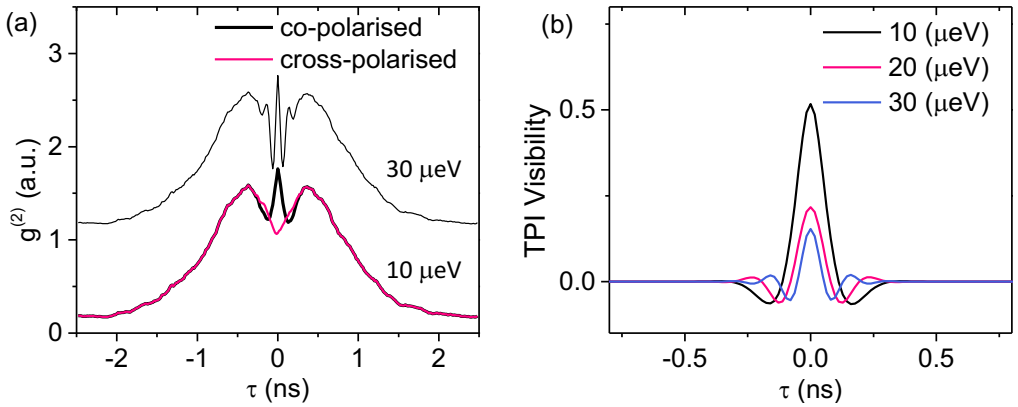

Figure 3.4: Modelling of two-photon interference between a laser and a biexciton photon with finite detuning. Input parameters as above. (a) Correlation traces for the co-polarised interfering photons and the cross-polarised photons, Δω=10 μeV. (b) Calculated TPI visibility for Δω=10, 20 & 30 μeV.

3.4.2 TPI & photon wave packet characteristics

Figure 3.5 (a) shows the effect the coherence time of the biexciton photon and the laser pulse width (parameters τ_c and 2σ, respectively) have on the maximum TPI visibility. High visibility points can be achieved for a range of τ_c. However, the high visibility points occur for short laser pulse widths. In this regime, the wave packet profiles are comparable in width i.e. τ_c and 2σ. The TPI visibility reduces for $\tau_c \ll 2\sigma$ when the laser approaches CW operation; given that the intensity ratio of the sources was kept constant (1) for this calculation, the Gaussian profile of the laser pulse reduces in amplitude for large σ. Figure 3.5 (b) shows the corresponding wave packet amplitude ratios for the points in (a). The visibility diminishes for the lowest amplitude ratios. It can be thus concluded that high TPI visibility for photon pulses can be achieved for short laser wave packet width that match in amplitude and width.

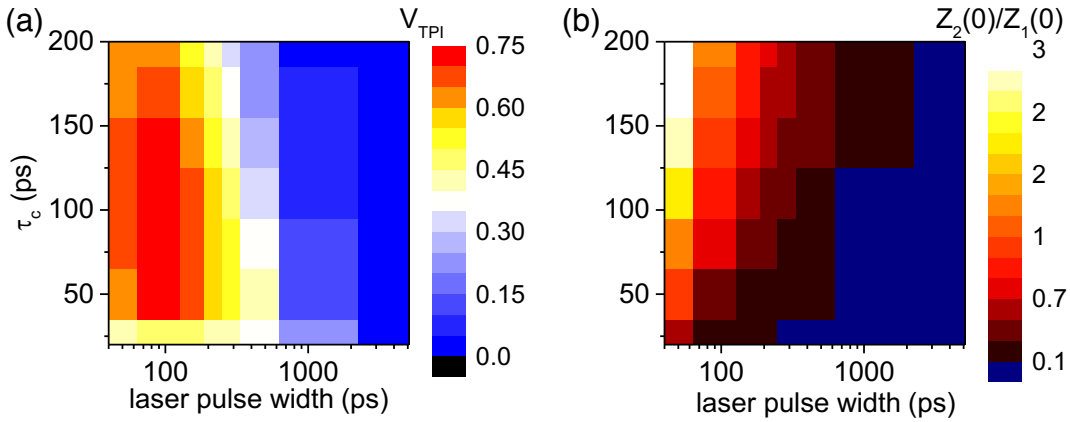

Figure 3.5: (a) Maximum TPI visibility and (b) Wave packet amplitude ratio as a function of biexciton coherence time (τ_c) and laser pulse width (2σ). $Z_2(0)$ & $Z_1(0)$: laser & biexciton wave packet amplitudes for both mode intensities normalised to 1.

3.4.3 TPI as a function of delays δτ and τ

The two wave packets are emitted with a time difference δτ and detected with a time difference of τ, as shown by Figure 3.2. Figure 3.6 (a) shows how the interference varies as a function of δτ and τ, within a time window much shorter than one excitation period (1 period = 4.9 ns). Figure 3.6 (b) is the cross-section of (a) for τ = 0. The maximum visibility is found at a small positive delay, due to the dissimilar nature of the photon wave packet profiles. This is the result of the joint detection probability being the integral of a Gaussian function and an exponential decay, which are defined with different time limits in (3-5) and (3-6). The TPI visibility peak is restricted by the width of two wave packets and has a width similar to the photon coherence length τ_c (~140 ps). As a result, coincidences within this window will be post-selected and account for the maximum TPI visibility.

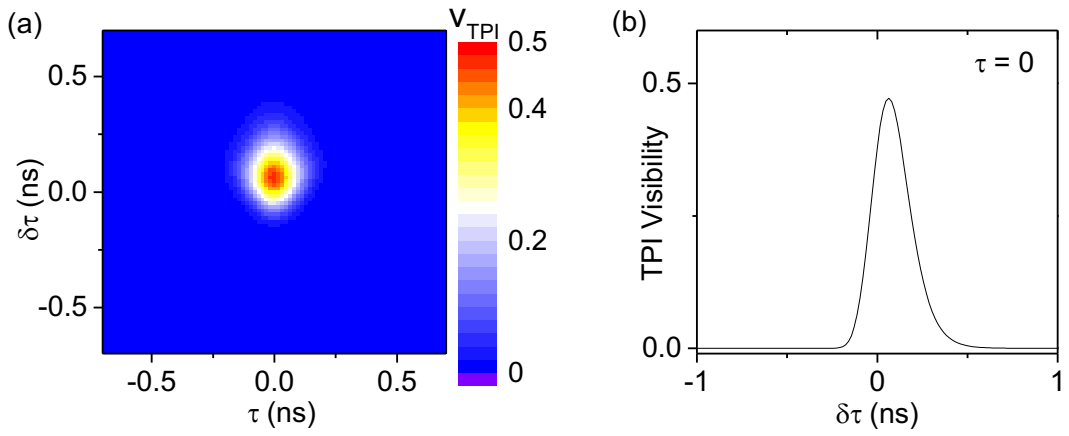

Figure 3.6: (a) TPI Visibility as a function of δτ and τ. (b) TPI Visibility as a function of δτ at τ=0. Laser wave packet defined as a Gaussian where $2\sigma = \tau_c$.

3.5 Experimental details

3.5.1 Pulsed E-LED operation

The operation of the E-LED under DC bias has been exhibited in numerous past experiments. For practical applications, though, triggered emission from the device and consequently synchronised detection would be desirable. The design of a small size device has enabled clocked operation and can reach high switching frequencies. However, pulsed electrical operation can prove to be a complex process that requires a good understanding of the excitation dynamics. It is known from other reports that the emission characteristics, including the coherence length of a single photon and wavelength, are directly influenced by the electric field the QD is in [47], [92]. It is therefore expected that the application of a varying electric field across the device will alter the emission characteristics dramatically, compared to what was achievable under DC current injection. We are thus interested in investigating the effects of pulsed operation on the exciton-biexciton pair properties.

In theory, operation under large A.C. voltage amplitudes will broaden the emission linewidth. It is the result of the applied electric field variation across the diode, which causes a Stark-shift in emission [47]. A broadened linewidth indicates reduction in the coherence length of the exciton and biexciton photons. Moreover, the same effect limits the post-selection coincidence window, thus reducing the post-selected maximum entanglement. The challenge therefore lies in achieving pulsed operation of the

device at fast switching frequencies while maintaining good biphoton entanglement characteristics. Using time-resolved spectroscopy, we can study the character of the emission for different frequencies and AC voltage biases.

Figure 3.7 shows time-resolved measurement for the biexciton and exciton photons at an AC bias frequency of 253MHz. The biexciton emission has clearly pulsed characteristics, with the emission decay being well contained within the electrical pulse width. The exciton emission on the other hand has some DC component and the emission does not decay completely before the next excitation pulse. The reason for this is due to the radiative lifetime being longer than the excitation period.

For the TPI measurements described in this chapter the bias conditions are as follows: a pulsed electrical signal is supplied to the device, with a high pulse at 2.5 V and a low pulse at 0.75 V. The high or "on" pulse has a width of 450 ps, which is shorter than the biexciton lifetime. It should also be noted that the emission intensity and shape are dependent on the bias function and power delivered to the device. For this reason, pulsed excitation generally results in reduced emission intensity, since the diode is not continuously in the "on" state.

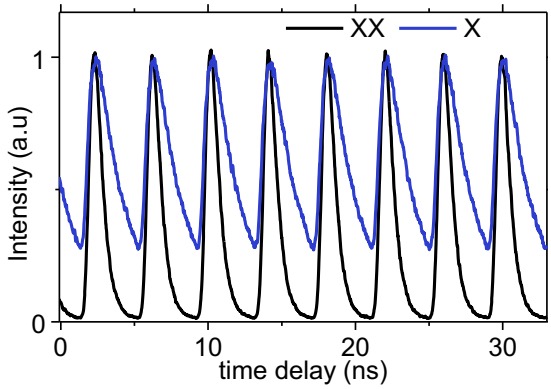

Figure 3.7: Pulsed emission characteristics for the biexciton and exciton at a bias frequency of 253 MHz.

3.5.2 Laser Modulation

The biexciton photon will be used as one of the beamsplitter inputs, whereas a laser photon will constitute the dissimilar source made to interfere with it. Indistinguishability of the photons is one of the pre-requisites of their successful interference, as explained above. The time-resolved trace of the laser was adjusted to match the biexciton wave packet by varying the pulse width of the modulating bias function. By using a wavelength-tuneable laser, the laser photons are made to have the same emission

energy as the biexciton photons in Figure 3.8 (a). The tuneable CW semiconductor laser diode was used in conjunction with a Mach-Zehnder intensity modulator (I.M.). The modulator works by applying an electric field on the device, which applies a phase shift on the incoming light. By correctly choosing the modulator 'off' bias, and applying pulses some of the output light is suppressed and the collected light will be in pulses. A time-resolved correlation of the wave packet is shown in Figure 3.8 (b), in which the pulses can be fitted with a Gaussian function of σ=405 (0.004) ps. The frequency of these pulses is determined by the bias applied on the E-LED, as the two are synchronised.

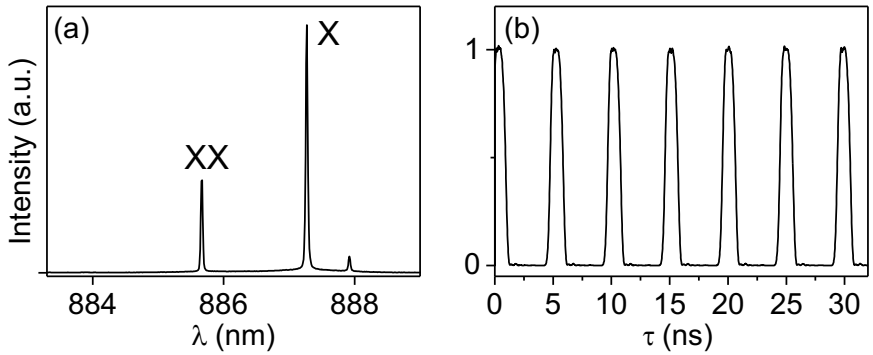

Figure 3.8: (a) Quantum dot spectrum, obtained under pulsed excitation. (b) Time-resolved trace of the laser pulses. Modulator extinction ratio: 1.33×10^3.

3.5.3 Experimental setup

The two-photon interference was measured using the setup depicted in Figure 3.9. The biasing frequency for both E-LED and laser is synchronised at 253MHz. This is achieved by observing the arrival of the photons in a time-resolved manner and adjusting the electronic path length accordingly, so that the delay $\delta\tau$ is varied. Light from the laser is modulated into pulses and then filtered using a transmission grating, to remove any unwanted frequencies, and polarised using a polariser plate. Light from the QD goes through a grating as well, in order to select the XX emission, and is then polarised as the laser photons. Photons from the two sources interfere on an unbalanced 95:5 beamsplitter, with 95% of the dot light and 5% of the laser light coupling to exit port 4. At this point, the laser: dot intensity ratio is defined by us, by integrating the detected photon counts, as a means of controlling and tuning the wave packet amplitudes. To create the non-interfering and the interfering coincidences separately, the light from port 4 of the 95:5 beamsplitter is split into P and S polarisations using a polarising beamsplitter. At this point, the polarisation controller voltages are adjusted so that the two outputs P & S have equal intensities.

The P-polarised light is finally divided into two using a 50:50 beamsplitter. This is the interfering component (co-polarised photons) and is detected using SSPDs at the two beamsplitter outputs, observed as a time-resolved correlation function. Assuming constructive interference from co-polarised photons, bunching should be observed. The non-interfering component of the light is measured using a third detector. Photons at this output are cross-polarised to the photons at SSPD1. With this third channel, a second correlation can be obtained. By comparing the two correlations, the visibility of two-photon interference can be measured as defined in (3-11).

Light from the other arm of the 95:5 beamsplitter is directed to the spectrometer, so that the spectrum of both sources can be automatically scanned during the experiment. This is required as the laser emission "drifts" with time and needs to be re-tuned to the biexciton emission wavelength. The spectrum of the biexciton may also change slightly, due to the small variations in temperature. It was also important to keep the laser to dot intensity ratio constant, which was done using the spectra from the 5% beamsplitter port and by adjusting the laser attenuation accordingly.

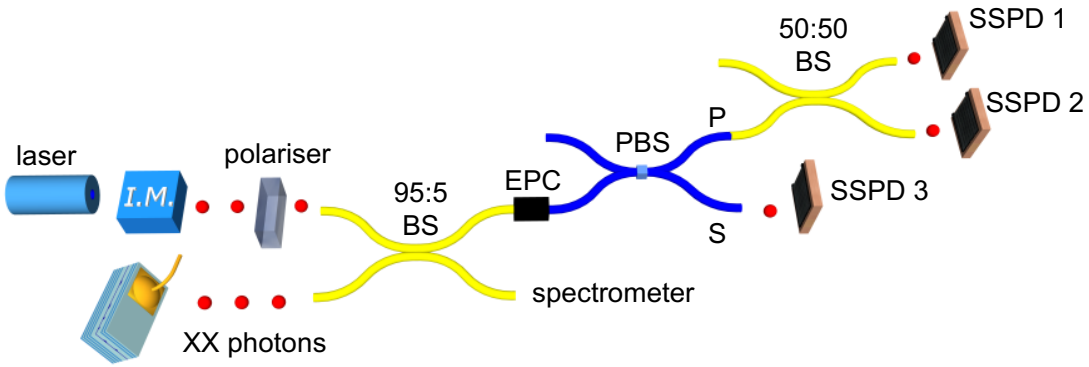

Figure 3.9: Two-photon-interference setup schematic. Photons from the two sources photon interfere on a 95:5 unbalanced beamsplitter. In this configuration, the collection of dot photons is maximised. The interference between the laser and dot photons should be observed as bunching, as they exit the BS port together. The other BS output port is used to adjust the intensity and detuning of the laser photons, throughout the experiment. Output modes of the PBS: P⊥S. The correlation produced from SSPD 1 and 2 is constructive interference because of the bunching effect at the first BS. The correlation between SSPD 1 and 3 will show absence of bunching, as the pair is cross-polarised. EPC: Electrical Polarisation Controller, I.M.: Intensity modulator, PBS: Polarising Beamsplitter.

3.6 Results & Discussion

The next step is to explore the effect of the various parameters dictating the TPI between a laser photon and a biexciton photon in pulsed mode. Ultimately, the maximum quantum relay fidelity will

depend on optimizing the bias conditions so that TPI visibility is maximum throughout the experiment. Following from the theoretical discussion, the major parameters that will be varied are the energy detuning $\Delta\omega$, the delay $\delta\tau$ and the laser: dot intensity ratio. The excitation conditions of the two sources were as defined in 3.5.1 and 3.5.2 and were not varied. It is worth noting that $\delta\tau$ is difficult to define under experimental conditions, since the two wave packets are not perfect Gaussian and exponential decay functions, with maximum amplitudes at $\delta\tau=0$. For this reason, the $\delta\tau=0$ is re-defined as the maximum wave packet overlap point.

3.6.1 Pulsed TPI between a laser & biexciton photon

Figure 3.10 shows the second-order correlations for the co- (red) and cross- (blue) polarised photons exiting the same output port of the beamsplitter. The detuning $\Delta\omega$ between laser and biexciton photons is 0. The pulsed character of the correlations, with several peaks separated by the bias pulse period, can be observed. The co-polarised trace shows increased coincidences and a peak around 0, indicating the bunching effect of constructive interference. The absence of this effect can be observed for the cross-polarised case. The dip of the blue trace is attributed to the sub-Poissonian character of one of the source photons and is limited by the resolution of the detectors and the relative contribution of the Poissonian source, as the two $g^{(2)}$ components are added, as in (3-10). Here, the laser: dot intensity ratio is 0.5, so the laser photon contribution is not limiting the dip. The same parameters therefore limit the calculated visibility peak width. The measured post-selected visibility shown in (b) peaks around $\tau = 0$ and reaches a value of 0.53 (0.08). The visibility eventually drops to zero, when the time delay surpasses the coherence time of the biexciton photons, which is ~140 ps. This follows well from the discussion in 3.3 and illustrates the need for longer coherence times, as a pre-requisite for quantum logic operations. The maximum post-selective interference occurs at $\tau = 0$, which means that the laser and biexciton photons arrive at the detectors at the same time. The visibility peak width is also limited by the quantum dot re-excitation, which translates to non-zero biexciton $g^{(2)}$ around $\tau = 0$ and a narrower dip. Ideally, the central peak of the blue correlation would have no contributions from the single-photon emitter, but only from the laser photons. If the $g_B^{(2)}(0)$ was lower or the dip wider with reduced dot re-excitation features, the post-selected TPI visibility would be higher.

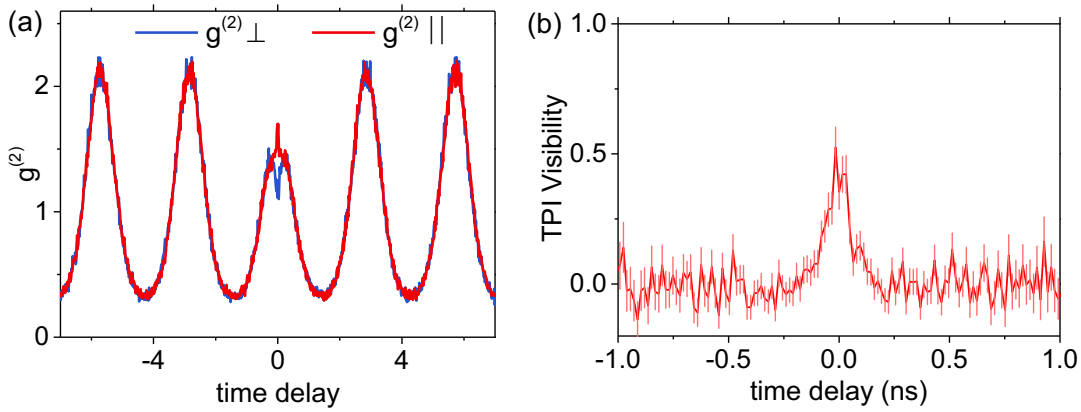

Figure 3.10: Normalised second-order correlations $g^2_{||}$ and $g^2_{\perp}$ for the biexciton photons. (b) Corresponding two-photon interference visibility.

3.6.2 Quantum Beat of two single photons

The two photons are adjusted to have the same frequencies when observing HOM (Hong-ou-Mandel) interference. In the case when there is a difference in the frequency of the interfering photons, quantum beats may be observed [80], [91], [93]. In Figure 3.11 the effect is observed for energy detuning Δω ranging from 0 to 40μeV. Here the laser: dot intensity ratio was set to 0.5 and δτ = 24.3 ps. The highest visibilities were observed when the laser is made to have an emission wavelength of only a few μeV away from the XX emission wavelength. Significant drop in visibility is observed for a large detuning of 40 μeV.

In Figure 3.11 (a) the measured $g^{(2)}_{||}$ correlations for a range of Δω demonstrate the effect of the term $\cos(\Delta\omega\tau)e^{-|\tau|/\tau_c}$ from (3-9). Bunching of photons is observed for all energy detuning values at τ=0, verifying quantum interference between the two photons. Faster oscillations are observed for increasing energy detuning, as expected. Away from τ=0 the co- and cross-polarised traces overlap perfectly, as TPI is limited by the coherence length τ_c of the biexciton. The corresponding TPI visibilities are plotted in Figure 3.11 (b). The visibility peak reduces from 0.53 (0.07) when Δω=0μeV to 0.23 (0.06) for Δω=40μeV. This is the result of a narrower bunching peak that cannot be resolved with the resolution-limited detectors. The results match well with the modelled correlations in Figure 3.4.

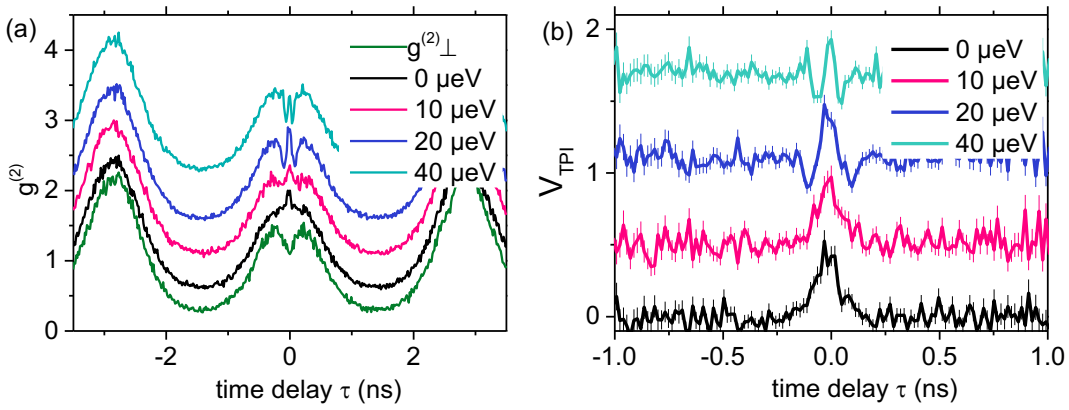

Figure 3.11: (a) Quantum beats in pulsed TPI. Measured $g_{||}^{(2)}$ for energy detuning Δω=0, 10, 20 & 40 μeV (traces have an offset for clarity). (b) TPI visibility calculated from the correlations in (a).

3.6.3 Effect of time delay & intensity ratio on the Visibility

The effect of varying the photon emission delay δτ is investigated. Figure 3.12 (a) summarises the dependence of the two-photon interference visibility as a function delay time δτ and the laser: dot intensity ratio (Δω=0). In order to make the trends visually clearer, the averaged measurements over all Δω=0, 10, 20 and 40 μeV are also plotted in (b). From the plots we can make some interesting observations: 1) the visibility maximises for a small time delay between the overlapping wave packets. As discussed in 3.4.3, this is the result of dissimilar wave packet profiles. The visibility is surprisingly robust for a wide range of time delays, but drops off around δτ~400 ps. This is directly comparable to the laser photon wave packet width (σ=405 ps), since away from this region the pulse is 'off'. This effect is also shown in Figure 3.12 (a). 2) The visibility is higher for the lower intensity ratios i.e. 0.5–0.85. The highest is obtained for the smallest laser:dot intensity ratio (0.5), for which the peak reaches 0.54. This happens because the contribution of the laser coincidences in the co- and cross- polarised correlations increases. The visibility is defined by $V_{TPI}(\tau) = \left[g_{\|}^{(2)}(\tau) - g_{\perp}^{(2)}(\tau)\right] / g_{\perp}^{(2)}(\tau)$ (3-11). Since the laser intensity term a is of second order in the denominator and only of first order in the numerator, the visibility is expected to degrade as the laser:dot intensity ratio increases.

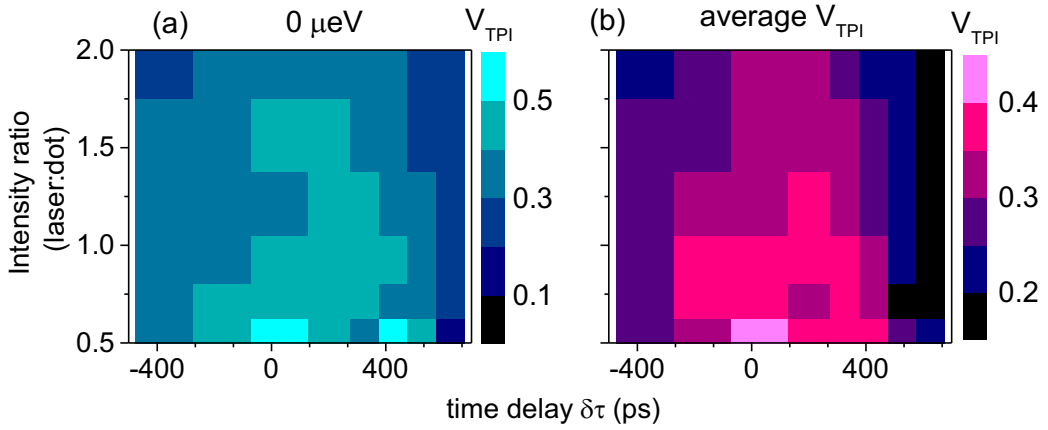

Figure 3.12: TPI Visibility plots as a function of laser:dot intensity ratio and emission delay time δτ. (a) Δω=0 μeV. (b) Averaged visibility over all 4 measurements Δω=10, 20 and 40 μeV.

In order to study the trends more clearly, Figure 3.13 shows the TPI visibility as a function of δτ in (a) and intensity ratio in (b). In (a), the visibility is not symmetrical around δτ=0, but rather follows the overlap of the dissimilar wave packets. The points can be fitted with a maximum at δτ~24 ps, as expected. From the results in (b), we see that the TPI visibility reduces for increasing intensity ratio but can still be high, whereas the effect of Δω is more prominent.

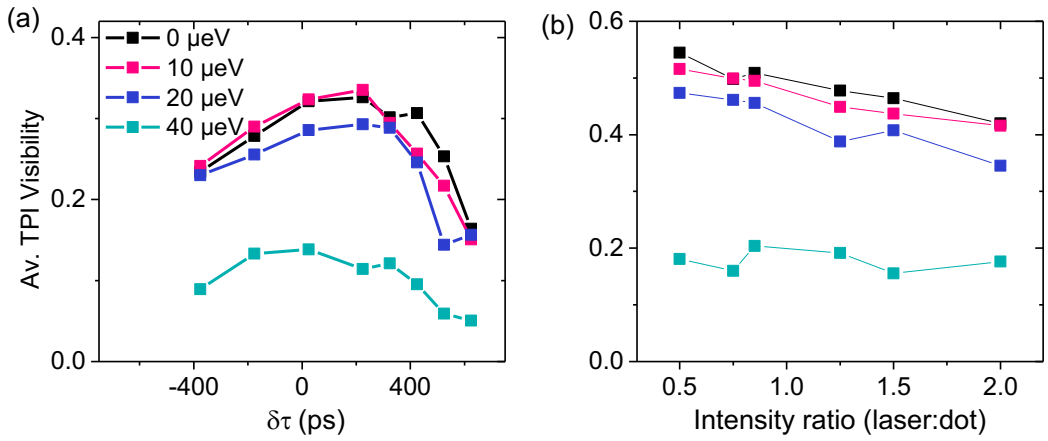

Figure 3.13: (a) TPI visibility as a function of delay. (The points correspond to the visibility measurements averaged over the range of intensity ratios). (b) TPI visibility as a function of laser:dot intensity ratio. (The points correspond to the visibility measurements averaged over the range of δτ).

3.7 Conclusions

This experiment was the first step towards achieving quantum teleportation of a qubit state from an electrical-driven E-LED under clocked MHz bias. Biexciton photons have been shown to interfere with laser photons during the same synchronised cycle with high interference visibility.

As expected, the highest two-photon interference visibilities occur for $\tau=0$ delay and decrease for bigger delays. The visibility is maximum for 0 energy detuning between laser and biexciton photons, remains quite high (~0.45) for small detuning values and rapidly reduces for 40 μeV of detuning. The results generally show good two-photon interference visibilities, with the highest being 0.57 (0.1). The detector resolution and the biexciton emission coherence length limit the measured visibilities. These results will allow us to proceed with the quantum teleportation-based relay scheme, for which the optimal conditions for two-photon interference will be set. From both theoretical calculations and experimental measurements, we can see that the visibility from two-photon interference is strongly affected by the coherence time of the emission. With the biexciton coherence XX time as ~140 ps and by setting the optimum parameters for pulse width, intensity ratio and detuning, we have managed to achieve a visibility between 0.45-0.55. In combination with a high entanglement fidelity of the QD photon pair, the quantum relay experiment was implemented.

Chapter 4 Quantum Relay over 1km of fibre

4.1 Introduction

Quantum cryptography [94], [95] refers to encryption schemes, which allows secret keys to be distributed between two users over a quantum channel, with security established by the completeness of quantum mechanics [60]. A key element of quantum technologies is quantum teleportation, which can provide a reliable and efficient way to transfer quantum information between two remote parties. Several experimental demonstrations have been implemented inside and outside the lab [78], [96]–[103], using various substrates and qubit systems. A practical limitation of teleportation-based quantum communication is the achievable range, since fibres introduce losses and detectors can be noisy. The challenge of extending the distance of secure QKD can be addressed by introducing more parties and creating multi-node networks. A possible solution comes in the form of quantum relays or repeaters [104], [105], which can be implemented for the teleportation of qubits from a sender to a receiver, without the two parties sharing entanglement. In quantum relay schemes [106]–[108], long-distance distribution of entanglement can be achieved by dividing the channel into sections and sending a different photon across each one. In contrast to quantum repeater schemes, quantum relays do not require quantum memory, which is not compatible with current technology. Another advantage of quantum relays is the potential to improve the signal-to-noise ratio, since all the qubit operations are performed locally. The increased SNR at the detectors is achieved because the entangled photons are distributed to separate locations, limiting the distance that each photon has to travel [107]. It has been shown that better SNR can be achieved as more relay nodes are added as a chain [106].

Following from the discussion in Chapter 3, a quantum teleportation-based relay scheme was implemented, conditioned upon achieving high two-photon interference visibility between laser and quantum dot photons. This chapter discusses the operation of a quantum relay over 1 km of optical fibre using electrically generated entangled photons to teleport photonic qubits encoded on weak coherent pulses emitted by a laser. Weak coherent pulses with a Poisson distribution are compatible with current QKD technologies, in the absence of perfect single-photon sources [109]. The setup provides a compact alternative to other quantum relay configurations [108], given that the entangled pair source is a

simple semiconductor E-LED. The advantages of a quantum dot-based source over methods like SPDC [110], in combination with the distribution of entanglement over a significant distance, provide a proof of principle experiment for scalable network implementations. The successful teleportation of four input states corresponds to an average relay fidelity of 0.90 ± 0.03, well above the classical threshold of 0.75 and high enough to allow error correction.

4.1.1 Fidelities for different protocol sets

Before proceeding with the implementation of a teleportation-based quantum relay over 1 km, quantum teleportation tests have been carried out. The initial assessments have tested quantum teleportation in all three bases, rectilinear, diagonal and circular, in order to deduce the best strategy to follow regarding the quantum relay protocol. In these experiments, lower resolution detectors were used, which compromised the highest teleportation fidelity achieved, compared to the actual quantum relay experiment. Protocols that make use of quantum teleportation by encoding in either 4 or 6 polarisation states were considered [111], [112]. Reducing the number of teleportation bases from 3 to 2 would give a practical advantage to the laboratory implementation, as more photon counts reduce the error on the individual basis measurements. On the other hand, the fidelity threshold for quantum teleportation is higher when using 2 bases (3/4) compared to using 3 bases (2/3). An efficient BB84 protocol [113], in which the input states are not used with equal probabilities, (i.e. biased choice of basis) was implemented. Such a protocol allows the exchange of keys predominantly on one of the two bases, yielding higher efficiency and lower Quantum Bit Error Rate (QBER) than with the standard BB84 protocol.

With the presence of finite FSS, the teleportation in the superposition bases yields lower fidelity than in the logical basis. In order to alleviate big differences between the maximum and minimum teleportation fidelity, two orthogonal bases other than the three standard equatorial ones were considered, as illustrated in Figure 4.1. In Bloch sphere representation, these two bases lie in between the rectilinear and diagonal bases and their polarisation state vectors lie at 45° to the corresponding pure equatorial states.

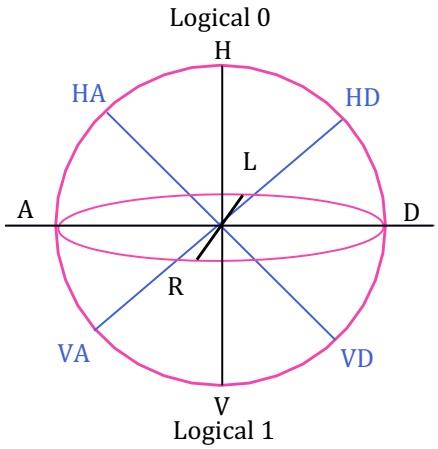

Figure 4.1: Bloch sphere and polarisation state representation. Input polarisation states HA, HD, VA, VD lie on the orthogonal basis between the rectilinear and diagonal bases and are at 45° angles to the respective states.

In conclusion, quantum teleportation in all the 10 qubit states mentioned above was tested to determine the best protocol for the quantum relay implementation. The assessment of the four protocol strategies in consideration and how they would perform using one-way error correction is given in the Appendix (A- 1). From these preliminary quantum teleportation results, it was therefore decided that the implementation of the efficient 4-state BB84 scheme using the rectilinear and diagonal bases would give the optimum results.

4.1.2 Characterising Entanglement

After verifying that the QD biexciton photons can interfere with laser photons and achieve high two-photon interference visibility, the entanglement properties of the source need to be assessed, before proceeding with quantum teleportation. Following from the discussion in 2.5.2, the entanglement fidelity may be determined directly from polarisation-dependent correlations between the exciton and biexciton photons made with the same bases for both. The relevant measurements in the rectilinear, diagonal and circular bases are shown in Figure 4.2 (a)-(c) and were obtained as second-order correlations using the setup illustrated by Figure 2.12. The correlations in the superposition bases, namely circular and diagonal, reveal the nuclear polarisation fluctuations in the quantum dot and hence non-zero exciton FSS. As expected from the switching between the on and off state of the device, distinct peaks in the correlations show the pulsed character of the emission. The measured time-dependent correlations in the superposition states (diagonal and circular bases) exhibit fast oscillations caused by finite FSS of the excitons. Another feature is the zero-delay dip, which represents the small probability

of an X photon being emitted before an XX photon. Similar observations and discussion about entanglement measurements are found in 5.7.2.

The entanglement fidelity to the maximally entangled Bell state $|\Psi^+\rangle$ was calculated using the formula in (2-8) and it reaches a maximum of 0.93±0.002, well above the classical threshold of 0.5 [Figure 4.2 (d)]. Note that this is the highest entanglement fidelity obtained for an electrically injected QD source and under AC excitation.

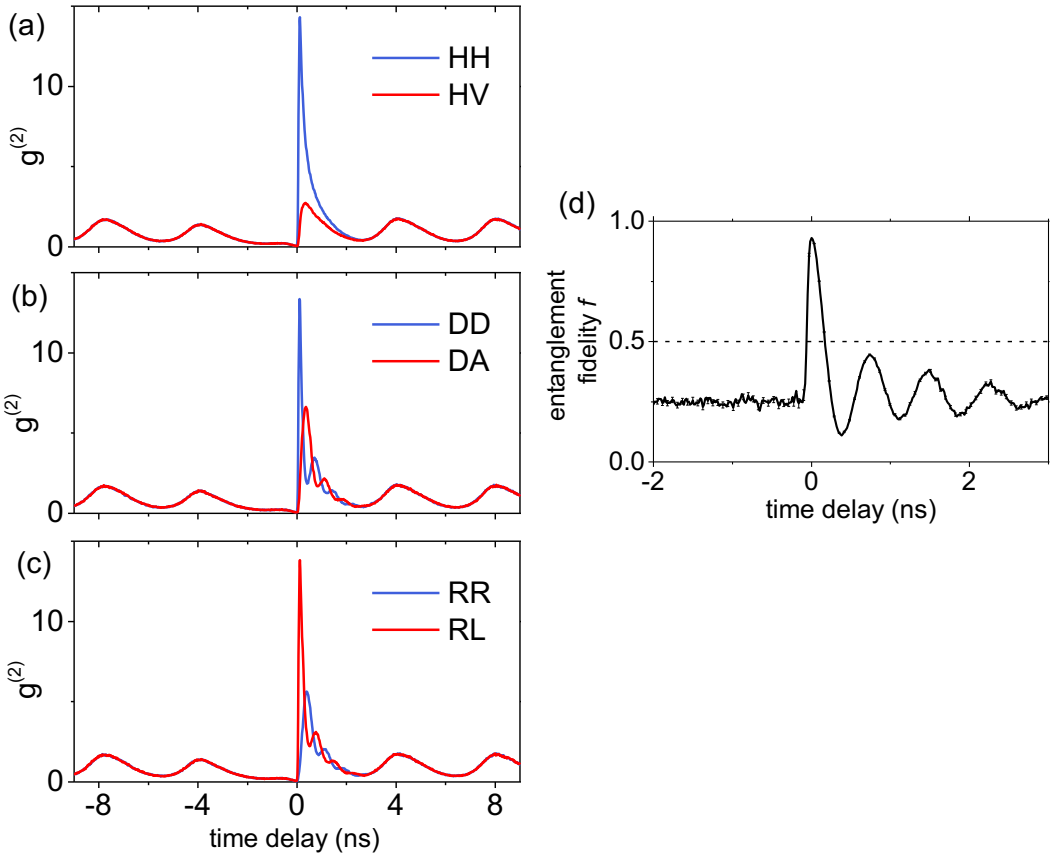

Figure 4.2: Entanglement measurement for the exciton-biexciton pair under pulsed electrical excitation. Polarisation-dependent $g^{(2)}$s in the (a) rectilinear, (b) diagonal and (c) circular basis. (d) Entanglement fidelity *f* to the static Bell state Ψ^+ derived from the $g^{(2)}$s.

4.2 Quantum teleportation setup

The quantum relay scheme implementation involves the coincident detection of the laser, the biexciton and exciton photons. The input qubits in the form of laser photons interfere with ELED biexciton

photons on a highly imbalanced beamsplitter, where $|k_t| >> |k_r|$, as depicted by Figure 4.3 and similarly to the two-photon interference experiment in Chapter 3. In contrast to other teleportation setups [59], the Bell state measurement is performed using detectors resolving polarisations only at one of the beamsplitter outputs , which is the efficient beamsplitter output port in terms of biexciton counts in the Figure 4.3 diagram. A successful BSM projects the detected photon pair onto the symmetric Bell state $|\Psi^+\rangle$.

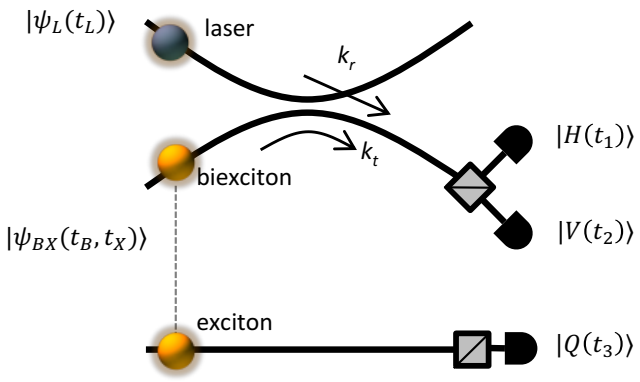

Figure 4.3: Quantum Relay diagram. Input qubit laser photons and biexciton photons interfere on a beamsplitter with transmission and coupling amplitudes k_t and k_r. A polarising beamsplitter then sends the photons to a pair of detectors aligned to a certain measurement basis. The exciton photon is measured in a state Q by the third detector.

The quantum relay scheme implemented here adopts the 4-state protocol. Teleportation of 4 polarisation states in two orthogonal bases on the Bloch sphere was evaluated in order to extract the average quantum relay fidelity. The first pair of detectors performs a Bell-state measurement (BSM) in the rectilinear basis spanning states $|H\rangle$ and $|V\rangle$ and is always aligned to the state $\frac{|H_L V_B\rangle + |V_L H_B\rangle}{\sqrt{2}}$, where subscripts L and B denote a laser and a biexciton photon respectively. We will therefore refer to the rectilinear basis states as logical or polar. The two vector states of the diagonal basis are then a superposition of $|H\rangle$ and $|V\rangle$ such that $|D\rangle = \frac{|H\rangle + |V\rangle}{\sqrt{2}}$ and $|A\rangle = \frac{|H\rangle - |V\rangle}{\sqrt{2}}$. The Receiver's detectors should be randomly switching alignment through all four states, according to the protocol. Input qubits are represented by the encoded laser photons and are teleported to the corresponding state as:

$$\cos(a)\,|H_L\rangle + e^{ib}\sin(a)\,|V_L\rangle \rightarrow \cos(a)\,|V_X\rangle + e^{ib}\sin(a)\,|H_X\rangle \quad (4\text{-}1)$$

Using the experimental setup and following from the algebra in Chapter 1 and (4-1), the teleportation state transformations from the input qubit state to the Receiver's detectors are $|H\rangle \rightarrow |V\rangle, |V\rangle \rightarrow |H\rangle, |D\rangle \rightarrow |D\rangle$ and $|A\rangle \rightarrow |A\rangle$. The Receiver's detectors will measure the correct 'expected' and their orthogonal 'unexpected' states, assuming they are aligned to the right basis.

4.2.1 Optimum teleportation conditions

A theoretical model was developed for this experiment in order to simulate the experimental conditions and make computational calculations [114] (see Appendix). The computational model was used to identify the optimum teleportation conditions in order to maximise the quantum relay fidelity. In this model, the laser photon wave packet intensity I_L was defined as a Gaussian function, which is a satisfactory approximation of what was observed experimentally (details about the laser photon pulses are given in 4.3.1). Some of the terms in this model refer to the dot emission profile and were obtained experimentally, namely the single biexciton and exciton photon intensities $I_B(t_B)$ and $I_X(t_X)$. The rest of the terms were calculated from time-resolved measurements as a separate experiment under the actual relay configuration, in the absence of input laser photons, so that the dot emission components could be probed. For instance, correlations between biexciton and exciton photons to determine the term $g_{BX}^{(3)}(t_B, t_X - t_B)$ for co- and cross-linearly polarized states were measured. The entangled biphoton fraction $g_{BXe}^{(2)}$ was extracted from half the difference between these correlations and the unentangled photon fraction $g_{BXu}^{(2)}$ was extracted from the uncorrelated component of these measurements. Similarly, the correlations between pairs of biexciton photons $g_{BB}^{(2)}(t_1, t_2)$ were directly measured. It is safe to assume that imperfections in polarization recovery and timing jitter are already represented in the above terms, since the same physical measurement system was used for their measurement as for the actual experiment.

In order to maximize teleportation fidelity that could be obtained experimentally, the expected maximal teleportation fidelity was calculated as a function of laser pulse intensity, width, and delay relative to the biexciton photon. The results are summarized in Figure 4.4, which plots the calculated teleportation fidelity as a function of the pulse delay and width in (a) while the corresponding optimal laser intensity is shown in (b). The maximum point is observed for a laser delayed 0.5 ns relative to maximal overlap with the biexciton state, and for a pulse width of 0.8 ns. Note that these values are close to those eventually employed in the experimental implementation (see 4.3.1).

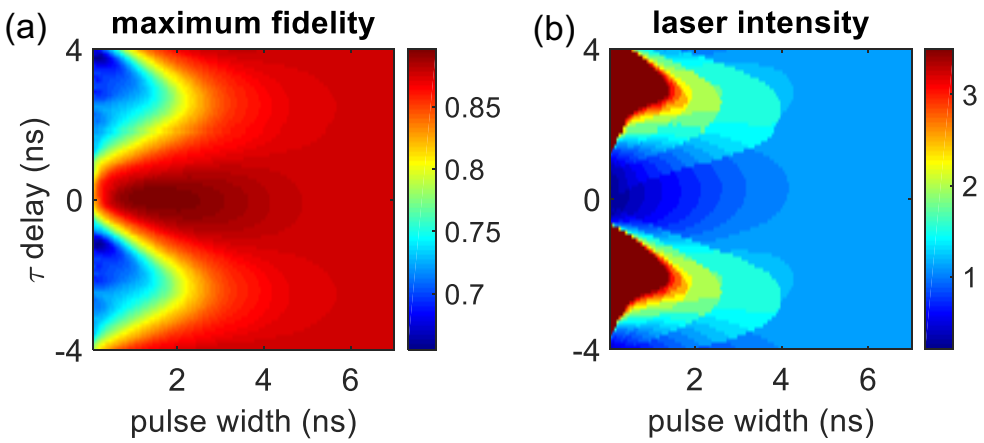

Figure 4.4: Theoretical model results for optimum teleportation conditions. (a) Calculated maximum relay fidelity as a function of laser pulse width and delay τ relative to the biexciton photon. (b) Corresponding laser intensity relative to biexciton intensity required (laser:dot intensity limit: 3.5) to achieve maximal fidelity.

The first observation is the concentration of high fidelity points around τ=0, whereas the low fidelity points are at longer time delays, with the minima being one excitation period apart. This may be explained as the effect of reduced two-photon interference at these points, as the two photon wave packets do not overlap optimally at the beamsplitter. The effect of the pulsed wave packet is also clear from the fact that the low fidelity points are observed for short pulse width. In other words, the two wave packets must be synchronised for maximum TPI and teleportation fidelity. It is also interesting to note that the maximum fidelity drops slightly for CW operation, which corresponds to a longer laser pulse width. In this case, the maximum fidelity remains constant for all time delays, since the laser wave packet has a long coherence time and still interferes with biexciton photons, irrelevant of their time of arrival at the beamsplitter. From (b) we can deduce that for minimally overlapping wave packets (i.e. at time delays away from 0), the maximum fidelity is low even for high laser intensity. Similarly, lower laser intensity is required to achieve high fidelity when the two wave packets are matched in time of arrival and wave packet profile (i.e. shorter laser pulses). In conclusion, the calculations here show that the maximum achievable relay fidelity depends on successful TPI between the laser and biexciton photons, which requires pulse synchronisation and wave packet profile matching when it comes to pulsed operation. Therefore, the laser pulse width, intensity and delay are important parameters that were carefully adjusted.

4.3 Experimental setup

The implementation of a quantum relay configuration is illustrated by Figure 4.5. There are four sections in this setup: The Sender, the Receiver, the E-LED and the BSM in the middle, each separated by a 350m- fibre spool. The Sender node is effectively separated from the end Receiver node by 1.05 km of optical fibre. Entangled photons emitted by the E-LED quantum dot are collected using single-mode fibre and distributed to separate nodes, which are 700 m apart. A diffraction grating is used to spectrally filter the biexciton and exciton photons, which are then sent to the BSM and Receiver nodes respectively. In this configuration, the Sender would like to share a key in the form of the input qubits with the Receiver, by quantum teleportation. The purpose of the untrusted node in the middle is to perform a Bell-state measurement and effectively 'relay' the photonic qubits from the first node to the end one. At the Sender node, an optical intensity modulator creates laser pulses from a continuous-wave laser tuned to the biexciton wavelength, as described in the previous chapter. The input qubits are encoded on these laser photons by the Sender. The polarised pulses are then rotated by a polarisation controller PC1 to encode the qubit, before transmission to the BSM node.

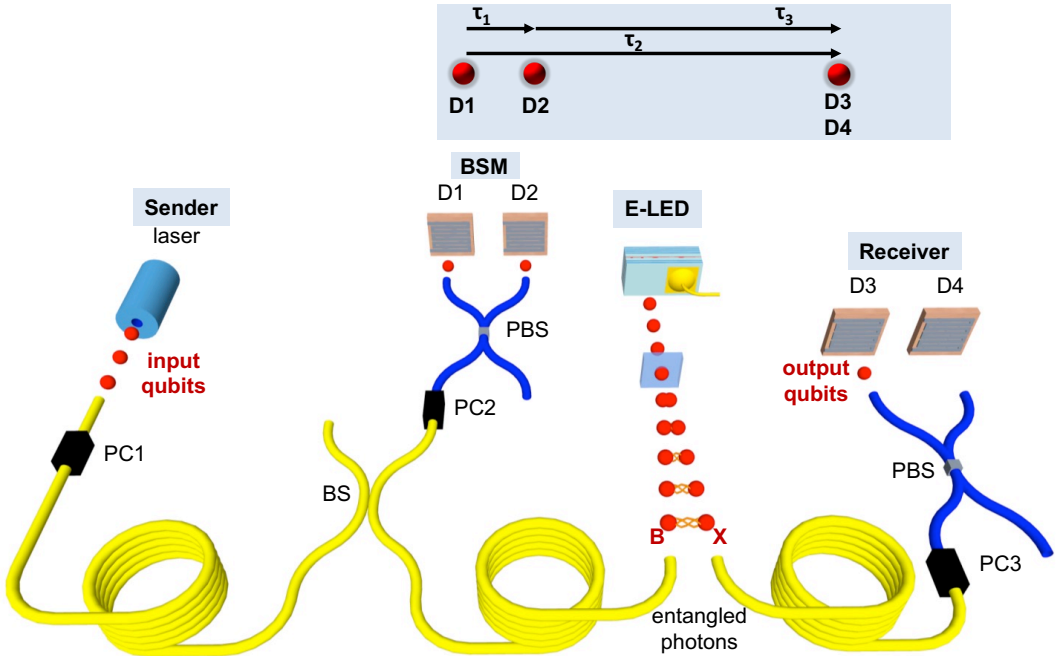

Figure 4.5: Quantum relay experimental set-up. The Sender encodes photons from an externally modulated laser diode with qubit states $|H\rangle, |V\rangle, |D\rangle$and $|A\rangle$, using a polarisation controller PC1, to be transferred to the receiver by quantum teleportation. The Sender and the Receiver are separated by 1 km of fibre and a BSM node in between. The BSM and receiver share an entangled pair of photons emitted from the E-LED. The input qubits interfere with biexciton photons (B) on beamsplitter BS. Once detectors D1 and D2 measure their state, teleported output qubits are detected with a polarising beamsplitter (PBS) at D3 and D4. All state calibrations at each node are done with polarisation controllers (PCs).

Under this configuration, the two entangled qubits are spatially separated by 700 m. Successful non-local quantum correlations were performed in 2 different bases, demonstrating long-distance teleportation and the potential for use in extending quantum networks.

4.3.1 Experimental details

In this experiment both the capabilities of the device as a triggered source and the distribution of entanglement from a quantum dot over a significant distance were exhibited. The major obstacles in achieving the first target is the degradation of the performance in terms of entanglement fidelity, photon coherence time and photon detection rates. As explained in the previous chapters, optimising the resistance and capacitance of the device has allowed for pulsed electrical operation at high switching frequencies of up to 253 MHz, without compromising entanglement fidelity or photon coherence.

The second target poses another concern that is pertinent to maintaining the system's polarisation stability, given the fibre length of 1km. The laboratory fibre setup is susceptible to strain and temperature fluctuations, which compromises the polarisation state of the photons carried by the fibres. Maintaining a high degree of polarisation of photonic states at all nodes is crucial to achieving high teleportation fidelity. For this purpose, the system was actively stabilised every 15 minutes throughout the duration of the experiment (~70hrs) using electrical polarisation controllers at each of the sections. The degree of polarisation for the input control qubits was maintained at 97.5±1.5%. Additionally, the 5% output port of the first beamsplitter was used to tune the laser to the biexciton wavelength using a grating spectrometer, to overcome laser or biexciton wavelength drifting effects. The average detuning between the two was at 0.12±1.7 μeV throughout the experiment.

For the input qubit photons at the sender section, a CW laser was externally modulated and synchronised with the dot driving frequency using a Mach–Zehnder optical intensity modulator, as described in the previous chapter. The generated laser pulses had a full width at half maximum of 0.95 (0.01) ns. The relative time-integrated intensities between laser and biexciton photons incident on detectors D1 and D2 was set to 0.85:1. The input qubit polarisation state was selected using a pseudorandom number generator and polarisation controller PC1 at a frequency exceeding the three-photon coincidence rate.

Figure 4.6 shows a schematic of the set of optics used for basis calibration and light collection during the quantum relay experiment. Two pairs of beamsplitters and a camera were in place to divide the QD light into two paths (blue arrows): one for imaging and one for detection purposes. A polarised white light source going through the same path (pink arrows) as the QD light and a motorised half-wave plate were in place to automatically calibrate the 4 states. During the calibration process, the QD emission was blocked with a shutter. The quantum dot's polarisation eigenbasis was identified with a linear polariser and used to calibrate the logical teleportation states H and V. Similarly, the superposition states D and A were set at ±45° to the rectilinear basis.

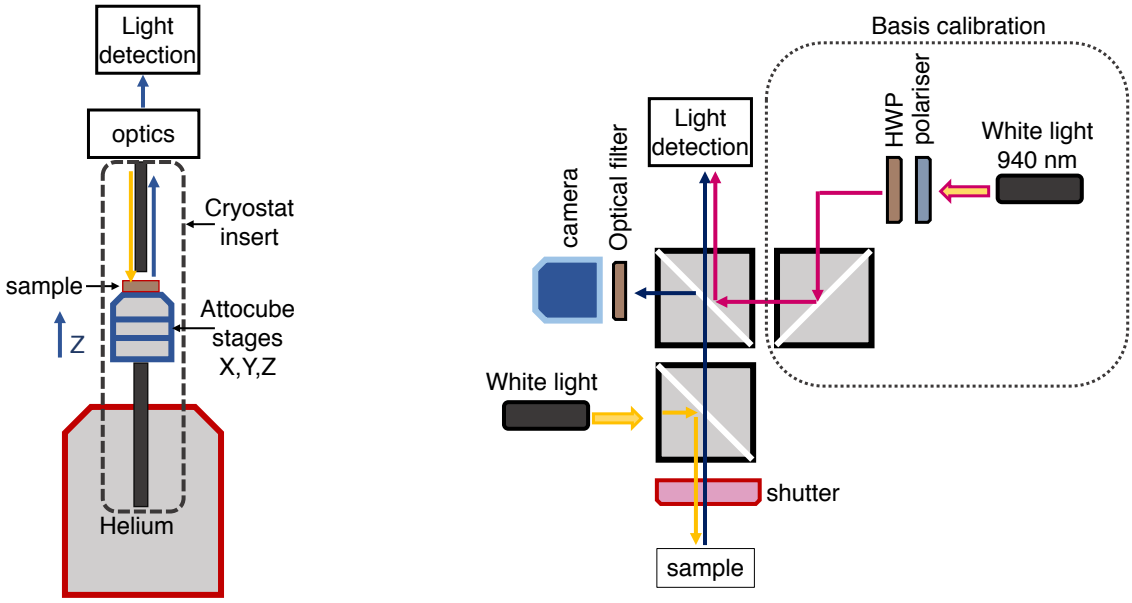

Figure 4.6: Schematic of the optics arrangement on top of the cryostat during the quantum relay experiment. A combination of beamsplitters splits the QD emission into two paths in order to image the sample and also send the majority of collected photons to the detectors. A polarised LED beam is used to calibrate the 4 input states H, V, D & A. Beamsplitter ratio: 92:8.

The E-LED device was driven electrically at a frequency of 203 MHz in forward bias. The modulating signal was an A.C. voltage rectangular waveform with pulses of 490 ps in width and 0.4 V in amplitude. The sample was cooled to a temperature of 19.7 K, at which photon rates were sufficient. Under these conditions, the biexciton B and exciton X emission occurs at 885.7 and 887.3 nm respectively and the fine-structure splitting was 4.2±0.1 μeV.

Finally, photons at the BSM and receiver polarising beamsplitters were detected using four superconducting single-photon detectors with mean detection efficiency 31±7%. The timing jitter between pairs of detectors was approximated as a Gaussian with full width at half maximum of 58.4±2.5ps, with single-photon-counting hardware resolution of 16 ps. The photon detection rate at the Receiver was ~620 kHz, corresponding to an efficiency of ~0.3% per pulse after all losses, including the >1 km fibres.

4.3.2 Three-photon coincidences

Three-photon coincidences were recorded corresponding to two photons at BSM detectors D1 and D2, with polarisation H and V, and one photon at either Receiver's detectors D3 and D4. SSPDs D3

and D4 record both expected photons with polarisation P and unexpected output photons with polarisation $\bar{P}$ simultaneously.

The detection times at each detector are defined as t1 (D1), t2 (D2) and t3 (D3 and D4). All events were recorded relative to detections at D1 (H-polarised photons). Third-order correlations $g^{(3)}$ for each output polarisation were determined from the normalised statistics of the three- photon coincidences, as a function of two time delays: $\tau_2=t_3-t_1$ and $\tau_3=t_3-t_2$ (see Figure 4.5 inset). It is important to clarify at this point that the choice of time axis, which corresponds to the chosen time delay of click events between two detectors, is arbitrary and serves for better visualisation purposes; for example, t_2-t_1 and t_3-t_1 have been used in previous reports.

The three-photon detection rate was ~0.47 Hz. However, the analysis of the $g^{(3)}$ correlations was based on the post-selection of coincidences within a window of 32 × 112 ps, for which the rate reduces to ~0.46 mHz. The error values quoted on the third-order correlations are derived mainly from Poissonian counting statistics based on the number of photons detected.

Figure 2c shows the measured third-order correlation function $g^{(3)}$ averaged over all four polarisation inputs, and over the corresponding co- and cross-polarised outputs. The horizontal and vertical axes are the time delays τ_2 and τ_3 between photon detection at D1 or D2, respectively, and a photon at D3 or D4. The intensity distribution has highly pulsed character, reflecting the electrical excitation mode, with peaks corresponding to the applied AC signal frequency (203 MHz=4.9 ns repetition period). Here, high intensity peaks are observed horizontally and vertically for $\tau_2=0$ and $\tau_3=0$, relating to the probability of the exciton emission immediately after a biexciton photon. Similarly, the low intensity diagonal line $\tau_2=\tau_3$, corresponding to coincident detection at D1 and D2, indicates a suppression in detecting two biexciton photons simultaneously due to the sub-Poissonian nature of the E-LED source.

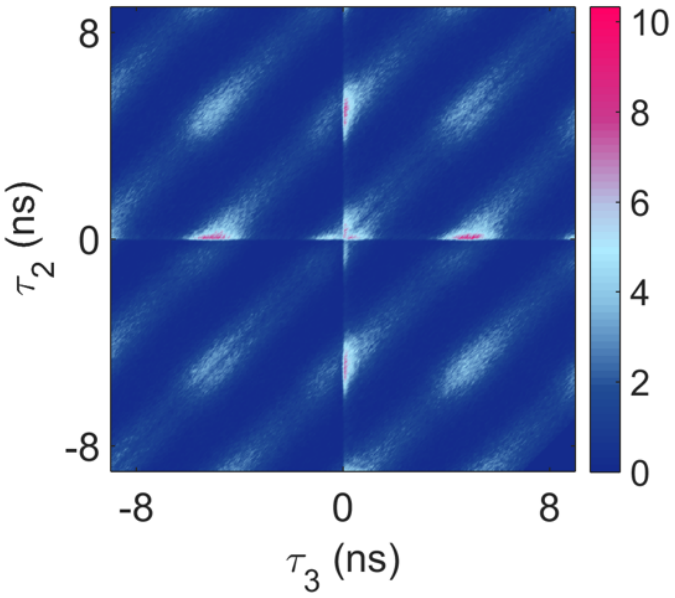

Figure 4.7: Average third-order correlation $g^{(3)}$. The pulsed character of the correlations is observed. The single-photon property of emission is seen as a dip in coincidences for τ_2=τ_3. The higher three-photon coincidences running along τ_2=0 and τ_3=0 originate from elevated probability of the E-LED emitting a pair of photons simultaneously.

4.4 Results

In principle, quantum teleportation should work for any unknown quantum state. In this implementation of a quantum relay, only the source's polarisation eigen-basis (rectilinear) and a superposition basis (diagonal) were used for the teleportation of quantum states. The success of the relay scheme is quantified by the number of correctly-polarised photons at the Receiver's detectors i.e. the photons that have been 'teleported' correctly. We therefore need to compare the number of photon coincidences at the two outputs of the PBS.

The teleportation fidelity for each input photon state a is defined as:

$$F_a(\tau_2,\tau_3) = \frac{g_P^{(3)}(\tau_2,\tau_3)}{g_P^{(3)}(\tau_2,\tau_3)+g_{\bar{P}}^{(3)}(\tau_2,\tau_3)} \quad (4\text{-}2)$$

where P and $\bar{P}$ are the expected and unexpected coincidences measured at the two orthogonal outputs of the PBS. The average relay fidelity is therefore derived from averaging over all four teleportation fidelities for the input photon states H, V, D and A. From (4-2), it can be deduced that higher contrast between expected and unexpected coincidences corresponds to higher fidelity. Error propagation is

included in this analysis to determine the relay fidelity errors of individual input states and the average relay fidelity. The average relay fidelity error calculation also includes systematic errors, due to the temporal calibration and resolution of the system, but are almost negligible.

Figure 4.8 and Figure 4.9 show the contrast between the measured third-order correlations $g_P^{(3)}(\tau_2, \tau_3)$ and $g_{\bar{P}}^{(3)}(\tau_2, \tau_3)$ at the beamsplitter outputs for each of the 4 input photon polarisation states, as a function of detection times τ_2 and τ_3. From the definition in (4-2), maximum teleportation fidelity occurs when the contrast is highest, that is along τ_2=0 and τ_3=0. The corresponding measured individual teleportation fidelities calculated by (4-2) are 0.957± 0.042 and 0.951±0.048 when teleporting the polar states H and V (Figure 4.8), and 0.845± 0.064, 0.847±0.063 for the superposition states D and A (Figure 4.9). The experimental results correspond relatively well to the theoretical estimation.

For the rectilinear basis (Figure 4.8), the high contrast areas expand over a broad window, as quantum teleportation takes place along the τ_2=0 (H input state) and τ_3=0 axis (V input state). These horizontal and vertical lines through time zero delay indicate the correlations between the exciton and biexciton photons when the detectors click simultaneously, indicating the successful teleportation of the input state. At all other detection times, the difference in counts averages 0, which corresponds to a teleportation fidelity of 0.5 i.e. random outcomes (light blue). A dark stripe along τ_2=0 (V input state) and τ_3=0 axis (H input state) reveals the sub-Poissonian character of the source and the suppressed probability of two XX photons being emitted simultaneously.

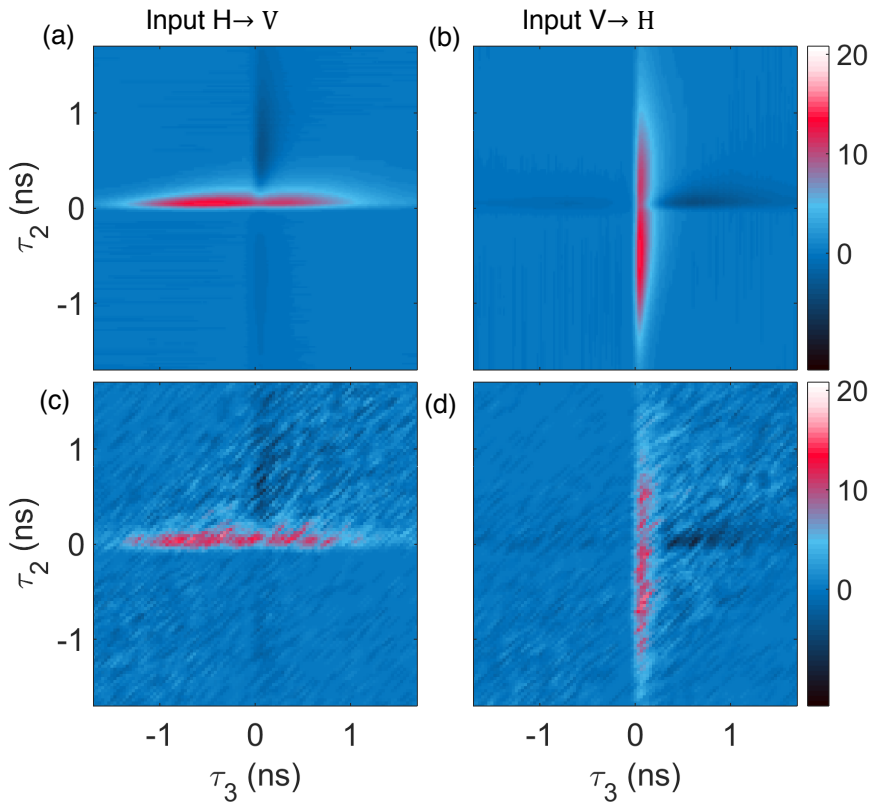

Figure 4.8: Difference between expected and unexpected outputs P and $\bar{P}$ for the polar states H & V, derived from the time-dependent 3-photon coincidences. (a, b) calculated and (c, d) experimental data. (a) The Sender encodes an H-polarised laser photon and the Receiver measures in V. (b) The Sender encodes a V-polarised laser photon and the Receiver measures in H.

Figure 4.9 shows the contrast calculated from the difference between the measured third-order correlation functions $g^{(3)}_{HVD}(\tau_2\tau_2)$ and $g^{(3)}_{HVA}(\tau_2\tau_2)$, for the cases where diagonal basis states D and A are encoded on laser photons and the Receiver measures D and A respectively. Interestingly, the high-contrast area for the superposition states is contained within a small time-window around τ_2=0 and τ_3=0, as the state teleportation is limited by the coherence time of the single biexciton photon and the entangled state. In contrast to the results presented above, these superposition states are not aligned to the BSM basis and their successful teleportation depends on the quantum properties of the source. The coherence time of the biexciton photon, detected at the BSM, limits the window along τ_3 and τ_2. The calculations agree well with the experimental results.

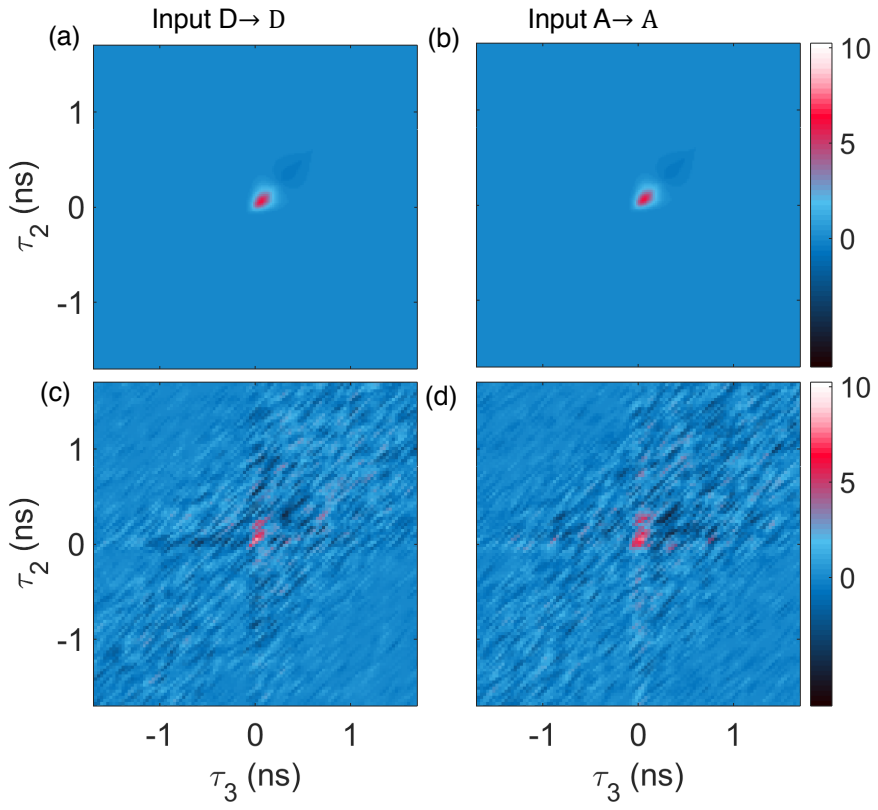

Figure 4.9: Difference between expected and unexpected outputs P and $\bar{P}$ for the superposition states D & A, derived from the time-dependent 3-photon coincidences. (a, b) calculated and (c, d) experimental data. (a) The Sender encodes a D-polarised laser photon and the Receiver measures in D. (b) The Sender encodes an A-polarised laser photon and the Receiver measures in A.

4.5 Discussion

The third-order correlation functions were used to examine the entanglement properties of the source. Figure 4.10 (a) shows a Bell parameter, extracted from the correlations. It clearly surpasses the classical limit of 2 reaching a peak of 2.59 (0.01) or 91.8% of the ideal value. Figure 4.10 (b), plots the average Relay fidelity, as a function of τ_2 or τ_3 for simultaneous detection of two photons at the 'BSM' section. The high average fidelity derived from the teleportation of 4 states clearly exceeds 0.75, which is the classical threshold, proving that quantum teleportation has taken place. The 0.8 limit [113] for the four-state protocol employed here is also exceeded. The peak rises to a maximum value of 0.900±0.028, exceeding the six-state average fidelity reported previously for teleportation using a QD [91].

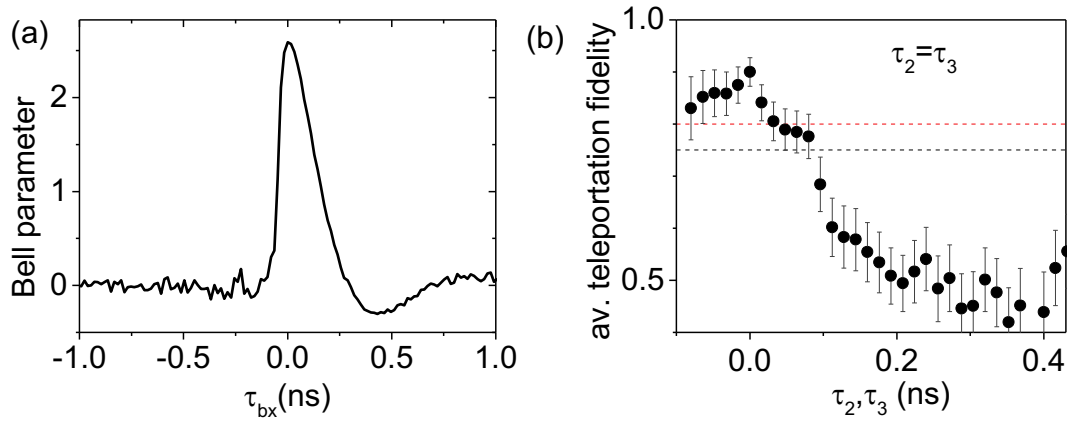

Figure 4.10: (a) Bell parameter extracted from experimental data. (b) Average relay fidelity as a function of time delay τ_2 and τ_3 for $\tau_2=\tau_3$. High fidelity points are concentrated around τ_2, $\tau_3=0$, where the measured fidelity exceeds the classical limit of 0.75 shown by black dashed line. The threshold for four-state error correction of 0.8 is shown as dashed red line.

Given the fact that the implementation described here uses the single-photon, efficient BB84 protocol in the asymptotic scenario [113], [115] and in the limit of infinitely many signals shared by the users, the secure key fraction R that can be extracted from each detected photon is [95], [112]:

$$R = 1 - h(Q_Z) - h(Q_X), \quad (4\text{-}3)$$

where *h* is the entropy function. Also taken into account are the quantum bit error rates Q_Z and Q_X in the Z and X basis, corresponding to the measurements in the {H,V} and {D,A} bases respectively. By substituting the results:

$$Q_Z = \frac{(1 - 0.951) + (1 - 0.957)}{2} = 4.6\%$$

$$Q_X = \frac{(1 - 0.845) + (1 - 0.847)}{2} = 15.4\%$$

From the above, a secure key fraction R=0.11 secure bits/detected photon corresponding to fidelity=0.90 can be extracted. The analysis here assumed the ideal scenario of infinite key size, this implementation of a quantum relay is, in principle, good enough to produce secure keys.

4.5.1 Effect of post-selection on fidelity

The effect of data binning on average teleportation fidelity and on individual polarisation bases is shown in Figure 4.11. By increasing the post-selected time bins, the extracted key can be extended at

the expense of lower teleportation fidelity and error correction protocol. High fidelity is observed in the rectilinear basis, even for large binning windows, as no two-interference window is needed for achieving teleportation. The fidelity drops for the diagonal basis once the binning window size exceeds the coherence time of emission.

The measured teleportation fidelity was derived from post-selected three-photon coincidences within a 32x112 ps window. Quantum teleportation, which refers to the teleportation of superposition states, is conditioned on two-photon interference between the input state and the ancilla photons. This is illustrated by Figure 4.11, where the blue trace represents the fidelity of the Diagonal basis states as a function of key length (binning window size). The fidelity points above the threshold of 0.75 for quantum teleportation are limited to a time window equivalent to the coherence time of the biexciton photon. In comparison, the fidelity for the teleportation of classical states in the rectilinear basis remains high, since it is not dependent on the two-photon interference effect.

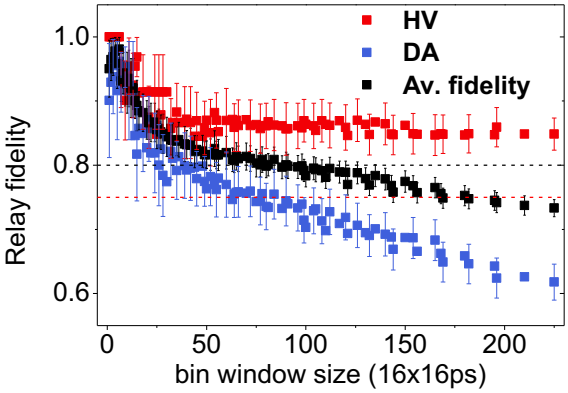

Figure 4.11: Effect of the binning window size and effectively key length on the teleportation fidelity. The red and blue traces represent the averaged fidelity for the polar states and superposition states, respectively. Increasing the area of post-selected number of coincidences increases the extracted key length, but reduces the fidelity of teleportation. (1 pixel=16 ps [τ_1] × 16 ps [τ_2]).

4.6 Conclusion

In summary, this chapter has demonstrated the proof of principle experimental implementation of a teleportation-based quantum relay. It was the result of building on the previous work by colleagues that has demonstrated teleportation using quantum dots from an E-LED [86], [91]. In this experiment, the device has been used as a triggered source of entangled photon pairs at MHz frequency and distribution of entanglement from a quantum dot over a significant distance was reported for the first time. The results presented here show the potential of the device as a source for generating error-corrected

quantum keys using the BB84 protocol. The next steps include shifting the emission to telecom wavelengths [116], allowing for integration within a quantum network, but also device design improvements that can enhance the performance of the source in terms of efficiency and practicality. The latter will be explored in the next chapter.

Chapter 5 Development of an E-LED based on Droplet Epitaxy QDs

5.1 Introduction

In electrically-injected devices like the E-LED, the carriers are constantly supplied both from and to the wetting layer and to the dots when the diode is biased above the turn-on voltage in forward bias. It has been suggested that the presence of the wetting layer around the dots can affect their optical and electrical properties [117]. One of the issues which surfaces is the re-filling of the dot with free carriers from the wetting layer, even when the diode is not ON. The result is uncorrelated mixed emission, which occurs when the emission of an XX photon is not followed by an X photon. A perfect photon pair source would emit photons that have decayed from the XX state to ground through the X state. In real devices, however, the dot may be re-excited to the XX state after recapturing an electron-hole pair, emit a charged X* after non-geminate capture of an electron or hole or emit a second X photon from the ground state without excitation through the XX state. The effects of dot re-excitation were made obvious when operating under AC bias conditions, when photons can be detected even during the OFF time of the pulse, as illustrated from the entanglement measurements in 4.1.2.

5.1.1 Coherence time & post-selective correlations

The second issue that needs addressing is the limited effective coherence time of the emission. In Chapter 3 it was shown how the post-selected two-photon interference visibility is limited by the coherence time of the emission and the detector resolution. In Chapter 4, it was shown how the quantum relay fidelity was also limited by the biexciton coherence length, since quantum teleportation is conditional upon successful two-photon interference. As a result, the post-selection window used for the analysis of the correlations was comparable to the biexciton coherence length. It is thus straightforward that dephasing processes degrading the coherence of the emission also limit the post-selection timescales.

In attempt to tackle the above issues, we may turn our interest to the fundamental limits of the E-LED device, which are interlinked with its design structure and QD growth. For our conventional E-LED structures self-assembled QD growth has been employed, which gives great control over the process and subsequent optical properties of the dots. However, the S-K growth method is based on strain between the GaAs substrates and the formation of a lattice-mismatched wetting layer. It has been suggested that the absence of this 2D layer may provide a remedy to the re-excitation problem [118]. An alternative method of growth based on droplet epitaxy (DE) to eliminate the WL was thus investigated.

The D-E growth method has already been shown to produce entangled photon emission [51], [119] with good entanglement fidelity results. The aforementioned work, however, demonstrates growth on (111) surfaces. The motivation behind growing on (111) surfaces is the minimisation of fine-structure splitting due to the atomic symmetry of the crystal. Similarly, growth along the (100) axis may induce dot elongation due to crystal asymmetry [120]. On the other hand, the InAs/GaAs (001) system is compatible with established III-V material technologies [121]. The devices used for this thesis were grown on (001) substrate surfaces to enable high quality cavity growth in the form of vertically stacked mirrors requiring accurate control of the growth rate during the MBE process.

A major difference between the two growth methods is that D-E does not rely on strain and can thus allow both lattice-matched and lattice-mismatched material systems to be used, opening the possibility for greater flexibility in the wavelength tuning of the dots. Telecom-band emission by D-E has already been demonstrated by successful growth on InP (111) substrates [122], [123]. Since single photon emission at longer emission wavelengths would be the natural progression of this project, it is an important advantage compared to the traditional S-K growth. This chapter describes the development of an E-LED based on InAs/GaAs QDs emitting around 900 nm using the D-E growth method.

5.2 Droplet Epitaxy growth

In contrast to the extensively investigated conventional S-K growth, the mechanisms governing D-E growth method are not yet well understood. Controlling variables like the density, wavelength and shape of dots is not governed by the same growth parameters as in the S-K growth. The studies here describe the attempts on growing useful D-E QDs at short wavelengths around 900 nm.

Droplet Epitaxy as a mode for growing unstrained QDs has been proposed by Koguchi et al in 1991 [124]. The growth technique is based on MBE and is illustrated in Figure 5.1. The first step is to create

a GaAs buffer and terminate it with Gallium. At this point no arsenic is supplied to avoid intermixing with Indium droplets later on. The next step is to deposit Indium on the GaAs substrate at low temperature (~280°C). Indium is a liquid at this temperature and so droplets form, as shown in (a). The surface tension between the two materials is responsible for the formation of isolated 3D In islands, which will form InAs QDs without a WL [125]. To create QDs, these droplets need to crystallise by being exposed to Arsenic flux as in (b). The last step is to anneal the droplets at a higher temperature (<500 °C) to improve the optical quality of the dots, as defects may have formed during the previous step. The temperature at the time of indium deposition is what determines the density of dots, in line with the predictions by classical nucleation theory. Basically, the density decreases with higher temperature, as adatoms preferentially attach to existing clusters instead of creating new ones [126]. The dots are then capped with GaAs and cooled down.

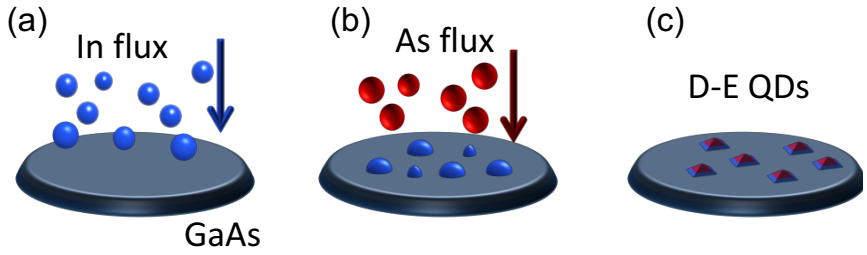

Figure 5.1: Illustration of Droplet Epitaxy QD growth technique. The group III (In) and V (As) elements are supplied individually. (a) Indium is deposited at low temperature (<300°C) and forms droplets on the Ga-terminated surface. (b) The droplets are exposed to As and (c) become crystallised semiconductor islands.

5.3 DE QD morphology

How the new growth method affects the shape and size of the D-E QDs is a critical and very practical question for us. For anyone studying phenomena of quantum confinement, it is well-known that structural characteristics of the dots may change the single-particle electronic states and hence the optical properties of the emission [127], [128]. The confinement potential of the carriers in the dots depends on various parameters such as crystal symmetry, composition and shape, amongst others, and the resulting FSS is a combination of these mechanisms.

We may draw our attention to growth parameters like the growth temperature and indium deposition, which can dramatically affect the shape, size and density of the dots. The surface morphology of

indium droplets and crystallised QDs is investigated using Scanning Electron Microscopy (SEM) and the relevant information is extracted from the scans by image analysis.

Figure 5.2 (a) and (b) show uncrystallised indium droplets deposited with 2 ML of indium, while (c) shows the crystallised QDs. The uncrystallised indium droplets are found to be round and symmetric with a mean diameter of 90.78±16.3 nm. The density of droplets on these samples is found to be around 2.9 μm^{-2} with no significant variation across the centre, middle and edge areas of the wafer. Crystallising the droplets creates faceted nanostructures which do not exhibit particular elongation as in (c), which is encouraging when we consider the fine structure splitting requirements for our experiments.

The first observation we make is the increased amount of 3D islands found on (c) compared to (a). Two sizes of structures can be identified with small and large islands being formed, whereas the uncrystallised dots in (a) are fairly similar in size and shape. The second observation is that the density of large islands in (c) corresponds well to the density of uncrystallised droplets in (a) and (b). It is not completely clear how the smaller islands present on the surface in (c) are formed.

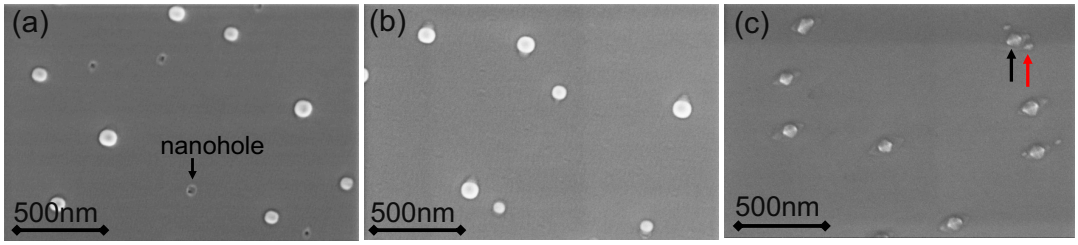

Figure 5.2: Scanning electron micrographs of indium droplets deposited on GaAs (001) (2ML of indium at 290°C). Uncrystallised Indium droplets deposited after growth interruption of (a) 30s (b) 30 minutes. The effect of arsenic flux present in the chamber, indicated by the etching of nanoholes, is more prominent when the indium deposition takes place immediately after the As cell is closed. (c) Crystallised indium droplets. Black arrow: big island, red arrow: small island. (SEM images were provided by Joanna Szymanska).

The second observation from Figure 5.2 (a) is the effect of local etching and the creation of nanoholes on the surface. The formation of nanoholes by etching during D-E growth is a well-known phenomenon [119], [129]. The etching happens during the deposition of Gallium for surface termination, before the deposition of Indium. As reported by others [130], the etching process begins when Ga atoms are exposed to As at high temperature (>480 °C) and results in the creation of nanoholes surrounded

by ring-like structures. At this stage during growth the As cell is closed but As molecules are still present. Growth may be interrupted before Ga deposition begins, so that the background pressure is low and As molecules are removed by pumping the chamber out.

Figure 5.2 shows uncrystallised In droplets after an interruption of (a) 30 s and (b) 30 mins after the As cell is closed. Fewer nanoholes are present in (b) and have been filled by the Indium droplets, verifying that the presence of As plays a critical role in the formation of nanoholes. The crystallised dots in (c) also sit on a "pedestal", which appears to be the evolution of the nanohole and ring. In summary, two distinct processes may be identified: 1) local etching by Ga atoms, but also 2) Ga consumption by GaAs growth that gives rise to the creation of nanorings around the holes [131]. The more detailed mechanisms behind these effects are not completely clear and are the subject of ongoing investigation. The conclusion from these observations is that nanoholes appear to act as preferential sites for InAs QD nucleation, opening up the possibility of QD positioning and ordering using the D-E method [132], [133].

5.3.1 Growth Temperature

As already mentioned above, compared to conventional growth techniques, the fabrication of dots by D-E takes place at low substrate temperatures (≤290°C). Figure 5.3 shows SEM scans from samples that have been grown at different temperatures, ranging from 70 °C to 290 °C. Graph (a) illustrates the effect of increasing the growth temperature during the indium deposition on the density of droplets. The density of droplets is highest for the sample grown at the lowest temperature (145.5 μm^{-2} at 70 °C) and reduces steeply with rising growth temperature (2.9 μm^{-2} at 290 °C). The density of droplets can be well described by an Arrhenius plot of the form [134]:

$$A * \exp\left(\frac{E_a}{k_B(T+273)}\right), \qquad (5\text{-}1)$$

where A is the pre-exponential factor, E_a is the activation energy, k_B is the Boltzmann constant and T is the growth temperature in degrees °C. An activation energy of E_a=0.238 eV and a pre-factor A=0.0138 μm^{-2} can be determined from the fitted curve.

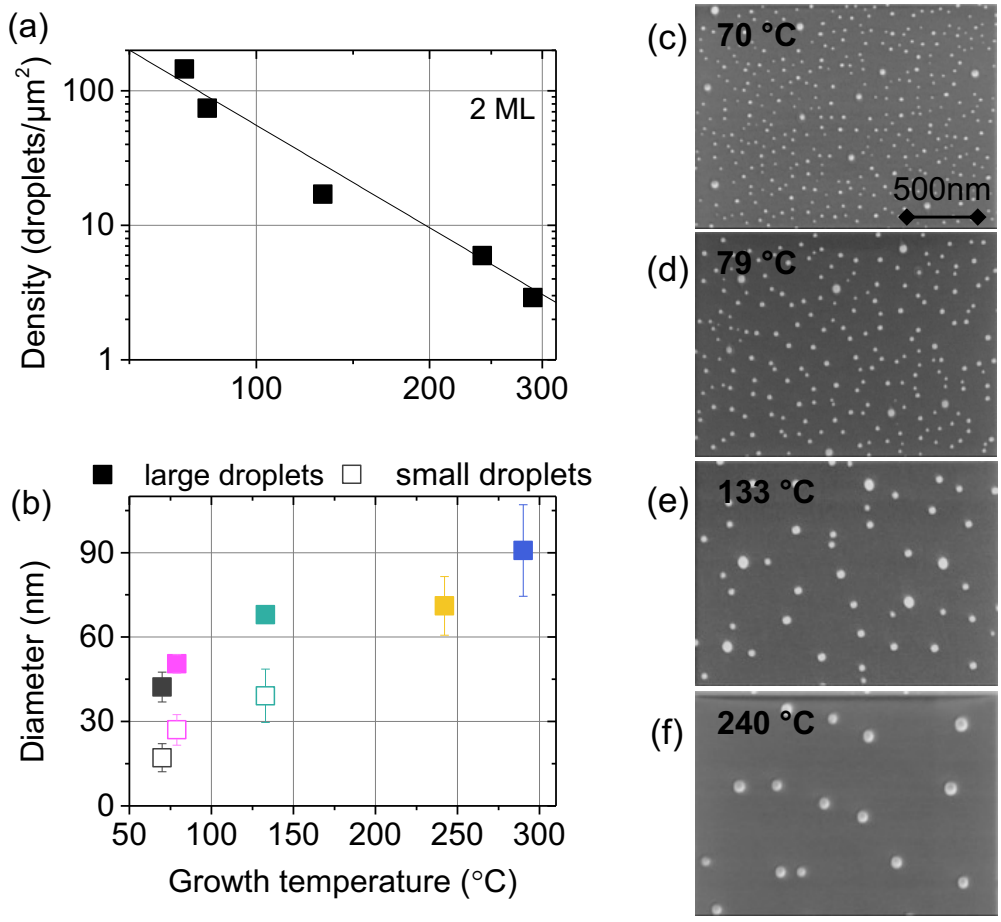

Figure 5.3: Effect of growth temperature on the uncrystallised indium droplets. All depositions are at 2 ML of indium content. (a) Arrhenius plot of droplet density as a function of growth temperature. The droplet density reduces dramatically with increasing growth temperature. (b) Droplet diameter as a function of growth temperature. The droplet size increases with increasing temperature and becomes more uniform. (c)-(f) SEM scans of the uncrystallised indium droplets at different growth temperatures. (SEM images were provided by Joanna Szymanska).

It was thus shown from our study that the growth temperature is a significant variable in tuning the droplet density and agrees with an Arrhenius-type temperature trend. An increase in droplet diameter by a factor of 5 is also observed as a result of increasing the temperature over the whole range (Figure 5.3 (b)). Another interesting observation in terms of droplet morphology is the bimodality observed for the lower temperatures of the range 70-133 °C (images c-e). Droplets grown at the lower temperatures vary in size with a large-to-small diameter ratio of around 2 (Figure 5.3 (b)). For the sample grown at 70 °C small droplets amount for around 97.5 % of all the droplets present on the surface, whereas for the sample grown at 290 °C no small droplets can be observed. The trends discussed here

and more specifically the observation of a bimodal distribution of large and small droplets are in accordance with the assumption that with higher temperature and higher surface activity, the adatoms prefer to attach to existing clusters instead of creating new ones, in a process referred to as Ostwald ripening [126]. This phenomenon is well-documented and is responsible for the droplets growing in size at the expense of smaller ones and their density decreasing [33].

5.3.2 Indium content

The indium content used during growth was another main investigation parameter. In order to quantify the amount, the stated values refer to the indium flux equivalent to form one monolayer (ML) InAs. From the SEM images in Figure 5.4, it can be observed that the higher indium content (2 ML) creates two sizes of islands after crystallisation; large and small ones, whereas for 1.6 ML indium mostly uniformly-sized QDs are obtained. Note that the classification into large and small is based on the island area, from which a clear step increase was identified and a threshold was set. Large islands appear pyramidal in shape and slightly elongated, as is typically observed from strain relaxation mechanisms [135], [136]. Interestingly, the large islands show elongation along a certain axis, suggesting ordering in their formation. Most of the small islands, however, are circular or elliptical in shape.

The spectrum in Figure 5.4 d) shows the PL measurement obtained from (c). There is emission from QDs extending from 850 nm to 980 nm. It is important to note the absence of any wetting layer-like features around 870 nm, which was our initial target. At this point, it was not possible to say with certainty whether the emission comes from the large or the small islands, or both.

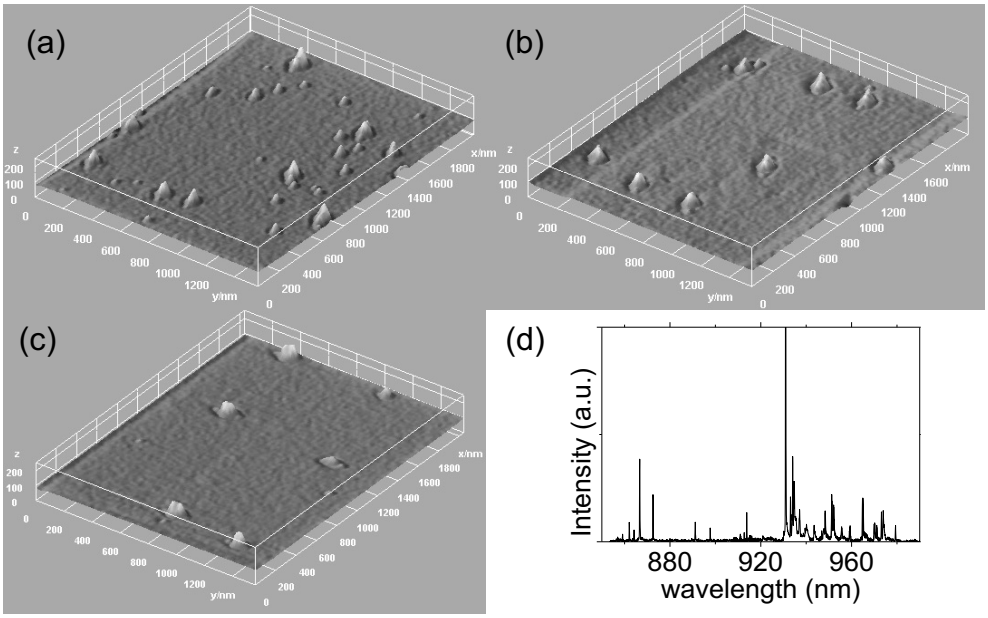

Figure 5.4: Projected 3D-Surface plots from 2D-SEM scans (the z axis has arbitrary units) showing crystallised indium droplets deposited at 240 °C for different indium content: (a) 2 ML (b) 1.8 ML (c) 1.6 ML (d) PL spectrum of (c).

Data from SEM image analysis are displayed in Figure 5.5. The density of big islands remains fairly constant at around 2.33±0.29 μm^{-2}, whereas the density of small islands increases with increasing indium content. A slight enlargement for both large and small islands is also noted and indicates ripening.

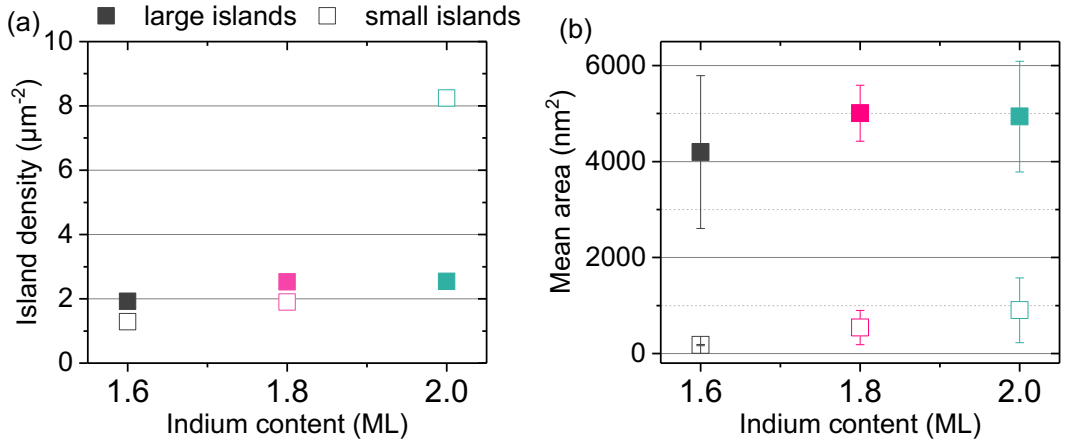

Figure 5.5: (a) Dot size and (b) dot density as a function of indium content. Island sizes are categorised into large (solid squares) and small (open squares).

5.4 DE QDs in an optical cavity

Once the right growth conditions were identified, a device with QDs embedded in an optical cavity was grown. We chose 900 nm as the centre wavelength for the D-E QDs devices grown for this thesis. The optical sample was made of 12 pair bottom DBR mirrors, each consisting of 65 nm of GaAs and 77 nm of AlAs followed by 2-lambda GaAs cavity with dots in the middle. Two repeats of mirror were added on top of the cavity. Photoluminescence measurements can reveal important information about the excitonic complexes in these dots and the injection regimes that govern the emission.

5.5 Polarisation-resolved spectroscopy

Naturally, it is of utmost interest to assess how the fine structure splitting of D-E QDs compares to our existing S-K QDs and how useful they can be for our applications.

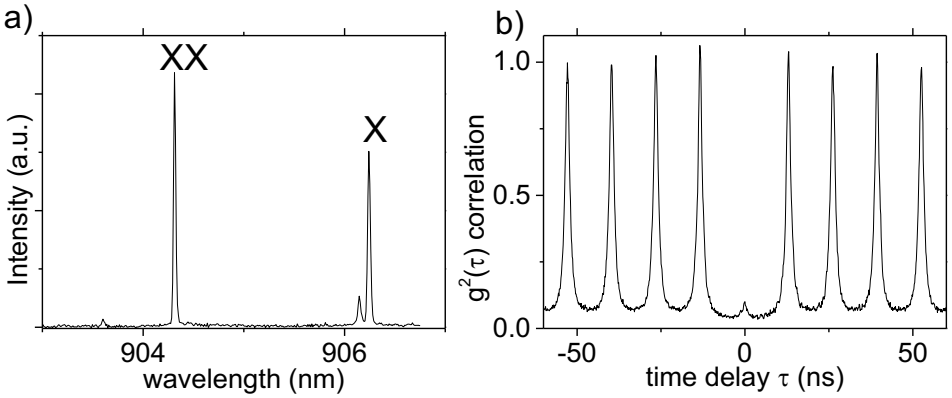

Figure 5.6: PL spectrum of a D-E QD placed in a 2λ-cavity structure with 12/2 DBRs. b) Second-order correlation measurement of the XX emission under above-band pulsed excitation at 57.5 μW.

Figure 5.6 (a) shows the spectrum of a D-E QD from an optical cavity sample, under PL excitation. Figure 5.6 (b) shows the normalised second-order correlation for the biexciton emission of the dot. The $g^{(2)}$ around $\tau = 0$ peaks at a value of 0.101 ± 0.01, showing suppressed multi-photon probability, stray emission from other dots and weak re-excitation features. The offset in the pulsed $g^{(2)}$ comes from background components such as emission from the sample itself [137].

5.5.1 Statistics on FSS measurements

A sample of 53 quantum dots was measured using the half-wave plate setup described in Chapter 2. A study of the dipole orientation of the emission and the size of the FSS are included in the analysis. A large variation in FSS magnitude is observed, with the mean FSS being equal to 44.6 μeV with standard deviation of 29.55 μeV.

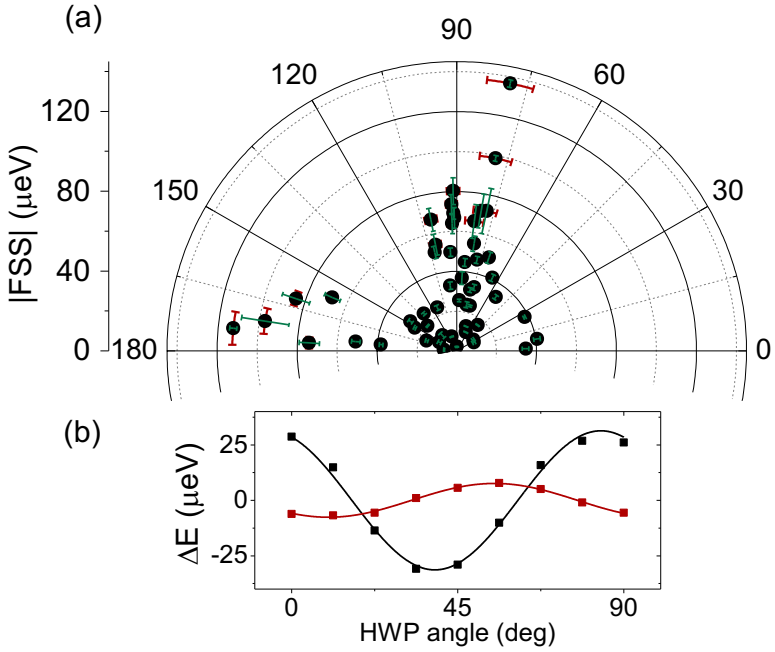

Figure 5.7: (a) FSS and dipole orientation angle from linear polarisation axis rotation. The reference crystallographic axis angle is arbitrary. The points are distributed over all regions of the semi-circle. (b) FSS measurement by HWP rotation for two different D-E QDs. Different phases show variation in the dipole orientation angle.

Figure 5.7 (a) plots the magnitude of FSS for each QD as a function of the in-plane angle of the lowest energy eigenstate, where dipole orientations of 0 and 180 degrees are equivalent. The first observation is that dots were found and measured across all circular sectors. The second observation is that for the dots with fine structure splitting below 40 μeV the plot shows the absence of preferential direction in the [001] plane. The measurements are further analysed in the histograms of Figure 5.8.

DE-QDs with small FSS have been recorded and, assuming a Gaussian distribution as in Figure 5.8 (b), there is a finite probability (0.0347) of finding a dot with small |FSS| (<4 μeV). The distribution of the FSS magnitude has a centre at 28.96 μeV, closer to 0 than the statistical mean (44.6 μeV). Note here that the angle of the crystallographic axis was not identified during measurements, but it was

extracted from the angle distribution histograms based on the assumption that QDs will tend to align along the crystallographic axes. From Figure 5.8 (b), the [110] and [1-10] planes can be found at approximately 80° and 170°.

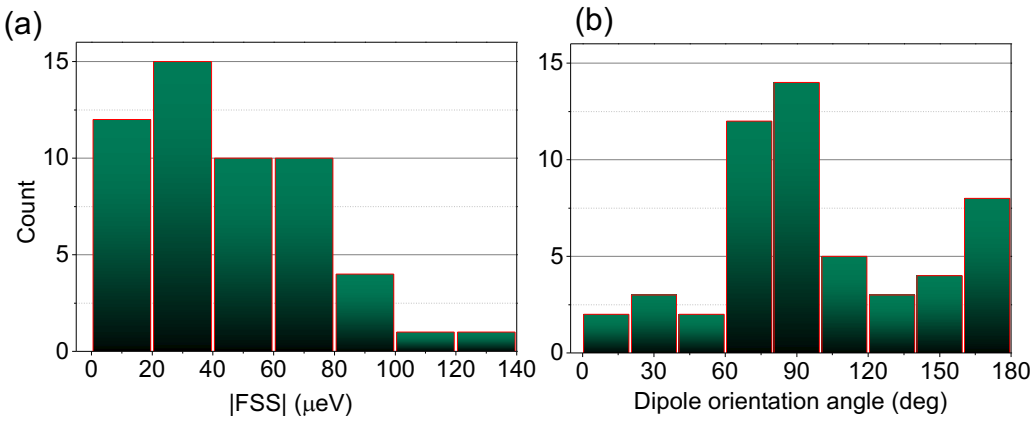

Figure 5.8: Histogram for all the dots according to (a) FSS magnitude. (b) dipole orientation angle. The dipole angle histogram has two distinct peaks at around 90° apart, attributed to the [110] and [1-10] crystallographic axes.

In summary, this section has shown that InAs QDs with low fine-structure splitting can be grown by droplet epitaxy. This has not been demonstrated before on GaAs [001], nor their incorporation into an optical cavity. The optical spectra show no evidence of wetting layer, which was the goal of this project.

5.6 DE QDs in a doped cavity

After D-E QD optimisation through AFM, SEM and PL measurement characterisation, we proceeded to the next step, which is incorporating the QDs in an LED structure. The standard E-LED design was adopted, where the p-i-n structure is designed to inject electrons and holes into the QD through non-resonant flow of current. However, the first few attempts at growing a D-E QD-based LED exposed a range of issues with these devices.

5.6.1 Hole injection problem

The first attempt at a D-E QD-based LED was QDs grown with 2 ML of Indium. The first issue that was the limited EL intensity (see Figure 5.11(a)) and the absence of narrow emission lines in the spectrum. In fact, the spectrum included features with a broad linewidth but no emission from a biexciton cascade, as illustrated by the EL trace in Figure 5.9 . The second issue was the early turn-on voltage of

the diode, which was ~1.3 V. The carriers are expected to be created in the GaAs region, which has a bandgap corresponding to 1.5 V at 4 K. Therefore, there was a flow of carriers through the device but no radiative recombination of electron-hole pairs was observed from the QDs, which suggests that current was probably non-uniform across the junction. The issues are also obvious when comparing the microscope image of the device EL to the camera image of a previous S-K E-LED (Figure 5.11(a) and (e)).

A third issue was the blinking of the emission over timescales of hundreds of milliseconds, which sometimes indicates coupling of the radiative transitions to non-fluorescing states. One possible cause for fluorescence intermittency is the presence of crystal defects or dislocations that can act as charge trap centres reducing the emission from the QD states [138].

The situation was investigated further by reducing the voltage bias below turn-on, where no electroluminescence occurs, since the electric field across the intrinsic region is increased. In this regime, QD spectra could be obtained with non-resonant, above-band optical excitation, as illustrated by the PL trace in Figure 5.9. This result shows that the quality of the QDs is not inherently problematic, but there is a fundamental issue with the electrical injection mechanism. Moreover, broadening of the dot emission at turn-on voltage is an indication that injection of either the electrons or the holes is occurring across the whole area of the device.

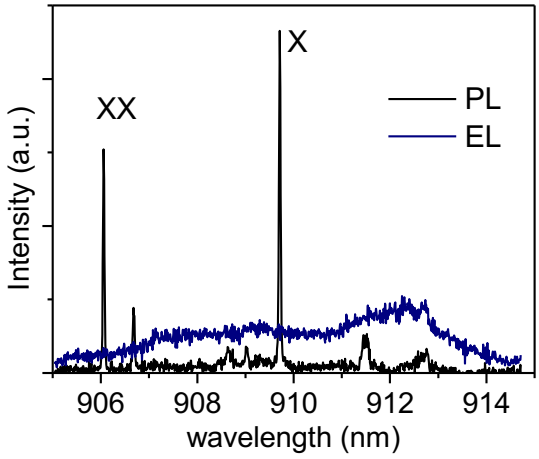

Figure 5.9: Spectra obtained from the first D-E LED. The spectrum under electrical injection consists of broad linewidth features resembling the cavity bandwidth and no QD emission can be observed. The spectrum obtained under optical excitation reveals exciton emission.

The above observations indicate non-uniform injection of carriers into the QDs, as illustrated by Figure 5.10 (b). The assumption here is that only the dots near a defect nucleation site receive both electron

and hole carriers, and dot EL from other regions of the mesa is quenched because hole injection is localised away. Following from the discussion in section 5.3.2 (Indium content) and Figure 5.4, we may suggest that large island formation is associated with the stage of In droplet deposition and the presence of nanoholes that act as nucleation centres [135], [136], [139]. It is possible that over a critical indium amount, the formation of the large strained islands introduces defects into the structure [33]. Island relaxation in lattice-mismatched systems has been found to reduce carrier concentration near the QDs and to quench luminescence intensity [140], both of which have been clearly observed here.

In order to improve the current injection, an annealing step (600 °C) was added to the growth process after the initial burial of the droplets, so that any excess indium from the surface is flushed away. The effects of this step are encouraging and are shown by the turn-on voltage measurement in Figure 5.10 (a) and the improved EL observed in Figure 5.11 (b) compared to (a).

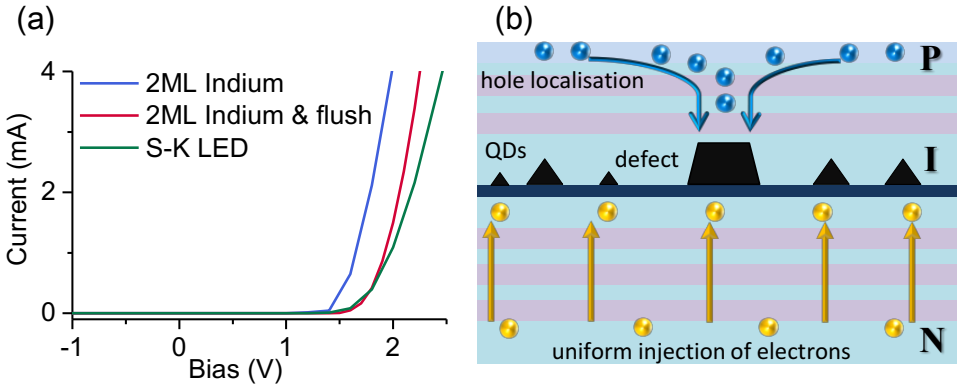

Figure 5.10: (a) Current-Voltage curves for two D-E LEDs compared to an S-K LED (20 K). The early turn-on voltage observed for the first D-E LED has been rectified by an indium flush step added during growth. (b) Illustration of the hole-injection issue of the D-E LED devices. Defects originating from large indium islands may propagate upwards in the structure and cause localisation of hole injection away from the QDs and EL suppression.

Figure 5.11 shows the progression of our study on the role of indium content in the development of an E-LED based on D-E QDs. From these images, there is an obvious trend linking the indium content to the amount of EL detected from the mesas. In (a) the mesa is mostly dark with a few localised bright spots and EL concentrated near the contact. The effect of reducing the indium content is more uniform EL across the mesas. The device with the lowest indium content (d) finally exhibits considerable EL due to QD emission.

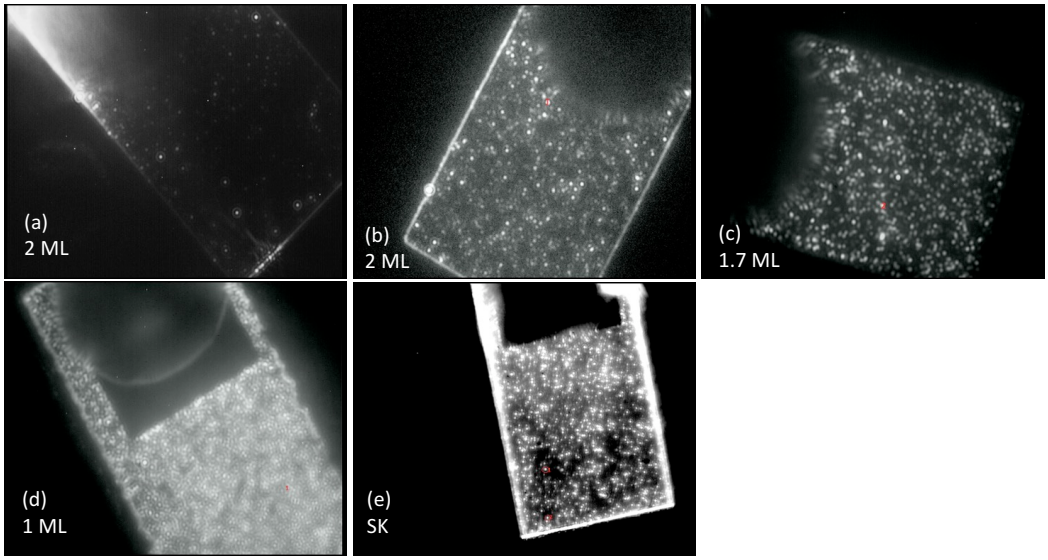

Figure 5.11: Photographs taken from the cryostat imaging setup for various devices under EL conditions at 20 K. (a) no Indium flush step. (b)-(d) D-E QD LED devices for different indium content. (e) S-K QD device. Reduction of the indium content from 2ML to 1ML improves EL. Mesa size: 220μm x 110μm.

5.7 Droplet Epitaxy Entangled-LED

In this section, the properties of the photons from an E-LED based on D-E QDs, are investigated. The device used for these measurements is a doped cavity structure with droplet epitaxy dots grown at 1.7 ML of indium (Figure 5.11(d)). The quantum dot being characterised has emission from a bound X-XX pair and the spectrum of the emission is shown in Figure 5.12 (a).

A second-order correlation $g^{(2)}$ of the exciton photon is shown in Figure 5.12(b). The fast detector response and the low background emission allows us to resolve a zero-delay dip very close to zero (0.08617±0.0041), verifying single-photon emission under DC electrical excitation conditions. A numerical fit to the correlation data can be obtained using $g^{(2)}(t) = 1 - exp\,(-\frac{|t|}{\tau_0})$ for perfect detectors. The exciton lifetime $\tau_0 = 1.46\ ns$ is extracted from the fit.

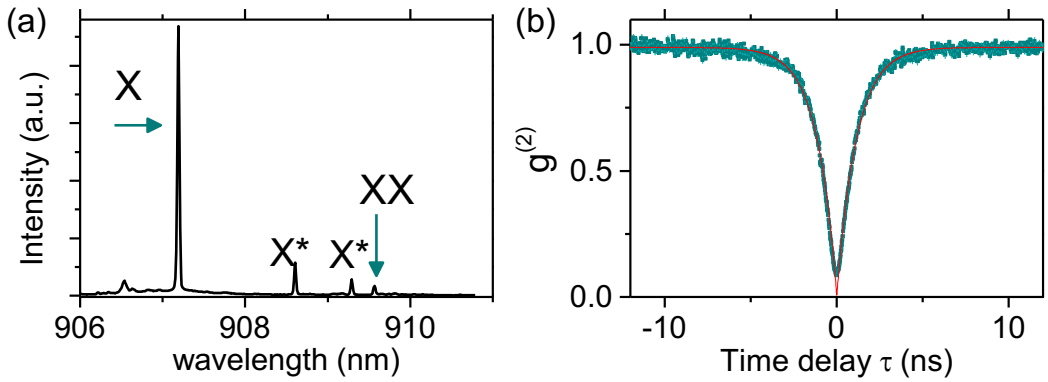

Figure 5.12: (a) Spectrum of the D-E QD used for the measurements in this section. (b) $g^{(2)}$ measurement of the X photon under DC bias. Current density: 5.28 nA μm^{-2}, T=21 K. $g^{(2)}(\tau=0)$= 0.0862 (0.0041).

5.7.1 Pulsed Operation

It has already been shown that triggered emission and detection of the photon events is required for any practical implementations of quantum logic operations. Figure 5.13 shows a basic investigation of the emission characteristics in pulsed mode. The dot was electrically injected using an AC voltage at a frequency of 203 MHz and a nominal pulse width of 300 ps. Note that these excitation conditions are similar to what was quoted in Chapter 4 for S-K QD excitation. However, direct comparison between the two cases is not possible, as the injection dynamics are different between the two systems. Consecutive distinct pulses are observed in the $g^{(2)}$ trace in (a), while reduced emission is observed for the zero-delay peak. The $g^{(2)}$ in pulsed mode allows us to study the issue of dot re-excitation more closely. The creation of carriers in D-E QDs occurs at the GaAs layer and not in the wetting layer, as before. Some re-excitation around time $\tau=0$ is still present, even in the absence of a wetting layer directly below the dots. The $g^{(2)}$ in (a) is slightly better than the one obtained with an S-K QD Figure 2.11 (b) , however, the two cannot be compared directly, as the electrical injection conditions are different in each case. This suggests that the re-capture of carriers is also a consequence of the creation of carriers around the QD, dependent on the injection conditions.

Polarised second-order correlations in the circular basis are shown in (b), illustrating the high degree of correlation in this basis for this particular X-XX pair. The correlation traces have a pulsed character with the peak separation of 3.3 ns corresponding to the pulse repetition rate of 303 MHz. These results suggest that D-E QDs embedded in an E-LED have the potential to serve as high-quality sources for triggered pulsed operation.

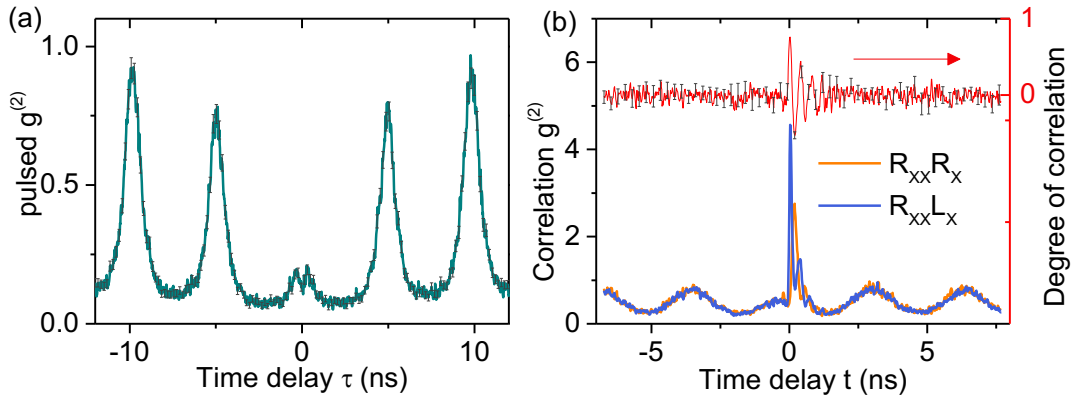

Figure 5.13: (a) $g^{(2)}$ measurement of the X photon in Figure 5.12(a) under AC bias. AC amplitude: 0.3 V, pulse width: 300 ps, *f*= 203 MHz. $g^2(0)$= 0.13±0.014. (b) (left axis) Polarised second-order correlations in the circular basis in pulsed mode, *f*=303 MHz. (right axis with offset) Degree of correlation from the $g^{(2)}$s in circular basis.

5.7.2 Entanglement measurement

The most important assessment of the new E-LED is perhaps entanglement, which is the crucial requirement for the applications in this thesis. Reduced re-excitation and longer coherence from the emission should enhance the measurement of quantum entanglement in terms of post-selection timescale and fidelity. To measure entanglement, two-photon polarised correlations are recorded. The main challenge comes from the fact that the dot used here has a FSS of 15.83±0.76 μeV, which is considerably larger than the one used in the previous chapters.

Determining the entanglement fidelity to the maximally entangled state Ψ^+ requires measurements on three orthogonal planes on the Bloch sphere. Figure 5.14 (a)-(c) illustrates two-photon polarised correlation traces for each of the three bases. As expected, the presence of FSS manifests as fast oscillations with a period of 0.13 ns, when measuring time-dependent correlations of superposition states i.e. measuring in diagonal and circular bases. Here, the biexciton photon measurement causes the exciton photon polarisation to evolve with time and the exciton photon state to rotate around the Bloch sphere equator [42], [141]. However, the fast oscillations caused by the energetic splitting can be resolved with the fast SSPD response (69.7±9.8 ps). All correlations show a very low dip, which is the result of reduced re-excitation, as the probability of an X photon being emitted before an XX photon is small. Detector resolution and low background emission also contribute to this of course. The effect of reduced re-excitation is also clear from the cross-polarised trace in the rectilinear basis, which is almost flat for small positive delay times, in contrast to the clear bunching exhibited in Chapter 4 for the S-K QD.

The degree of correlation is calculated from the 3 sets of correlations using (2-9) and is shown in (d).

$$degree\ of\ correlation\ C_{a\bar{a}} = \frac{g^2_{aa} - g^2_{a\bar{a}}}{g^2_{aa} + g^2_{a\bar{a}}} \quad (2\text{-}9)$$

where g^2_{aa} denotes the two-photon correlation for co-polarised photons and $g^2_{a\bar{a}}$ denotes the correlation for cross-polarised pairs. The normalised traces are shown in Figure 5.14 (a). At time τ=0 the degree of correlation for each basis is found to be: 0.84±0.03 (Diagonal), 0.91±0.04 (Rectilinear) and -0.76±0.07 (Circular). The peak for the rectilinear basis is higher than the other two because of the large FSS and the nuclear spin interactions in the dot [142]. The result is damping of the oscillations in the circular and diagonal bases, so that the correlation in the rectilinear is stronger.

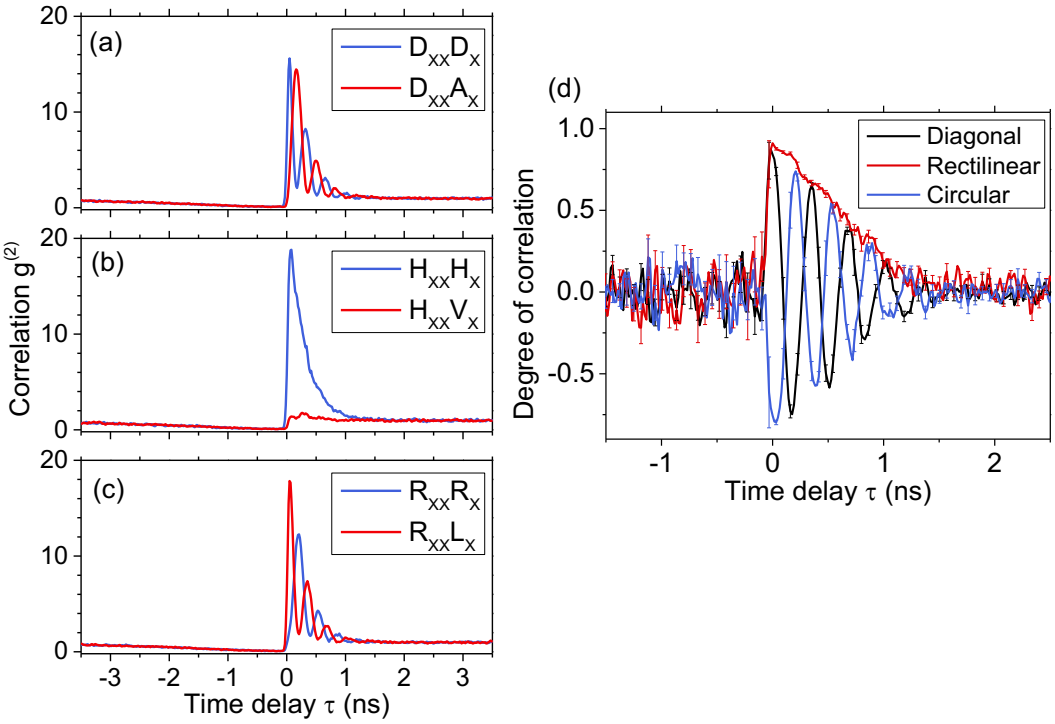

Figure 5.14: (Left) Two-photon polarised correlation traces for parallel and orthogonal photon pairs in each measurement basis: (a) Diagonal (b) Rectilinear (c) Circular. Average detector resolution: 69.7±9.8ps, bin size: 32 ps. (d) Degree of correlation extracted from the $g^{(2)}$s for each of the three bases. At time τ=0 the degree of correlation for each basis is found to be: 0.84 (0.03) (Diagonal), 0.91 (0.04) (Rectilinear) and -0.76 (0.07) (Circular).

The entanglement fidelity to the $|\Psi^+\rangle = (|H_{XX}|H_X\rangle + |V_{XX}|V_X\rangle)/\sqrt{2}$ state was measured for static Bell states in the rectilinear (HV), diagonal (DA) and circular (RL) bases. The calculated Entanglement fidelity *f* was determined using the expression (2-8) [77]:

$$f = \frac{1+C_{HV}+C_{DA}-C_{RL}}{4} \qquad (2\text{-}8)$$

where $C_{a\bar{a}}$ denotes the degree of correlation in the different polarisation bases.

Figure 5.15 (a) shows the measured entanglement fidelity *f* with a maximum of 0.88±0.03, well above the classical threshold of 0.5. The trace exhibits oscillations due to the evolution of the entangled state. Interestingly, the timescale of the fidelity being over the classical limit is longer than what was previously recorded for the S-K QDs.

Finally, Bell's parameters were extracted from the three static entangled states as a further assessment of the entanglement. The three bases represent three linearly independent planes on the Poincare sphere on which measurements are taken. Measurements from each pair of orthogonal planes can give a different Bell parameter in the following way [143]:

$$\begin{aligned} S_{DR} &= \sqrt{2}(C_{DA} + C_{HV}) \\ S_{DC} &= \sqrt{2}(C_{DA} - C_{RL}) \\ S_{RC} &= \sqrt{2}(C_{HV} - C_{RL}) \end{aligned} \qquad (5\text{-}2)$$

The calculated Bell parameters from the three states reach 2.48±0.09 (S_{DR}) 2.26±0.14 (S_{DC}) and 2.36±0.15 (S_{RC}). These values are well above 2, the threshold for violation of Bell's inequality, showing that the emission is entangled and useful for our entanglement-based applications. It is important to note that this is the first time entanglement is shown from an electrically-driven droplet epitaxy QD.

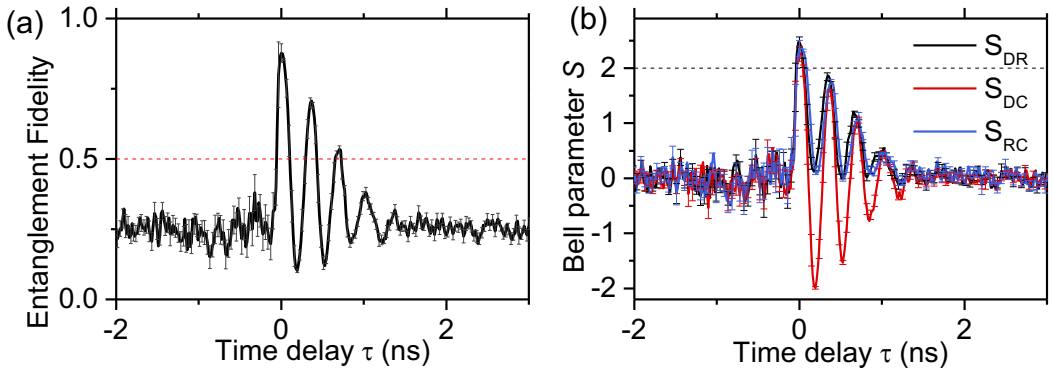

Figure 5.15: (a) Entanglement fidelity for all three polarization bases. The level at 0.5 indicates the maximum limit for a classical photon-pair source. Maximum fidelity *f*: 0.88±0.03. (b) Bell parameter extracted from the three static entangled states. A Bell parameter exceeding the classical limit of 2 indicates entangled light emission. Violation by σ: 5.27 (DR), 4.07 (DC), and 5.4 (RC).

5.7.3 Coherence time

The coherence time is limited by dephasing processes such as local charge fluctuations around the dot. More specifically, excess carriers around the dot may interact electrostatically with the electron-hole pairs in the dot. The creation of carriers is related to the injection conditions of the device and, following from the discussion about dot re-excitation, the presence of excess charge may be facilitated by the wetting layer in S-K dots.

Figure 5.16 (a) shows the spectrum of a D-E QD under electroluminescence, where an exciton X, a biexciton XX and a charged exciton X* are observed. The coherence length for each of these emission lines is obtained from first-order interference measurements, as described in Chapter 2. A Gaussian fit was used for the X (210.6±8.1 ps), X* (135.7±5.8 ps) measurements and an exponential decay fit was used for the XX (82.35±8 ps).

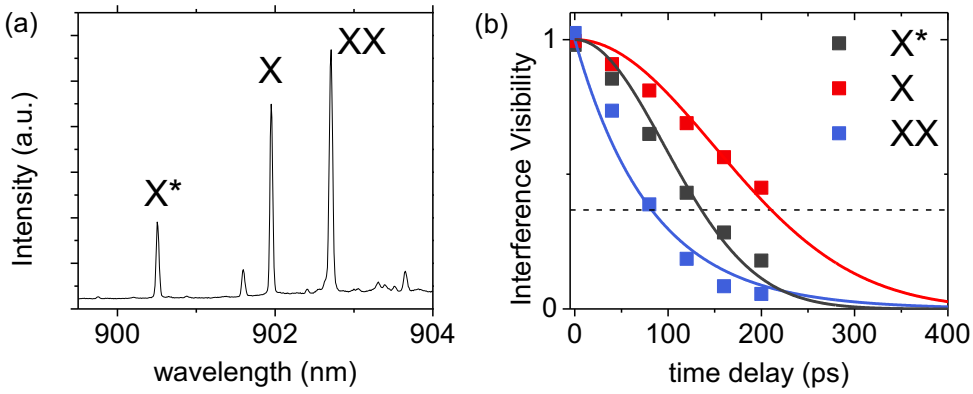

Figure 5.16: (a) Spectrum of the D-E QD used to obtain the D-E LED measurements (red stars in Figure 5.17). (b) Coherence time measurements for the excitons in (a).

Figure 5.17 (a) shows how the coherence times measured here compare to those reported in the literature. In general, D-E QDs (blue circles) fare worse than S-K dots, with some groups reporting linewidths up to hundreds of μeV. It is worth mentioning that these results are obtained under optical excitation. Directly comparable to these reports is the red circle point, which represents our measurement from an optical sample. The coherence time for this point is several orders of magnitude better than the rest. A possible explanation is the different growth techniques among research groups that might result in more or fewer defects being present in the lattice. The D-E QD in an LED shown in Figure 5.16 (b) is represented by the red star points. Note that these are also the only measurements recorded under electrical excitation. The coherence times of the D-E QD photons under electrical excitation are comparable to the S-K QD ones (black squares). The only points representing better coherence times were recorded under resonant optical excitation of S-K dots. From these results, we can confirm that the emission from a D-E QD in an E-LED in terms of coherence is at least just as good as the S-K QD E-LED. Improving the coherence time of the D-E QD emission further, either by growth or excitation method, can potentially provide a better emitter for future experiments.

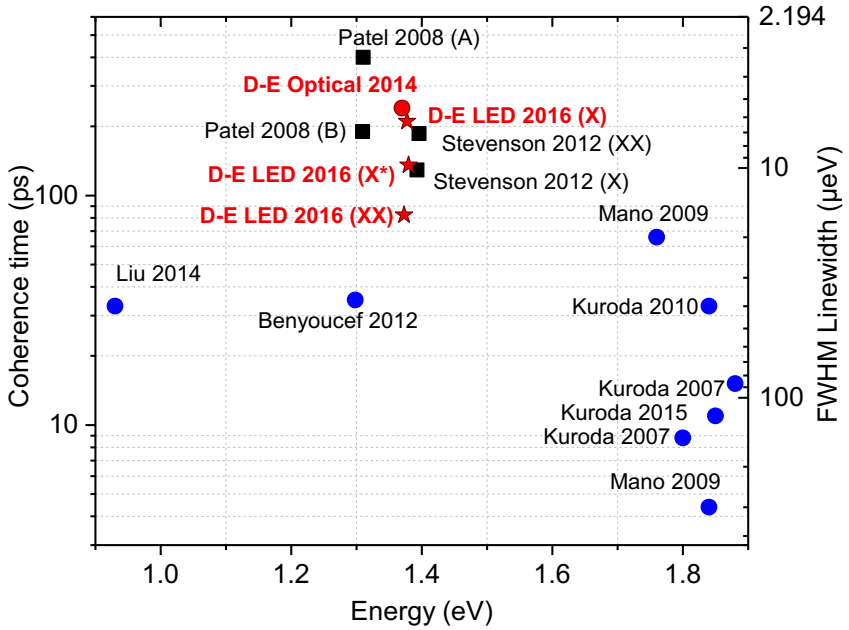

Figure 5.17: (a) Coherence time of single photons from quantum dots over various wavelengths, as reported in the literature: D-E QDs (blue circles), S-K QDs (black squares). The D-E samples used for this thesis are represented by measurements using optical excitation (red circle) and electrical excitation (stars). Other points refer to these publications: Kuroda 2015 [144], Kuroda 2010 [145], Mano 2009 [146], Benyoucef 2012 [147], Liu 2014 [123].

5.7.4 Higher Temperature Operation

The typical confinement energies for electrons and holes in QDs limit the operation to low temperatures only. In the InAs/ GaAs system, InAs QDs have been shown to perform better at liquid helium temperatures, where thermally-assisted carrier escape is reduced. There is a strong motivation for higher temperature operation for our semiconductor-based single-photon emitters, as it will make the transition from the lab to commercially available systems more realistic. The obstacles lie in the temperature dependence of optical properties of quantum dots, which is driven by the lattice relaxation based on exciton-acoustic phonon coupling [148] and exciton loss of confinement. Linewidth broadening and dephasing correlated with increasing temperature has been demonstrated on various QD systems [149], [150]. Single-photon emission at elevated temperature has been shown for other material systems such as group-III nitrides (300 K) [151] and InP/GaP (80 K) [152] amongst others. These systems operate in the visible range though and are not relevant to the applications discussed here. As far as GaAs is concerned, single-photon emission from neutral QD excitons has been shown at 77 K (0.3) [153], 100 K (0.260) [154] and for charged excitons at 80 K [155]. More recently, emission from a charged exciton at 1.55 μm at 80 K from quantum dashes has been reported (0.34) [156].

Figure 5.18 (a) shows quantum dot spectra taken at various temperatures from 30.8 K to 92.03 K. The spectrum shows narrow-linewidth, sharp lines for both X and XX photons, even at 48 K, which is higher than normal operating conditions. The linewidth broadens with increasing temperature, as expected, due to relaxation effects caused by electron-phonon interaction [157]. Two effects can be observed here: the broadening of the central emission frequency and the broadening of the background emission. The latter is more significant below 50 K and is attributed to phonon sidebands, corresponding to the coupling between excitons and acoustic phonons [158], [159]. The former effect exciton-LO phonon interaction is more dominant with increasing temperature [160] The emission peak redshifts to longer wavelengths, exhibiting a clear signature of a decreasing energy bandgap with high temperature, as predicted by the Varshni law [161]. This effect is illustrated by Figure 5.18. Remarkably, individual X and XX lines can be observed up to 81.75 K, which is unusual for InAs/GaAs QDs. Comparing with self-assembled S-K dots in particular, the presence of a wetting layer energy bandgap close to the dot states may enhance the non-radiative losses, resulting in earlier loss of carrier confinement and exciton coherence. More specifically, the wetting layer may absorb carriers from the dots via thermal emission [162], [163].

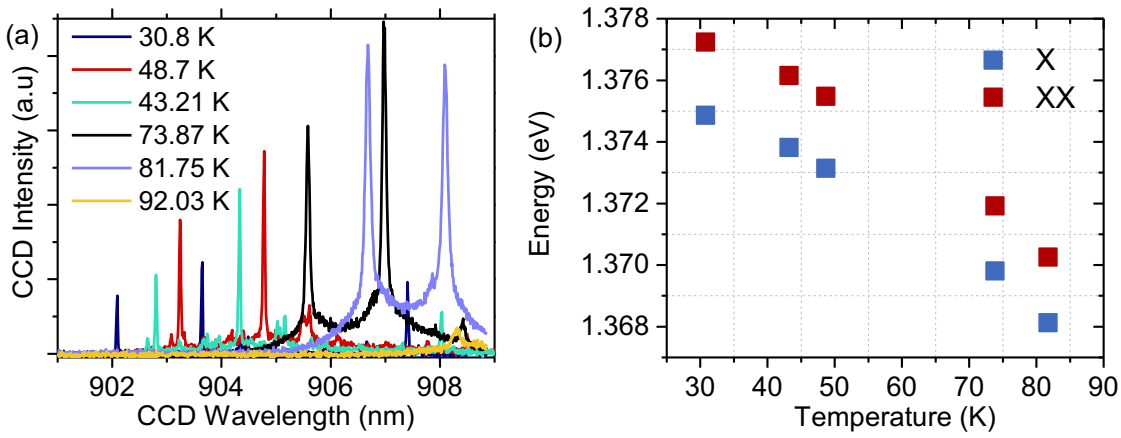

Figure 5.18: (a) Temperature-dependent spectra for a D-E QD under electrical excitation. (b) Exciton and biexciton emission energies against temperature. Spectral emission shifts to longer wavelengths with increasing temperature.

Figure 5.19 demonstrates how single-photon emission from a D-E QD exciton was achieved for temperatures up to 83.2 K (0.17). This opens new operational possibilities, since it surpasses the liquid nitrogen temperature threshold (77.2 K). The autocorrelation measurements show clear anti-bunching for all the temperatures recorded. Anti-bunched behaviour from $g^{(2)}$ measurements on InAs/GaAs QDs has been observed at 80 K, but the $g^{(2)}$ values are much higher: X* (0.29) [155] and X (~0.5) [164].

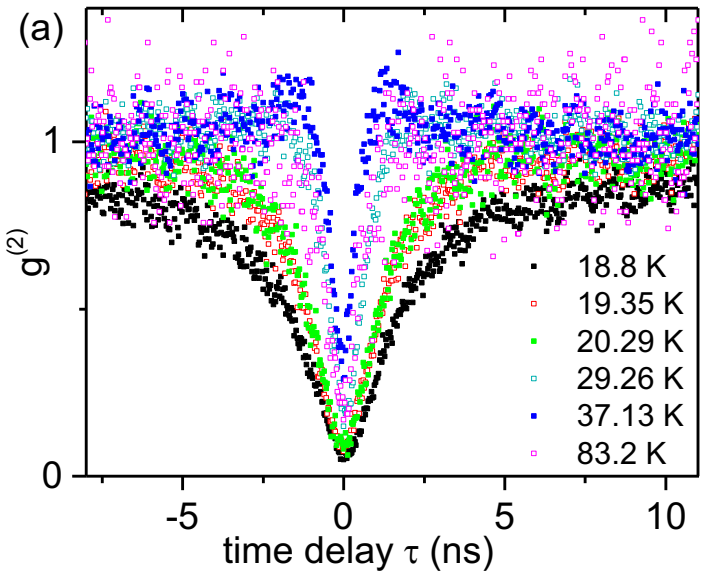

Figure 5.19: (a) $g^{(2)}$ measurement of the X photon for various sample temperatures up to 83.2 K. $g^{(2)}$ values: 18.8 K (0.05), 19.35 K (0.075±0.012), 20.29 K (0.06±0.015), 29.26 K (0.15±0.017), 37.13 K (0.29±0.03), 83.2 K (0.17 ±0.05).

5.8 Conclusion

This chapter has demonstrated the development of an entangled-LED based on the droplet epitaxy growth technique. It has recently been shown that the growth technique is universal and can be applied to other material systems such as InAs/InP by MOVPE (metal-organic vapour phase epitaxy), extending the emission to standard telecom wavelengths (1.55 μm) [165]. The growth approach enables flexibility in the engineering of the QDs by controlling the indium deposition temperature and volume. Another interesting feature is the formation of nanohole structures during the growth process, which may provide a method for site-controlled QDs of low density.

InAs QDs can be grown by droplet epitaxy on (001) substrates, enabling their incorporation into an optical microcavity, which has not been shown before for this type of dots. The D-E QDs exhibit small fine-structure splitting for a range of wavelengths, making them suitable for quantum communications applications. Entanglement fidelity reaching 0.88 from an electrically injected LED based on D-E QDs has been reported for the first time. In contrast to the S-K QDs, the single-photon character of the emission has demonstrated the potential for higher temperature single-photon emission, which could pave the way for more practical photonic emitters on GaAs. A $g^{(2)}$ of 0.17 was recorded at 83 K, which is the lowest for biexciton emission from an InAs QD at this elevated temperature so far to our

knowledge. Finally, the majority of QDs grown by droplet epitaxy have positive exciton binding energy, a requirement for resonant two-photon excitation of the biexciton state. The importance of this feature will be discussed in the next chapter, in which a two-photon biexciton state excitation experiment will be described. In conclusion, alternative methods of excitation in addition to new QD growth techniques could vastly enhance the single-photon purity and emission quality of the sources.

Chapter 6 Resonant two-photon biexciton excitation

6.1 Introduction

The previous chapters have explored the potential of a semiconductor QD-based E-LED as a quantum communications device. The limitations of the existing device have also been stressed. More specifically, Chapter 5 explored the development of an E-LED based on a different QD growth technique in order to address some of the issues, for instance the re-excitation of the biexciton cascade during a single cycle. In this chapter, the approach concerns the excitation method and explores the mechanisms towards the deterministic creation of entangled photon pairs.

In a semiconductor QD system, dephasing processes degrade the coherence of the photons and compromises their indistinguishability, a crucial requirement for future photonic quantum technologies and applications like quantum relays or repeaters. These processes are the result of strong interaction of the QD with its environment. In the case of incoherent excitation coupling of the dot to other states in the vicinity of the dot i.e. wetting layer or defect states may occur. More specifically, solid-state systems like quantum dots undergo dephasing due to phonon scattering [165], [167]. In general, the presence of free carriers and the consequent charge fluctuations in the QD surrounding material cause a small time-varying Stark shift in the emission wavelength, which ultimately leads to linewidth broadening [168]. The creation of excess carriers is related to the excitation density and method. Such charge fluctuations can be a source of dephasing and thus degradation of the coherence time of the emission [72], [169]. A straightforward way to alleviate the issue is to avoid creating excess carriers through incoherent above-band optical or electrical excitation by exciting the quantum dot s-shell directly under resonant optical injection [170]. Resonant excitation strategies have been shown to create deterministic and highly indistinguishable photons with almost transform-limited emission characteristics [171]–[175]. In these demonstrations, a coherent laser pulse is brought to resonance with the two-level solid-state system [170], [176]. More specifically to the applications explored in this thesis, the improvement

of the photon coherence time is crucial for extending the post-selection time scales. As discussed previously in Chapter 4, a wider post-selection time window can extend the efficiency of teleportation and improve the maximum fidelity that can be achieved. More recently, two groups have demonstrated entanglement and distinguishability from quantum dots grown with droplet etching under a resonant two-photon excitation scheme [177], [178].

Under resonant excitation schemes, the quantum dot is driven by a laser with frequency close to or at the emission energy (resonance fluorescence). For this reason, the experimental configuration requires a sophisticated laser suppression technique. Polarisation rejection schemes are widely used for resonant fluorescence [12]–[14] with success. In these configurations, the polarisations of the laser and the detected photons have orthogonal polarisations. It is thus straightforward that the technique cannot be employed for the generation of entangled photons. Another technique would be to use different geometries for the excitation and detection laser wave vectors. In such configurations, the quantum dot is excited from the side, with the sample cavity acting as a waveguide, while the light is collected from the top of the sample [167], [182]. Taking the above into consideration, the experiments in this chapter relied on a configuration that had not been implemented before for this type of experiments: normal laser incidence was implemented for practicality in conjunction with a simple pulse shaping technique for suppressing the scattered laser light, filtering only in the spectral domain.

6.2 Theoretical background

Two-photon excitation (TPE) in this chapter refers to the process in which the biexciton state is populated directly from the ground state by the simultaneous absorption of two photons of lower energy. The resonant excitation of the biexciton state via a two-photon process is schematically illustrated in Figure 6.1 (a). Assuming the case where the energy of the exciton is higher than the energy of the biexciton, the resonant TPE state is equal to half the biexciton state energy, so that two photons are required for excitation. The binding energy E_B is positive in this case and it is important to note that bound S-K dots are quite rare in our samples. The detuning of the laser frequency from the single exciton level E_X is given by δ. In the case where the excitation laser energy lies above the virtual TPE state (blue arrows) at detuning Δ, phonon-assisted excitation may be observed. Some experimental reports have shown how phonon coupling can be used for the initialisation of the biexciton state via an off-resonant optical pulse [167], [171], [181].

Figure 6.1 (b) shows an electroluminescence spectrum of the quantum dot. Under the resonant TPE scheme the pump laser is tuned to the virtual TPE level, which spectrally lies in between the exciton (1.4097 eV) and biexciton (1.4081 eV) emission lines, as shown in (b).

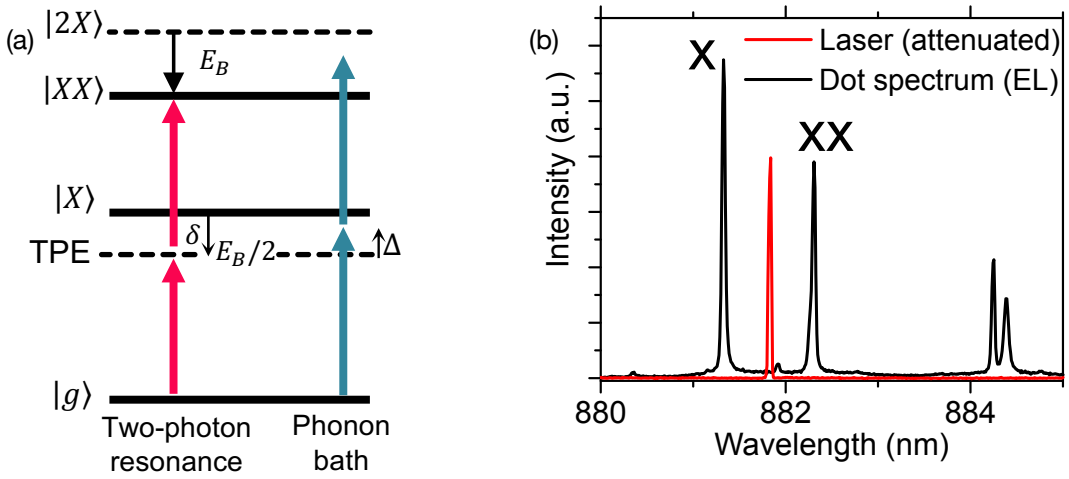

Figure 6.1: (a) Two-photon biexciton state excitation (red arrows) and phonon-bath (blue arrows) energy and optical transition levels. The TPE state energy is equal to half the biexciton state energy. In this configuration, the binding energy is positive. (b) A shaped laser pulse is tuned to be in resonance with the virtual biexciton TPE state. The energy of the TPE state is spectrally in the middle of the exciton and biexciton.

Under TPE, two optical photons of energy $E_B/2$ from the exciton level are used to excite the QD to the biexciton state. The laser field drives the population transfer between the two states found on the poles of the Bloch sphere in Figure 6.2. The rotation about the x axis is dependent on the pulse area θ. The excitation pulse induces a rotation of the Bloch vector, creating superpositions of the ground and biexciton state. As the driving field amplitude increases, the population switches between $|XX\rangle$ and $|g\rangle$, allowing the observation of Rabi oscillations. When a π-pulse is applied, the biexciton state is populated, followed by population of the exciton state via recombination and emission of a XX photon.

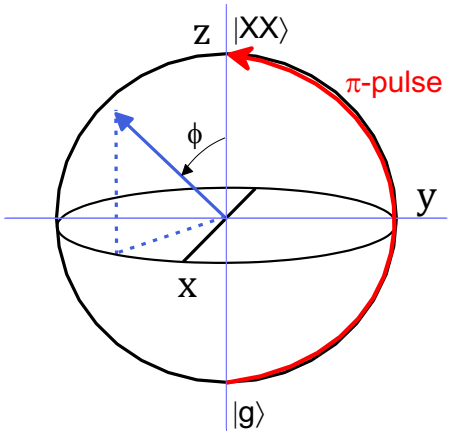

Figure 6.2: Bloch sphere representation of the biexciton population from ground state. The red arrow indicates the population inversion when the pulse area is π.

6.2.1 Modelling of two-photon Rabi oscillations

In contrast to single-exciton Rabi oscillations in two-level systems [183], [184], the population transfer in the biexciton cascade of a quantum dot via a coherent two-photon process does not vary sinusoidally with the pulse area of the driving field. In the two-photon excitation case here, the ground state is coupled to the biexciton state via the laser field and the transition $|g\rangle \rightarrow |XX\rangle$ via resonant excitation with two photons of energy $E_X - E_B/2$, is considered. If the laser is not tuned to the resonance frequency with $\delta = E_B/2$, the ground and biexciton states are not coupled and no Rabi oscillations can be observed.

Adopting the theoretical analysis from literature [176], [185], [186], a model based on a confined QD that is optically driven by a classical light field is implemented for calculating the population transfer from $|g\rangle \rightarrow |XX\rangle$ under TPE. The driving field is considered as laser pulses given by the Gaussian envelope:

$$f(t) = \frac{\theta}{\sqrt{2\pi}\tau_0} e^{-\left(\frac{t}{\tau_0}\right)^2/2} \quad (6\text{-}1)$$

where $\tau_0$is the nominal pulse width and θ is the integrated pulse area.

After the application of the driving pulse, the system acquires a dynamical phase α, which depends on the laser pulse amplitude, defined as:

$$\alpha = -\int_{-\infty}^{t} dt \frac{\delta}{2}\{1 - \sqrt{1 + 2[f(t)/\delta]^2}\} \quad (6\text{-}2)$$

where δ is the detuning of the laser frequency from the single exciton level E_X, as illustrated by Figure 6.1.

The state of the system becomes

$$|\psi\rangle = e^{\frac{i\alpha}{2}}[\cos\left(\frac{\alpha}{2}\right)|g\rangle + i\sin\left(\frac{\alpha}{2}\right)|XX\rangle] \quad (6\text{-}3)$$

and the occupation of the biexciton state is therefore given by

$$N_{XX} = |\langle XX|\psi\rangle|^2 = \sin^2\left(\frac{\alpha}{2}\right) \quad (6\text{-}4)$$

From the above expressions, the system is found to oscillate between the ground and biexciton states with increasing pulse amplitude.

Dephasing in the QD due to interactions with the environment can be observed as damping of the Rabi oscillations with increasing pulse area. Damping of the oscillation intensity may be caused by coupling to wetting layer [187][188] and other excitonic states [189], or more likely to acoustic phonons [190]. Driving the system harder leads to coupling to a larger phonon state density. A higher temperature also correlates with the dephasing, within the acoustic phonon model [191]. The exact mechanisms behind damping are not examined here. For simplicity, the intensity damping is assumed to have an exponential decay character so that the amplitude envelope can be characterised by $e^{-\theta^2/\tau_D}$, where τ_D is the loss of coherence time constant. Figure 6.3 (a) shows the effect of the laser pulse width and how the occupation of the biexciton state varies with increasing pulse area when the laser is on resonance with the TPE state. Increasing the width of the Gaussian laser pulse changes the period of the Rabi oscillations and shows how the shape of the field determines N_{XX}, an effect that has been explored before [176]. The effect of decoherence is illustrated in Figure 6.3 (b). The biexciton state occupation oscillates with an amplitude of 0 to 1 with increasing pulse area for the case of no decoherence, showing the transfer of population from the ground to the biexciton state. When a finite damping constant is included in the calculation the Rabi rotations become damped as the driving field increases. This loss of coherence was also observed experimentally.

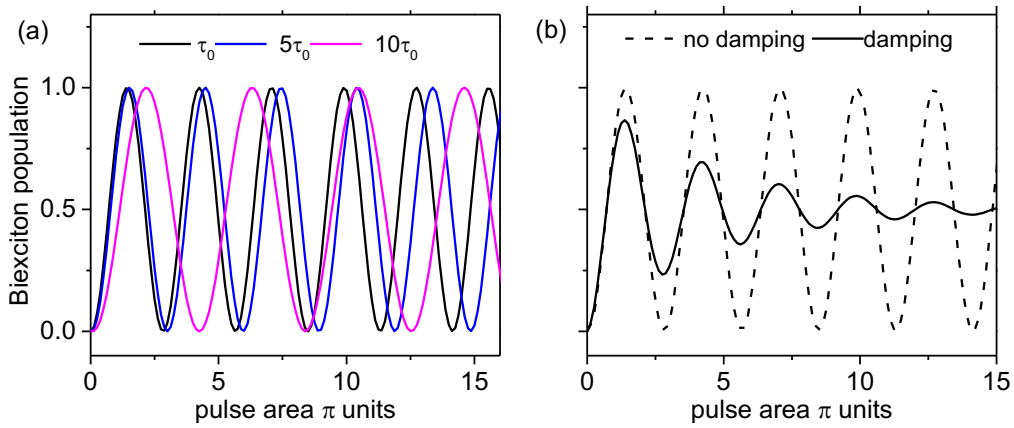

Figure 6.3: (a) Comparison of the biexciton state occupation for increasing pulse area and for different values of the laser pulse width (τ_o is the nominal pulse width, 2 ps). No damping is present. (b) The effect of the presence of damping due to incoherence on Rabi oscillations of the two-photon system.

6.3 Coherence time under electroluminescence

The main motivation behind the implementation of this resonant excitation scheme is to improve the effective coherence of the emission, so that the photon wave packets approach transform-limited characteristics. It is interesting to explore the effect temperature has on the coherence time under electrical injection for comparison. For this purpose, the dot emission coherence time was recorded for a temperature range of 7-23 K. For these measurements, the X-XX spectral intensity ratio was kept constant. Figure 6.4 (a) shows how the current flow varies under electroluminescence, as the temperature increases. Figure 6.4 (a) also illustrates how the coherence time of the emission changes for the same temperature points. A decrease in temperature corresponds to increased current flow for these measurement points, in order to keep the X-XX intensity ratio constant. Generally speaking, reports have shown how the loss of carrier confinement with increasing temperature and the increased interaction with external perturbations can limit the effective coherence time of the excitonic transitions [72], [168]. This dependency can be explained as the effect of non-radiative relaxation of excitons via phonon coupling, which is enhanced with increasing temperature. The measurements shown in Figure 6.4 (a), however, show that the coherence time of the emission decreases with decreasing temperature in this range (7-23 K). One possible explanation is that the dominant mechanism here is no longer phonon absorption but power broadening, caused by the increased delocalised carrier density due to higher current injection [72]. Charge fluctuations around the dots in this case may lead to spectral broadening and are limiting to our applications [192]. Under a resonant excitation scheme though, we expect to

manage the issue of having the carriers created in the wetting layer contributing to recapturing processes near the dot, thus increasing the TPI visibility between emitted photons [83].

It would be interesting to see whether the increase in current required to keep the intensity ratio constant corresponds to the increase of the energy bandgap as the temperature is reduced. Figure 6.4 (b) (pink circles) shows the current flow through the diode as a function of temperature for a constant voltage bias of 2 V. The current (left axis) increases with increasing temperature from 0.168 (7 K) to 0.223 mA (23 K), which corresponds to an increase of 24.6 %. Figure 6.4 (b) also shows how the quantum dot emission redshifts to longer wavelengths (right axis), a clear signature of a decreasing energy bandgap as the temperature increases. In contrast, the points in Figure 6.4 (a) show a current reduction from 1.3 (7 K) to 0.223 mA (23 K), which corresponds to a decrease of 480.9 %. In other words, trying to maintain the photon intensity ratio constant requires a high voltage bias as the temperature decreases and the massive difference in the two percentages suggests that the injection of carriers into the dot and subsequent recombination is not as efficient at low temperatures. In conclusion, the physical processes behind the dephasing in this quantum dot at low temperatures are not completely clear. The trend discussed here correlates the emission dephasing with increased power density, showing that operation at lower temperatures does not improve the coherence of the emission.

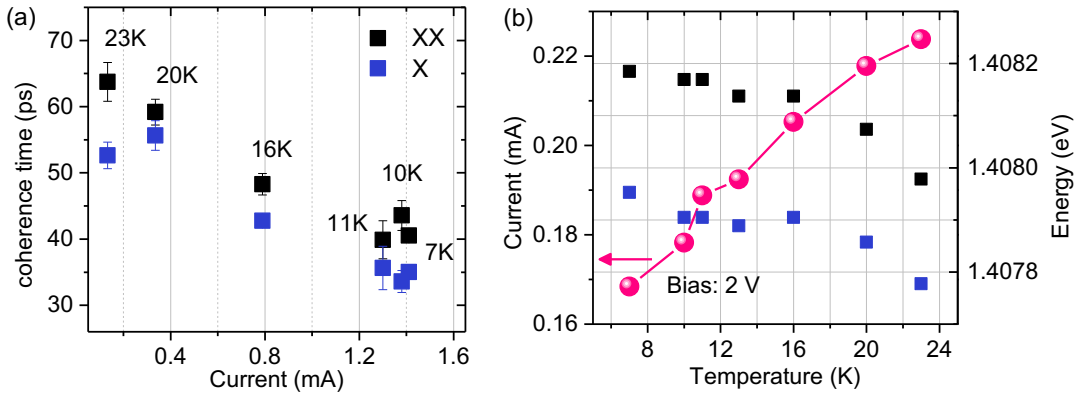

Figure 6.4: (a) Coherence time of exciton and biexciton emission as a function of the current flowing through the diode (temperature). (b) Left: Current flowing through the device as a function of increasing temperature at a bias of 2 V across the diode Right: Emission energy tuning of the exciton and biexciton as a function of increasing temperature.

6.4 Experimental Setup

The main technical challenge of this experiment comes from the need to suppress the scattered laser background reflected off the sample and leaking into the collection path. The novelty here stems from the fact that filtering of the laser in the spectral domain only was employed before excitation and after collection from the sample. The usual in-plane geometry was preserved for practical reasons, in contrast to other experimental demonstrations that employ side excitation arrangements reported in the literature. The small binding energy between exciton and biexciton of only 1.56 meV was also another limitation. This was partly addressed by extending the monochromator path length.

Detuning of the laser relative to the TPE energy level was achieved by varying the bias voltage applied on the diode. In contrast to most similar experimental setups, the laser wavelength is kept constant while the quantum dot emission is tuned by changing the electric field of the quantum dot.

6.4.1 Pulse shaping

A femtosecond Ti-Sapphire laser is used for optical excitation and a variable attenuator is in place to adjust the laser power output. The short-pulse unfiltered laser beam is spectrally wide, extending over 10 nm in the spectral domain. The pulse shaping technique for making the beam spectrally narrow is based on a 'double filter', which consists of two transmission gratings in series. A single transmission grating stage is able to separate the wavelengths of the beam by dispersing them at an angle, so that specific wavelengths are collected independently, as shown in Figure 6.5 (a). The laser beam is directed to the transmission grating with a resolution of 1500 l/mm and collected from it via fibre collimators with an 11 mm lens. The coupling fibres have a 5 μm core diameter, which act as spatial filters for the beam resulting in a Gaussian intensity profile. Given that the centre frequency of the excitation laser pulse is only ~715 μeV away from the two dot transitions, there will be some laser intensity overlapping with the dot emission. By introducing a second grating at this stage, the resulting beam profile will be a convolution of the two individual system response functions i.e. a Gaussian profile with a narrower width. The spectral FWHM of the output excitation laser pulse from a double grating stage is 180.3 (0.4) μeV, compared to 290.4 (0.5) μeV for a single, as shown in Figure 6.5 (b). The pulse FWHM reduction corresponds to a suppression factor of $\sim 4.6 \cdot 10^{11}$ of the laser intensity, where it overlaps with the dot emission.

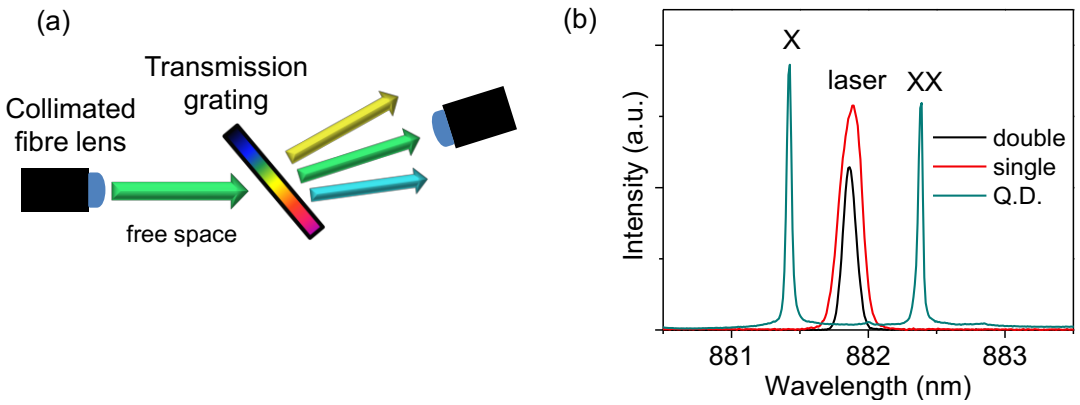

Figure 6.5: (a) Monochromator filter stage with a transmission grating. The collimated fibres shape the output laser pulse as a Gaussian mode. The different wavelengths of the incoming light are dispersed at an angle. (b) Spectral shape of the excitation laser pulse with a single (red) and a double (black) grating stage.

Figure 6.6 shows the full setup configuration. The double filter stage before the sample excitation was used to suppress the laser power (of the order of μW) and the rejection factor achieved for the laser light resonant with the X was ~10^3. Both monochromator filters are centred at the two-photon resonance frequency and have a total efficiency of ~30%. A beamsplitter (50:50 or 95:5) may be used to combine the excitation and collection paths. The first output of the beamsplitter is connected to a collimated lens fibre and excites the quantum dot via normal incidence. The second beamsplitter arm is directed to a power meter monitoring the laser power delivered to the sample. The emission from the dot is collected via the same path and directed to a monochromator, which consists of the third transmission grating stage in this setup and collimated fibres as before. This stage is used to separate the quantum dot emission before it is sent to the spectrometer. This monochromator filter has a Gaussian output intensity profile with a bandwidth of ~276 μeV. At this stage, there will be scattered laser light leaking through the collection paths, as shown in Figure 6.7. Spectroscopy measurements for observing Rabi oscillations or coherence time calculations may be carried out. An additional monochromator stage is required to further suppress the scattered laser light to carry out correlation measurements with photon counting detectors.

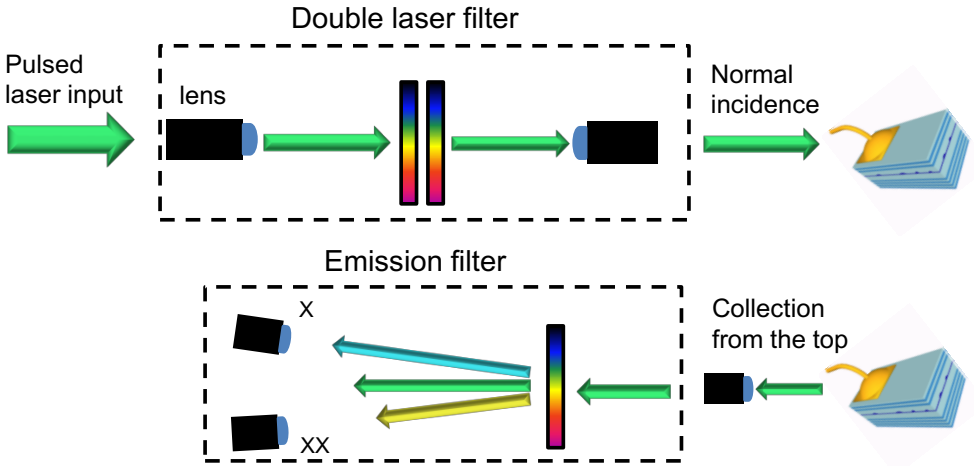

Figure 6.6: Experimental Setup for resonant two-photon biexciton state excitation. Two transmission grating filters are in place to suppress the excitation laser bandwidth, while coupling into collimated fibre lenses spatially filters the laser spectrum. The optical pump beam is incident on the sample from the top at normal incidence and the emission is collected via the same path. A second transmission grating stage is required to filter the QD emission for measurements and supress the laser background.

6.5 Results

6.5.1 Power-dependent spectroscopy

The resonant TPE process results in the emission of one exciton and one biexciton photon per cascade cycle and thus, the occupation level of the states should be the same. Figure 6.7 shows the quantum dot spectrum under the TPE scheme, after the emission filter stage. With each excitation cycle the biexciton state can be populated, while the exciton state is populated through the radiative cascade after the biexciton recombination.

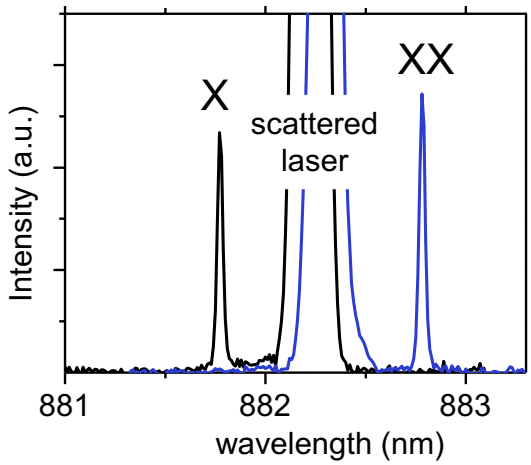

Figure 6.7: Emission spectrum under two-photon biexciton state excitation after the emission filter. Two separate collimated fibres centred at the exciton and biexciton frequencies are used to collect the emission from the quantum dot. Some residual scattered laser light is still present.

The exciton X and biexciton XX populations were probed by spectroscopy measurements as a function of the excitation power. Pulse area-dependent two-photon Rabi oscillations between the ground and biexciton states are a signature of coherent two-photon transitions between the two states. Figure 6.8 (a) shows the variation of the exciton and biexciton photon intensities as a function of the pulse area θ. Rabi oscillations can be observed from the emission intensity and can be interpreted as the result of a two-level system driven coherently by a pump laser field. Increasing the pulse area causes the biexciton cascade system to oscillate between the ground state and the biexciton state. For a pulse area equal to π, which corresponds to one half rotation on the Bloch sphere, the system is transferred from ground to the biexciton state and the oscillation is at its maximum. The oscillations exhibit rapid damping and a limited number of visible oscillations. The characteristic intensity damping is attributed to power-dependent dephasing, probably caused by acoustic phonon coupling [167], [193] and the presence of competing non-resonant processes caused by the creation of carriers in the vicinity of the dot [194], as explained in section 6.2.

The two-photon transition may be driven off-resonantly by introducing a difference Δ_{det} between the two-photon resonance energy level and the laser. Figure 6.8 (b) shows the case where the laser is positively detuned from the two-photon resonance energy level. The phonon-bath case is illustrated by Figure 6.1 (a). Under this excitation regime, the amplitude and the mean value of the Rabi oscillation intensities are reduced with increased detuning [167]. No sinusoidal oscillations of the emission intensity of the exciton can be observed.

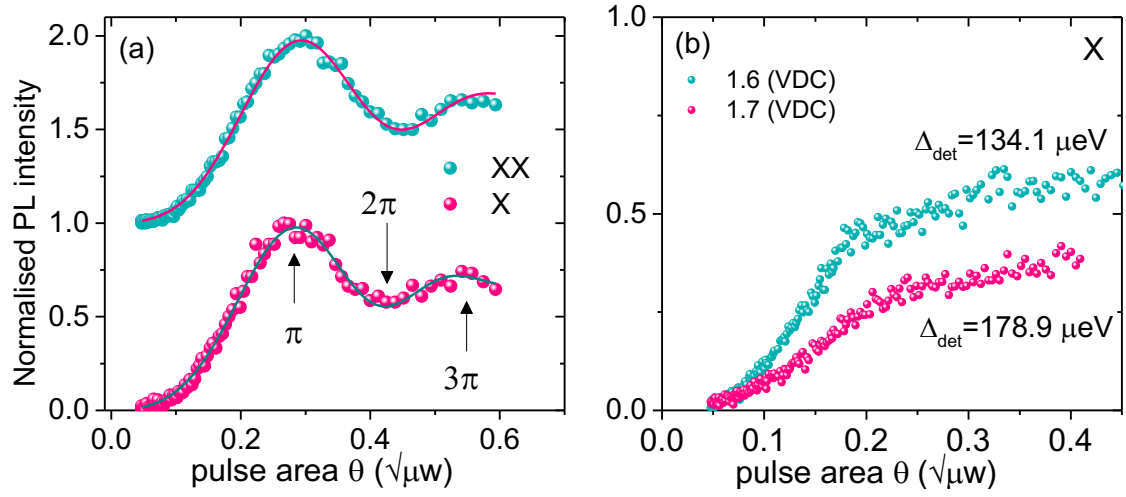

Figure 6.8: (a) PL intensities for the exciton and biexciton emission under resonant TPE conditions (normalised to photon intensity at π-pulse). Rabi-type oscillations of the biexciton XX (offset=1) and exciton X populations are observed as a function of the pulse area θ. The fitted curves include an exponential damping factor. (b) Incoherent two-photon excitation of the exciton state for finite laser detuning Δ_{det} from the TPE energy level.

The Rabi oscillations in Figure 6.8 (a) were fitted using the sinusoidal expression in (6-5), adopted from the analysis in 6.2.1. The power-dependent exponential decay factor was added to account for the presence of decoherence:

$$\sin^2\frac{\alpha}{2}\exp\left(-\frac{\theta^2}{\tau_D}\right)+\left(1-\exp\left(-\frac{\theta^2}{\tau_D}\right)\right)*0.5 \qquad (6\text{-}5)$$

where τ_D is a damping factor and the dynamical phase function $\alpha(\theta)$ is now approximated by:

$$\alpha=\sqrt{a^2+(b\theta)^2}-a \qquad (6\text{-}6)$$

The expression in (6-6) is the numerically evaluated approximation of (6-2), which seems to match the experimental data well. Constants a and b are extracted by the fits.

6.5.2 Second-order correlations

The single-photon purity was assessed by measuring the second-order correlation function of the quantum dot emission. Figure 6.9 shows the exciton autocorrelation function, for which $g_X^{(2)}(0)$ = 0.036 (0.008) at time zero delay. This result shows a great improvement from previous measurements of S-K quantum dots under electrical injection, where the effects of the dot re-excitation are prominent

around τ=0. The central peak is suppressed indicating the purity of the single-photon emission under the resonant excitation scheme.

The non-zero $g_X^{(2)}$ at zero delay time can be attributed to scattered laser photons leaking through the monochromator filter and detector nonidealities. No background subtraction was done to remove these effects. The first effect is mostly the consequence of the small binding energy and the fact that the laser wavelength is too close to the exciton transition.

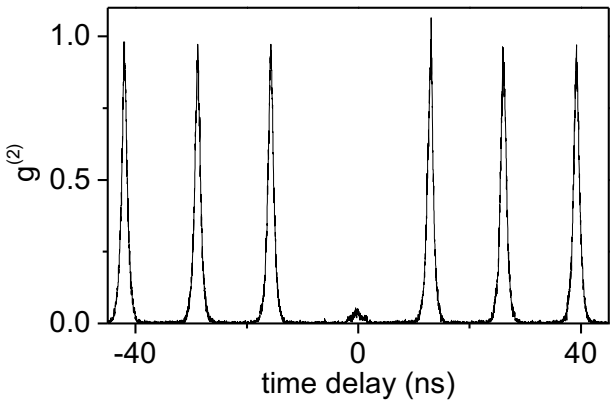

Figure 6.9: Exciton $g_X^{(2)}$= 0.036 ± 0.008. The zero-delay peak is greatly suppressed. It is possible that some counts come from residual laser background leaking through the filter due to the proximity of the laser frequency to the exciton line. No background subtraction was done.

6.5.3 Coherence time measurements

Due to the resonant nature of the excitation and the fact that no above-band excitation takes place, the coherence length of the QD emission is expected to be longer. The exciton and biexciton coherence times were measured with a Michelson interferometer and under resonant two-photon excitation. Figure 6.10 (a) shows the exciton coherence time τ_c, extracted from the Michelson interference visibility and fitted with an exponential decay of the form $\exp\left(-\frac{t}{\tau_c}\right)$. The measured values show an increase from 119.76 ± 5.22 ps (X) and 106.25 ± 2.36 ps (XX) under electroluminescence to 263 (25.3) ps and 219.6 (19.5) ps in the resonant TPE regime for the exciton and biexciton, respectively (the relevant measurement is given in the Appendix). The results correspond to an improvement in the effective coherence time τ_c by at least factor of 2 for both photons. The improvement is in agreement with other reports and is related to the suppression of dephasing mechanisms in the dot surroundings. Excitation under this scheme excites the biexciton state directly and therefore avoids phonon relaxation and charge scattering processes [195]. The exponential decay fit which points to a Lorentzian profile

of the emission suggests that homogeneous broadening related to a fluctuating environment is also minimised. However, dephasing processes like spectral diffusion still take place and the coherence time is still not dictated only by the lifetime of the emission, according to studies on similar emitters [195]. No lifetime measurements were carried out with this QD.

Figure 6.10 (b) shows the exciton coherence time as a function of temperature under TPE (red point) and for finite laser frequency detuning from the TPE level (blue and black). The highest coherence time is obtained for Δ=0 and T=7 K and corresponds to the measurement in (a). For finite laser frequency detuning, the excitation corresponds to a phonon-assisted process. There is also a clear dependency on the temperature, with the coherence time improving with decreasing temperature. The reason is the reduced dephasing caused by phonon coupling [190], as discussed in 6.2.

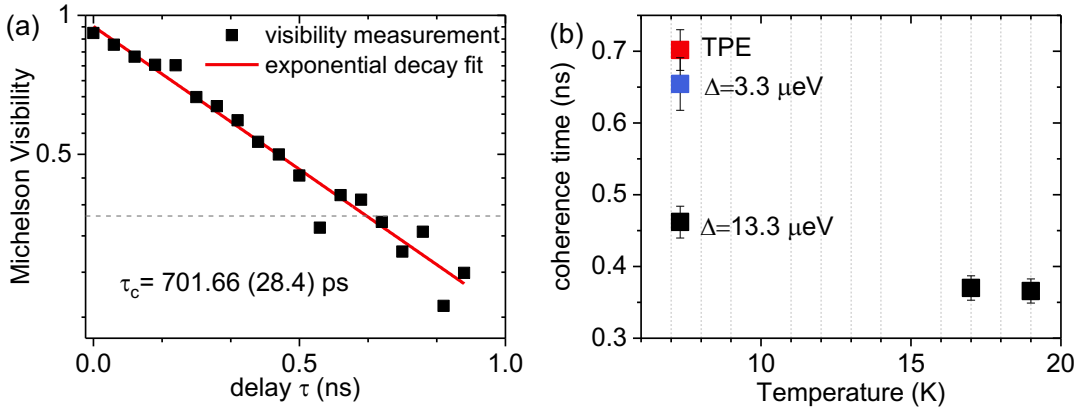

Figure 6.10: (a) Coherence time measurement under TPE (red point). (b) Evolution of coherence time of the exciton photon measured at various sample temperatures and bias voltages. Highest coherence time points occur at lowest temperatures.

6.5.4 Binding energy effect on TPE

Figure 6.1 shows the states and the energy levels involved in a TPE scheme of the biexciton transition, where the quantum dot binding energy is positive. Interestingly, there are no reports of TPE observation on a dot with negative binding energy. This is quite important for us, since most our SK-grown quantum dots are anti-bound. As a result, the implementation of the TPE scheme adapted to the anti-bound quantum dot used in the previous experiments was attempted.

The laser is adjusted to be in halfway between the exciton and biexciton spectral emission, following the same procedure as above. Figure 6.11 illustrates the attempted scheme and the corresponding state

transitions. The virtual resonance state lies higher in energy than the exciton state in the case of negative binding energy. The results from the scheme are shown in Figure 6.12.

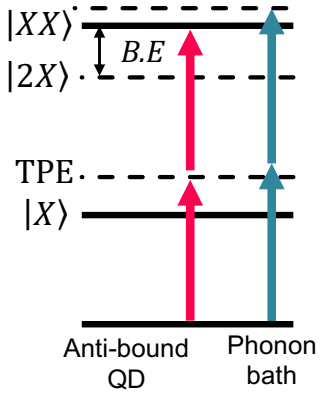

Figure 6.11: States and energy levels for resonant two-photon excitation attempt of an anti-bound quantum dot. The virtual state lies higher in energy than the exciton level.

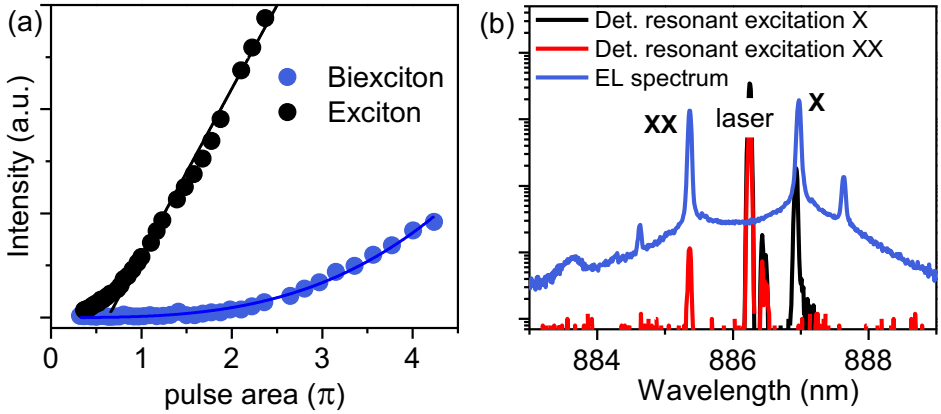

Figure 6.12: Detuned resonant excitation of an S-K dot (QD used for previous experiments) under TPE conditions. (a) Exciton and biexciton intensities as a function of pulse area. (b) Emission spectra for exciton and biexciton under non-resonant optical excitation after monochromator stage 3.

Figure 6.12 (a) shows the exciton and biexciton intensities as a function of pulse area. No Rabi oscillations indicating the coherent population transfer in a two-level system can be observed. The approximately linear (X) and super-linear (XX) power dependencies of the intensities suggest that a non-coherent excitation process is taking place. It was thus verified that it is not possible to resonantly excite the biexciton state via a two-photon transition. The mechanism behind this can be traced back to Figure 6.11, which shows that the exciton state will be excited through a phonon-assisted process, since the

pump laser frequency (virtual state) lies higher in energy. It is possible that other incoherent processes contribute to this excitation scheme, for example carrier excitation in the surrounding material.

Characterisation of the emission under this detuned resonant optical excitation scheme yielded good results that can be of practical use for our quantum teleportation applications. The exciton and biexciton coherence times showed an increase from 141.6 (4.3) ps (XX) and 121 (3.8) ps (X) under electroluminescence (quantum relay experiment conditions) to 275.2 (20.2) ps and 291.6 (7.8) ps for the biexciton and exciton respectively (the relevant measurement is given in the Appendix). The emission of this anti-bound dot thus exhibits similar coherence length improvement as the emission of the bound dot under the resonant two-photon method in 6.5.3. Similar arguments hold for the origin of the improvement; the excitation is not above-band, no WL excitation takes place and thus phonon coupling and charge fluctuations are suppressed.

Figure 6.13 (a) and (b) show the autocorrelation functions for the biexciton and exciton photons respectively. Multi-photon emission at $\tau=0$ is strongly suppressed and this is clear from the very low $g^{(2)}(0)$ values, demonstrating high purity of single-photon emission.

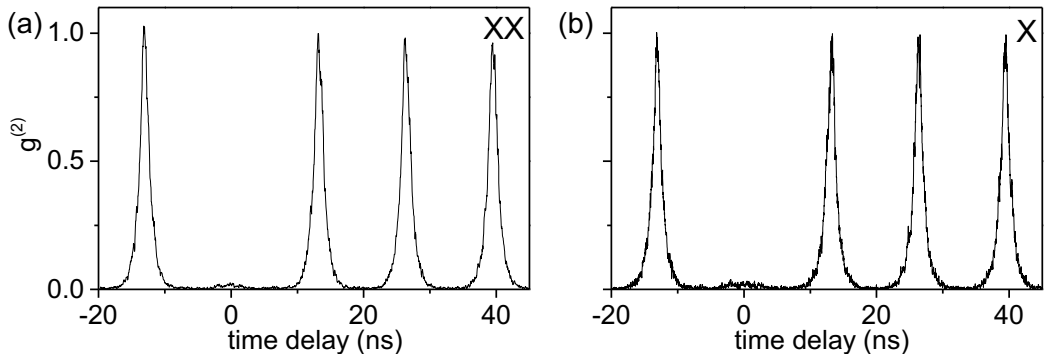

Figure 6.13: $g^{(2)}$ measurements under detuned resonant optical excitation of the anti-bound QD. (a) biexciton $g_{XX}^{(2)}(0) = 0.016\ (0.04)$ (3.7 μW) (b) exciton $g_{XX}^{(2)}(0) = 0.013\ (0.04)$ (1.82 μW).

To sum up, the coherence times and single-photon purity of the generated photons are comparable to what was measured under a fully resonant TPE scheme. The result is encouraging, as it shows that the majority of the S-K dots in our samples could be used for more sophisticated quantum teleportation schemes requiring longer photon coherence times, under excitation with the arrangement presented in this section.

6.6 Conclusions

In summary, it was experimentally demonstrated that resonant TPE can be achieved for a QD biexciton state only if the binding energy is positive because phonon assisted excitation of the exciton state Rabi oscillations were shown proving the coherent population transfer from ground to the biexciton state. Quantum dots grown by droplet epitaxy, as described in Chapter 5, are great candidates for this excitation scheme because of the high density of bound exciton pairs on the samples. The characteristic damping of Rabi oscillations is attributed mainly to acoustic phonon coupling of the QD states and the consequent loss of coherence with increasing power.

It has been shown that, under a resonant TPE scheme emission from a QD can be optimised by suppressing the effects of the interaction with the surrounding crystal i.e. phonon coupling. The improved coherence length and hence indistinguishability of the QD photons and is very promising for extending the range of applications of our QD emitters. Entanglement swapping or higher rate quantum relay configurations are such examples.

Chapter 7 Conclusions & Future Work

The chapters in this thesis have explored the potential of the Entangled-Light Emitting diode as a key component in future quantum networks. Using InAs quantum dots embedded in an electrically-injected p-i-n diode, the device is able to emit entangled photon pairs through the biexciton cascade. Chapter 3 investigated the quantum interference of the entangled biexciton photons with laser photons, under pulsed electrical injection at a frequency of a few hundred MHz. The new E-LED design with smaller diode mesas and improved electrical characteristics allowed the operation of the E-LED under AC electrical bias, which had not been previously demonstrated. The high two-photon interference results verified the indistinguishability between the two dissimilar photon sources, which was a pre-requisite for the quantum teleportation operation in Chapter 4. A quantum dot with relatively small fine-structure splitting was chosen and used as the single-photon emitter for the experiments in both chapters. In chapter 4, the implementation of a quantum relay scheme using the E-LED and laser photons as input qubits was demonstrated over 1 km of fibre. One of the challenges in this arrangement arises from the fact that it was the first time entanglement distribution over a somewhat significant distance was shown for a quantum dot. The rest of the technical challenges lay in the pulsed operation of both laser and quantum dot sources. Reaching a compromise between the major requirements for a high-quality single-photon emitter i.e. high photon pair entanglement fidelity, long biexciton coherence time and high single photon counts, dictated the electrical bias conditions of the device. The high quantum relay fidelity of 0.9 allows for error correction using BB84-based protocols, making the setup suitable for practical entanglement-based QKD applications.

In Chapter 5, a new technique of InAs/GaAs quantum dot growth was explored. The main motivation behind this undertaking was to improve the existing devices and address the quantum dot re-excitation issue speculatively caused by the presence of a wetting layer close to the QD layer. In this chapter, the development of an E-LED based on droplet epitaxy QDs is demonstrated. Firstly, the effect that growth parameters such as indium content and temperature have on the optical properties of the dots, until a satisfactory recipe is obtained was investigated. In the rest of the chapter the optical properties of the dots are assessed. Small fine-structure splitting has been shown for emission wavelengths around 900 nm, longer than what was previously achieved. Emission from DE-QD in a cavity was obtained

for the first time, showing that the technique can easily be adopted into the existing device designs. Finally, high degree of entanglement was achieved from an electrically-driven DE-QD. In addition, the operation of the electrical device at increased temperatures was investigated, showing the potential of the DE-QDs to emit single photons at liquid nitrogen temperature.

As an alternative solution to the re-excitation issue of the QDs, a resonant two-photon excitation technique was explored in Chapter 6. Improvement in the quality and single-photon purity of the emission was expected by avoiding excitation of the wetting layer, which occurs during electrical injection. Observation of Rabi oscillations demonstrated that the QD could be optically addressed via a two-photon absorption process. The optical properties of the emission under this type of excitation demonstrated improvement in the exciton coherence time and in the second-order correlation.

These results are very promising for future implementations of quantum teleportation-based applications. Longer coherence times of the QD emission combined with reduced QD re-excitation can increase the post-selection time window of photon coincidences. In addition, the detector resolution would not be a limiting factor for correlation measurements in this case. Therefore, repeating the two-photon interference and quantum relay experiment would yield better results. The experiment running time would also be reduced, as more 3-photon coincidences would be recorded. An entanglement swapping scheme based on an E-LED would be an extension of this work, but a challenging task for current devices. Resonant two-photon biexciton excitation techniques with DE-QDs may provide a viable solution. There is, however, a lot of room for improvement when it comes to the TPE laboratory arrangement in terms of photon collection efficiency, laser rejection filtering and wavelength tuning. The physics behind the TPE method were not fully explored, especially combined with the excitation of a pin diode, therefore it would be interesting if a theoretical model was also developed.

As a continuation from Chapter 5, further research into optimising the growth of InAs QDs by droplet epitaxy is needed. Combined with a better understanding of the excitation dynamics in this system, the single-photon emission can be further improved. After the promising results of single-photon emission at higher temperatures, an interesting experiment would be to carry out correlation measurements under liquid Nitrogen cooling. Finally, an obvious practical question is extending this work to telecom wavelengths i.e. 1.3 μm and 1.55 μm. Steps for pushing the emission of QDs to longer wavelengths are already being undertaken [165] and the results are very promising [116].

Bibliography

[1] N. Bohr, 'I. On the constitution of atoms and molecules', *Philos. Mag. Ser. 6*, vol. 26, no. 151, pp. 1–25, Jul. 1913.

[2] W. Heisenberg, 'Die beobachtbaren Grössen in der Theorie der Elementarteilchen. II', *Z. Für Phys.*, vol. 120, no. 11, pp. 673–702, 1943.

[3] E. Schrödinger and M. Born, 'Discussion of Probability Relations between Separated Systems', *Math. Proc. Camb. Philos. Soc.*, vol. 31, no. 4, p. 555, Oct. 1935.

[4] A. Einstein, B. Podolsky, and N. Rosen, 'Can Quantum-Mechanical Description of Physical Reality Be Considered Complete?', *Phys Rev*, vol. 47, no. 10, pp. 777–780, May 1935.

[5] J. Bub, 'Quantum Entanglement and Information'. 2015.

[6] T. P. Spiller, 'BASIC ELEMENTS OF QUANTUM INFORMATION', *Introd. Quantum Comput. Inf.*, p. 1, 1998.

[7] J. Benhelm, G. Kirchmair, C. F. Roos, and R. Blatt, 'Towards fault-tolerant quantum computing with trapped ions', *Nat. Phys.*, vol. 4, no. 6, pp. 463–466, Jun. 2008.

[8] G. D. Fuchs, G. Burkard, P. V. Klimov, and D. D. Awschalom, 'A quantum memory intrinsic to single nitrogen–vacancy centres in diamond', *Nat. Phys.*, vol. 7, no. 10, pp. 789–793, Jun. 2011.

[9] C. Santori, D. Fattal, J. Vučković, G. S. Solomon, and Y. Yamamoto, 'Indistinguishable photons from a single-photon device', *Nature*, vol. 419, no. 6907, pp. 594–597, 2002.

[10] J. Clarke and F. K. Wilhelm, 'Superconducting quantum bits', *Nature*, vol. 453, no. 7198, pp. 1031–1042, Jun. 2008.

[11] J. S. Bell, On the Einstein Podolsky Rosen paradox. 1964.

[12] S. J. Freedman and J. F. Clauser, 'Experimental test of local hidden-variable theories', *Phys. Rev. Lett.*, vol. 28, no. 14, p. 938, 1972.

[13] B. Hensen *et al.*, 'Loophole-free Bell inequality violation using electron spins separated by 1.3 kilometres', *Nature*, vol. 526, no. 7575, pp. 682–686, Oct. 2015.

[14] L. K. Shalm *et al.*, 'Strong Loophole-Free Test of Local Realism', *Phys. Rev. Lett.*, vol. 115, no. 25, Dec. 2015.

[15] M. Giustina *et al.*, 'Significant-Loophole-Free Test of Bell's Theorem with Entangled Photons', *Phys. Rev. Lett.*, vol. 115, no. 25, Dec. 2015.

[16] P. W. Shor, 'Polynomial-time algorithms for prime factorization and discrete logarithms on a quantum computer', *Siam J. Comput.*, vol. 26, no. 5, pp. 1484–1509, Oct. 1997.

[17] C. H. Bennett, 'Quantum cryptography: Public key distribution and coin tossing', in *International Conference on Computer System and Signal Processing, IEEE, 1984*, 1984, pp. 175–179.

[18] M. A. Horne, A. Shimony, and A. Zeilinger, 'Two-particle interferometry', *Phys. Rev. Lett.*, vol. 62, no. 19, p. 2209, 1989.

[19] J. D. Franson, 'Bell inequality for position and time', *Phys. Rev. Lett.*, vol. 62, no. 19, p. 2205, 1989.

[20] P. G. Kwiat, E. Waks, A. G. White, I. Appelbaum, and P. H. Eberhard, 'Ultrabright source of polarization-entangled photons', *Phys. Rev. A*, vol. 60, no. 2, p. R773, 1999.

[21] M. H. Rubin, D. N. Klyshko, Y. H. Shih, and A. V. Sergienko, 'Theory of two-photon entanglement in type-II optical parametric down-conversion', *Phys. Rev. A*, vol. 50, no. 6, p. 5122, 1994.

[22] P. W. Shor, 'Algorithms for Quantum Computation: Discrete Logarithms and Factoring', in *Proceedings of the 35th Annual Symposium on Foundations of Computer Science*, Washington, DC, USA, 1994, pp. 124–134.

[23] L. K. Grover and J. Radhakrishnan, 'Is Partial Quantum Search of a Database Any Easier?', in *Proceedings of the Seventeenth Annual ACM Symposium on Parallelism in Algorithms and Architectures*, New York, NY, USA, 2005, pp. 186–194.

[24] D. R. Simon, 'On the Power of Quantum Computation', *SIAM J Comput*, vol. 26, no. 5, pp. 1474–1483, Oct. 1997.

[25] N. Gisin and R. Thew, 'Quantum communication', *Nat Photon*, vol. 1, no. 3, pp. 165–171, Mar. 2007.

[26] R. Van Meter and J. Touch, 'Designing quantum repeater networks', *IEEE Commun. Mag.*, vol. 51, no. 8, pp. 64–71, 2013.

[27] S. Reitzenstein and A. Forchel, 'Quantum dot micropillars', *J. Phys. Appl. Phys.*, vol. 43, no. 3, p. 33001, Jan. 2010.

[28] K. Hennessy *et al.*, 'Quantum nature of a strongly coupled single quantum dot-cavity system', *Nature*, vol. 445, no. 7130, pp. 896–899, Feb. 2007.

[29] A. Faraon, D. Englund, I. Fushman, J. Vučković, N. Stoltz, and P. Petroff, 'Local quantum dot tuning on photonic crystal chips', *Appl. Phys. Lett.*, vol. 90, no. 21, 2007.

[30] K. Srinivasan and O. Painter, 'Linear and nonlinear optical spectroscopy of a strongly coupled microdisk-quantum dot system', *Nature*, vol. 450, no. 7171, pp. 862–865, Dec. 2007.

[31] E. Knill, R. Laflamme, and G. J. Milburn, 'A scheme for efficient quantum computation with linear optics', *nature*, vol. 409, no. 6816, pp. 46–52, 2001.

[32] A. Rastelli, S. Kiravittaya, and O. G. Schmidt, 'Growth and control of optically active quantum dots', in *Single Semiconductor Quantum Dots*, P. Michler, Ed. Berlin, Heidelberg: Springer Berlin Heidelberg, 2009, pp. 31–69.

[33] S. Bellucci, Self-Assembly of Nanostructures: The INFN Lectures. Springer New York, 2011.

[34] E. Cohen *et al.*, 'Structure of droplet-epitaxy-grown InAs/GaAs quantum dots', *Appl. Phys. Lett.*, vol. 98, no. 24, p. 243115, 2011.

[35] O. Schilling, A. Forchel, and M. Lebedev, 'Deep etched InGaAs/InP quantum dots with strong lateral confinement effects', *Superlattices Microstruct.*, vol. 16, no. 3, pp. 261–264, 1994.

[36] F. Houzay, C. Guille, J. M. Moison, P. Henoc, and F. Barthe, 'First stages of the MBE growth of InAs on (001) GaAs', *J. Cryst. Growth*, vol. 81, no. 1–4, pp. 67–72, 1987.

[37] R. E. Hummel, *Electronic Properties of Materials*. Springer New York, 2011.

[38] R. J. Young, R. M. Stevenson, A. J. Shields, P. Atkinson, K. Cooper, and D. A. Ritchie, 'Entangled photons from the biexciton cascade of quantum dots', *J. Appl. Phys.*, vol. 101, no. 8, p. 81711, 2007.

[39] M. Bayer *et al.*, 'Fine structure of neutral and charged excitons in self-assembled In(Ga)As/(Al)GaAs quantum dots', *Phys. Rev. B*, vol. 65, no. 19, May 2002.

[40] H. W. Van Kesteren, E. C. Cosman, W. Van der Poel, and C. T. Foxon, 'Fine structure of excitons in type-II GaAs/AlAs quantum wells', *Phys. Rev. B*, vol. 41, no. 8, p. 5283, 1990.

[41] R. M. Stevenson *et al.*, 'Quantum dots as a photon source for passive quantum key encoding', *Phys Rev B*, vol. 66, no. 8, p. 81302, Aug. 2002.

[42] R. M. Stevenson *et al.*, 'Evolution of Entanglement Between Distinguishable Light States', *Phys. Rev. Lett.*, vol. 101, no. 17, Oct. 2008.

[43] A. J. Hudson *et al.*, 'Coherence of an Entangled Exciton-Photon State', *Phys. Rev. Lett.*, vol. 99, no. 26, Dec. 2007.

[44] A. J. Shields, R. M. Stevenson, and R. J. Young, 'Entangled Photon Generation by Quantum Dots', in *Single Semiconductor Quantum Dots*, P. Michler, Ed. Berlin, Heidelberg: Springer Berlin Heidelberg, 2009, pp. 227–265.

[45] R. J. Young *et al.*, 'Inversion of exciton level splitting in quantum dots', *Phys Rev B*, vol. 72, no. 11, p. 113305, Sep. 2005.

[46] R. J. Young, 'Controlling the fine structure splitting in single InAs quantum dots', University of Cambridge, 2005.

[47] A. J. Bennett *et al.*, 'Electric-field-induced coherent coupling of the exciton states in a single quantum dot', *Nat. Phys.*, vol. 6, no. 12, pp. 947–950, Dec. 2010.

[48] R. Trotta *et al.*, 'Universal Recovery of the Energy-Level Degeneracy of Bright Excitons in InGaAs Quantum Dots without a Structure Symmetry', *Phys. Rev. Lett.*, vol. 109, no. 14, Oct. 2012.

[49] R. Trotta, J. Martín-Sánchez, I. Daruka, C. Ortix, and A. Rastelli, 'Energy-Tunable Sources of Entangled Photons: A Viable Concept for Solid-State-Based Quantum Relays', *Phys. Rev. Lett.*, vol. 114, no. 15, Apr. 2015.

[50] D. Su *et al.*, 'Tuning exciton energy and fine-structure splitting in single InAs quantum dots by applying uniaxial stress', *AIP Adv.*, vol. 6, no. 4, p. 45204, Apr. 2016.

[51] T. Kuroda *et al.*, 'Symmetric quantum dots as efficient sources of highly entangled photons: Violation of Bell's inequality without spectral and temporal filtering', *Phys. Rev. B*, vol. 88, no. 4, Jul. 2013.

[52] C. L. Salter, R. M. Stevenson, I. Farrer, C. A. Nicoll, D. A. Ritchie, and A. J. Shields, 'An entangled-light-emitting diode', *Nature*, vol. 465, no. 7298, pp. 594–597, Jun. 2010.

[53] Z. Yuan *et al.*, 'Electrically Driven Single-Photon Source', *Science*, vol. 295, no. 5552, p. 102, Jan. 2002.

[54] O. Benson, C. Santori, M. Pelton, and Y. Yamamoto, 'Regulated and entangled photons from a single quantum dot', *Phys. Rev. Lett.*, vol. 84, no. 11, p. 2513, 2000.

[55] J. Zhang *et al.*, 'High yield and ultrafast sources of electrically triggered entangled-photon pairs based on strain-tunable quantum dots', *Nat. Commun.*, vol. 6, p. 10067, Dec. 2015.

[56] W. K. Wootters and W. H. Zurek, 'A single quantum cannot be cloned', *Nature*, vol. 299, no. 5886, pp. 802–803, Oct. 1982.

[57] M. A. Nielsen and I. L. Chuang, *Quantum Computation and Quantum Information*. Cambridge University Press, 2000.

[58] C. H. Bennett, G. Brassard, C. Crépeau, R. Jozsa, A. Peres, and W. K. Wootters, 'Teleporting an unknown quantum state via dual classical and Einstein-Podolsky-Rosen channels', *Phys. Rev. Lett.*, vol. 70, no. 13, p. 1895, 1993.

[59] N. Lütkenhaus, J. Calsamiglia, and K.-A. Suominen, 'Bell measurements for teleportation', *Phys Rev A*, vol. 59, no. 5, pp. 3295–3300, May 1999.

[60] A. K. Ekert, 'Quantum cryptography based on Bell's theorem', *Phys. Rev. Lett.*, vol. 67, no. 6, p. 661, 1991.

[61] H.-K. Lo, X. Ma, and K. Chen, 'Decoy State Quantum Key Distribution', *Phys. Rev. Lett.*, vol. 94, no. 23, Jun. 2005.

[62] Q. Wang, X.-B. Wang, G. Björk, and A. Karlsson, 'Improved practical decoy state method in quantum key distribution with parametric down-conversion source', *Europhys. Lett. EPL*, vol. 79, no. 4, p. 40001, Aug. 2007.

[63] N. Lütkenhaus, 'Security against individual attacks for realistic quantum key distribution', *Phys. Rev. A*, vol. 61, no. 5, p. 52304, 2000.

[64] T. Schmitt-Manderbach *et al.*, 'Experimental Demonstration of Free-Space Decoy-State Quantum Key Distribution over 144 km', *Phys. Rev. Lett.*, vol. 98, no. 1, Jan. 2007.

[65] H. J. Kimble, 'The quantum internet', *Nature*, vol. 453, no. 7198, pp. 1023–1030, Jun. 2008.

[66] R. J. Young *et al.*, 'Inversion of exciton level splitting in quantum dots', *Phys. Rev. B - Condens. Matter Mater. Phys.*, vol. 72, no. 11, 2005.

[67] C. K. Hong, Z. Y. Ou, and L. Mandel, 'Measurement of subpicosecond time intervals between two photons by interference', *Phys. Rev. Lett.*, vol. 59, no. 18, p. 2044, 1987.

[68] A. Kiraz, M. Ehrl, C. Bräuchle, and A. Zumbusch, 'Ultralong coherence times in the purely electronic zero-phonon line emission of single molecules', *Appl. Phys. Lett.*, vol. 85, no. 6, p. 920, 2004.

[69] B. Lounis and M. Orrit, 'Single-photon sources', *Rep. Prog. Phys.*, vol. 68, no. 5, pp. 1129–1179, May 2005.

[70] B. E. A. Saleh and M. C. Teich, 'Wave Optics', in *Fundamentals of Photonics*, John Wiley & Sons, Inc., 2001, pp. 41–79.

[71] D. Bimberg, *Semiconductor Nanostructures*. Springer Berlin Heidelberg, 2008.

[72] A. Berthelot *et al.*, 'Unconventional motional narrowing in the optical spectrum of a semiconductor quantum dot', *Nat. Phys.*, vol. 2, no. 11, pp. 759–764, Nov. 2006.

[73] H. D. Robinson and B. B. Goldberg, 'Light-induced spectral diffusion in single self-assembled quantum dots', *Phys. Rev. B*, vol. 61, no. 8, p. R5086, 2000.

[74] A. Migdall, S. V. Polyakov, J. Fan, and J. C. Bienfang, *Single-Photon Generation and Detection: Physics and Applications*. Elsevier Science, 2013.

[75] R. HANBURY BROWN and R. Q. TWISS, 'A Test of a New Type of Stellar Interferometer on Sirius', *Nature*, vol. 178, no. 4541, pp. 1046–1048, Nov. 1956.

[76] A. J. Hudson, 'Polarisation-entangled photon pairs from the quantum dot biexciton cascade', University of Cambridge, 2008.

[77] A. J. Hudson *et al.*, 'Coherence of an Entangled Exciton-Photon State', *Phys. Rev. Lett.*, vol. 99, no. 26, Dec. 2007.

[78] D. Bouwmeester, J.-W. Pan, K. Mattle, M. Eibl, H. Weinfurter, and A. Zeilinger, 'Experimental quantum teleportation', *Nature*, vol. 390, no. 6660, pp. 575–579, Dec. 1997.

[79] H. de Riedmatten, I. Marcikic, W. Tittel, H. Zbinden, and N. Gisin, 'Quantum interference with photon pairs created in spatially separated sources', *Phys Rev A*, vol. 67, no. 2, p. 22301, Feb. 2003.

[80] T. Legero, T. Wilk, M. Hennrich, G. Rempe, and A. Kuhn, 'Quantum Beat of Two Single Photons', *Phys. Rev. Lett.*, vol. 93, no. 7, Aug. 2004.

[81] R. B. Patel, A. J. Bennett, I. Farrer, C. A. Nicoll, D. A. Ritchie, and A. J. Shields, 'Two-photon interference of the emission from electrically tunable remote quantum dots', *Nat. Photonics*, vol. 4, no. 9, pp. 632–635, Sep. 2010.

[82] E. B. Flagg, A. Muller, S. V. Polyakov, A. Ling, A. Migdall, and G. S. Solomon, 'Interference of Single Photons from Two Separate Semiconductor Quantum Dots', *Phys Rev Lett*, vol. 104, no. 13, p. 137401, Apr. 2010.

[83] P. Gold *et al.*, 'Two-photon interference from remote quantum dots with inhomogeneously broadened linewidths', *Phys Rev B*, vol. 89, no. 3, p. 35313, Jan. 2014.

[84] S. V. Polyakov *et al.*, 'Coalescence of Single Photons Emitted by Disparate Single-Photon Sources: The Example of InAs Quantum Dots and Parametric Down-Conversion Sources', *Phys Rev Lett*, vol. 107, no. 15, p. 157402, Oct. 2011.

[85] A. J. Bennett, R. B. Patel, C. A. Nicoll, D. A. Ritchie, and A. J. Shields, 'Interference of dissimilar photon sources', *Nat Phys*, vol. 5, no. 10, pp. 715–717, Oct. 2009.

[86] J. Nilsson *et al.*, 'Quantum teleportation using a light-emitting diode', *Nat. Photonics*, vol. 7, no. 4, pp. 311–315, Feb. 2013.

[87] T. Legero, T. Wilk, A. Kuhn, and G. Rempe, 'Time-resolved two-photon quantum interference', *Appl. Phys. B*, vol. 77, no. 8, pp. 797–802, Dec. 2003.

[88] J. Houel *et al.*, 'Probing Single-Charge Fluctuations at a GaAs/AlAs Interface Using Laser Spectroscopy on a Nearby InGaAs Quantum Dot', *Phys Rev Lett*, vol. 108, no. 10, p. 107401, Mar. 2012.

[89] J. Nilsson, 'Electrically generated entangled light for optical quantum information applications', Université Blaise Pascal-Clermont-Ferrand II, 2013.

[90] C. Santori, D. Fattal, J. Vuckovic, G. S. Solomon, and Y. Yamamoto, 'Single-photon generation with InAs quantum dots', *New J. Phys.*, vol. 6, no. 1, p. 89, 2004.

[91] R. M. Stevenson *et al.*, 'Quantum teleportation of laser-generated photons with an entangled-light-emitting diode', *Nat. Commun.*, vol. 4, Dec. 2013.

[92] W. Heller, U. Bockelmann, and G. Abstreiter, 'Electric-field effects on excitons in quantum dots', *Phys Rev B*, vol. 57, no. 11, pp. 6270–6273, Mar. 1998.

[93] J. Qiu, J.-H. Shi, Y.-S. Zhang, S.-S. Han, and Y.-Z. Gui, 'Interference of quantum beats in Hong-Ou-Mandel interferometry', *Photon Res*, vol. 3, no. 3, pp. 82–85, Jun. 2015.

[94] N. Gisin, G. Ribordy, W. Tittel, and H. Zbinden, 'Quantum cryptography', *Rev. Mod. Phys.*, vol. 74, no. 1, p. 145, 2002.

[95] V. Scarani, H. Bechmann-Pasquinucci, N. J. Cerf, M. Dušek, N. Lütkenhaus, and M. Peev, 'The security of practical quantum key distribution', *Rev. Mod. Phys.*, vol. 81, no. 3, pp. 1301–1350, Sep. 2009.

[96] E. Lombardi, F. Sciarrino, S. Popescu, and F. De Martini, 'Teleportation of a Vacuum-One-Photon Qubit', *Phys Rev Lett*, vol. 88, no. 7, p. 70402, Jan. 2002.

[97] R. Ursin *et al.*, 'Communications: Quantum teleportation across the Danube', *Nature*, vol. 430, no. 7002, pp. 849–849, Aug. 2004.

[98] X.-M. Jin *et al.*, 'Experimental free-space quantum teleportation', *Nat Photon*, vol. 4, no. 6, pp. 376–381, Jun. 2010.

[99] J. Yin *et al.*, 'Quantum teleportation and entanglement distribution over 100-kilometre free-space channels', *Nature*, vol. 488, no. 7410, pp. 185–188, Aug. 2012.

[100] X.-S. Ma *et al.*, 'Quantum teleportation over 143 kilometres using active feed-forward', *Nature*, vol. 489, no. 7415, pp. 269–273, Sep. 2012.

[101] F. Bussières *et al.*, 'Quantum teleportation from a telecom-wavelength photon to a solid-state quantum memory', *Nat Photon*, vol. 8, no. 10, pp. 775–778, Oct. 2014.

[102] T. M. Graham, H. J. Bernstein, T.-C. Wei, M. Junge, and P. G. Kwiat, 'Superdense teleportation using hyperentangled photons', *Nat. Commun.*, vol. 6, p. 7185, May 2015.

[103] R. Valivarthi *et al.*, 'Quantum teleportation across a metropolitan fibre network', *Nat. Photonics*, vol. 10, no. 10, pp. 676–680, Sep. 2016.

[104] K. Azuma, K. Tamaki, and H.-K. Lo, 'All-photonic quantum repeaters', *Nat. Commun.*, vol. 6, p. 6787, Apr. 2015.

[105] H.-J. Briegel, W. Dür, J. I. Cirac, and P. Zoller, 'Quantum repeaters: the role of imperfect local operations in quantum communication', *Phys. Rev. Lett.*, vol. 81, no. 26, p. 5932, 1998.

[106] D. Collins, N. Gisin, and H. De Riedmatten *, 'Quantum relays for long distance quantum cryptography', *J. Mod. Opt.*, vol. 52, no. 5, pp. 735–753, Mar. 2005.

[107] B. C. Jacobs, T. B. Pittman, and J. D. Franson, 'Quantum relays and noise suppression using linear optics', *Phys Rev A*, vol. 66, no. 5, p. 52307, Nov. 2002.

[108] H. de Riedmatten, I. Marcikic, W. Tittel, H. Zbinden, D. Collins, and N. Gisin, 'Long Distance Quantum Teleportation in a Quantum Relay Configuration', *Phys Rev Lett*, vol. 92, no. 4, p. 47904, Jan. 2004.

[109] H.-K. Lo and H. F. Chau, 'Unconditional Security of Quantum Key Distribution over Arbitrarily Long Distances', *Science*, vol. 283, no. 5410, pp. 2050–2056, 1999.

[110] D. Fattal, E. Diamanti, K. Inoue, and Y. Yamamoto, 'Quantum Teleportation with a Quantum Dot Single Photon Source', *Phys Rev Lett*, vol. 92, no. 3, p. 37904, Jan. 2004.

[111] D. Gottesman and I. L. Chuang, 'Demonstrating the viability of universal quantum computation using teleportation and single-qubit operations', *Nature*, vol. 402, no. 6760, pp. 390–393, Nov. 1999.

[112] M. Koashi, 'Simple security proof of quantum key distribution based on complementarity', *New J. Phys.*, vol. 11, no. 4, p. 45018, Apr. 2009.

[113] H.-K. Lo, H. F. Chau, and M. Ardehali, 'Efficient Quantum Key Distribution Scheme and a Proof of Its Unconditional Security', *J. Cryptol.*, vol. 18, no. 2, pp. 133–165, Apr. 2005.

[114] C. Varnava *et al.*, 'An entangled-LED-driven quantum relay over 1 km', *Npj Quantum Inf.*, vol. 2, p. 16006, Mar. 2016.

[115] G. Brassard and L. Salvail, 'Secret-key reconciliation by public discussion', in *Workshop on the Theory and Application of of Cryptographic Techniques*, 1993, pp. 410–423.

[116] M. Felle *et al.*, 'Interference with a quantum dot single-photon source and a laser at telecom wavelength', *Appl. Phys. Lett.*, vol. 107, no. 13, p. 131106, Sep. 2015.

[117] S. Sanguinetti, M. Henini, M. Grassi Alessi, M. Capizzi, P. Frigeri, and S. Franchi, 'Carrier thermal escape and retrapping in self-assembled quantum dots', *Phys Rev B*, vol. 60, no. 11, pp. 8276–8283, Sep. 1999.

[118] Y. H. Chen, X. L. Ye, and Z. G. Wang, 'Evolution of wetting layer in InAs/GaAs quantum dot system', *Nanoscale Res. Lett.*, vol. 1, no. 1, p. 79, 2006.

[119] P. Alonso-González, B. Alén, D. Fuster, Y. González, L. González, and J. Martínez-Pastor, 'Formation and optical characterization of single InAs quantum dots grown on GaAs nanoholes', *Appl. Phys. Lett.*, vol. 91, no. 16, p. 163104, 2007.

[120] D. Bimberg *et al.*, 'Quantum Dots for Single- and Entangled-Photon Emitters', *IEEE Photonics J.*, vol. 1, no. 1, pp. 58–68, Jun. 2009.

[121] J. Martín-Sánchez *et al.*, 'Single Photon Emission from Site-Controlled InAs Quantum Dots Grown on GaAs(001) Patterned Substrates', *ACS Nano*, vol. 3, no. 6, pp. 1513–1517, Jun. 2009.

[122] N. Ha *et al.*, 'Droplet epitaxial growth of highly symmetric quantum dots emitting at telecommunication wavelengths on InP (111) A', *Appl. Phys. Lett.*, vol. 104, no. 14, p. 143106, 2014.

[123] X. Liu *et al.*, 'Vanishing fine-structure splittings in telecommunication-wavelength quantum dots grown on (111)A surfaces by droplet epitaxy', *Phys. Rev. B*, vol. 90, no. 8, Aug. 2014.

[124] N. Koguchi, S. Takahashi, and T. Chikyow, 'New MBE growth method for InSb quantum well boxes', *J. Cryst. Growth*, vol. 111, no. 1–4, pp. 688–692, 1991.

[125] Z. M. Wang, *Nanodroplets*. Springer New York, 2014.

[126] C. Heyn, A. Stemmann, A. Schramm, H. Welsch, W. Hansen, and Á. Nemcsics, 'Regimes of GaAs quantum dot self-assembly by droplet epitaxy', *Phys. Rev. B*, vol. 76, no. 7, Aug. 2007.

[127] A. P. Alivisatos, 'Semiconductor Clusters, Nanocrystals, and Quantum Dots', *Science*, vol. 271, no. 5251, pp. 933–937, Feb. 1996.

[128] J. Li and Wang, 'Shape Effects on Electronic States of Nanocrystals', *Nano Lett.*, vol. 3, no. 10, pp. 1357–1363, Oct. 2003.

[129] A. Stemmann, C. Heyn, T. Köppen, T. Kipp, and W. Hansen, 'Local droplet etching of nanoholes and rings on GaAs and AlGaAs surfaces', *Appl. Phys. Lett.*, vol. 93, no. 12, p. 123108, 2008.

[130] D. Fuster, Y. González, and L. González, 'Fundamental role of arsenic flux in nanohole formation by Ga droplet etching on GaAs (001)', *Nanoscale Res. Lett.*, vol. 9, no. 1, p. 1, 2014.

[131] X. Li *et al.*, 'Origin of nanohole formation by etching based on droplet epitaxy', *Nanoscale*, vol. 6, no. 5, p. 2675, 2014.

[132] Z. M. Wang, K. Holmes, Y. I. Mazur, K. A. Ramsey, and G. J. Salamo, 'Self-organization of quantum-dot pairs by high-temperature droplet epitaxy', *Nanoscale Res. Lett.*, vol. 1, no. 1, pp. 57–61, Nov. 2006.

[133] Z. M. Wang, B. L. Liang, K. A. Sablon, and G. J. Salamo, 'Nanoholes fabricated by self-assembled gallium nanodrill on GaAs(100)', *Appl. Phys. Lett.*, vol. 90, no. 11, p. 113120, 2007.

[134] C. Heyn and Jesson, D. E., 'Congruent evaporation temperature of molecular beam epitaxy grown GaAs (001) determined by local droplet etching', *Appl. Phys. Lett.*, vol. 107, no. 16, p. 161601, Oct. 2015.

[135] Z. B. Chen *et al.*, 'Preferential nucleation and growth of InAs/GaAs(001) quantum dots on defected sites by droplet epitaxy', *Scr. Mater.*, vol. 69, no. 8, pp. 638–641, Oct. 2013.

[136] G. Costantini, C. Manzano, R. Songmuang, O. G. Schmidt, and K. Kern, 'InAs/GaAs(001) quantum dots close to thermodynamic equilibrium', *Appl. Phys. Lett.*, vol. 82, no. 19, p. 3194, 2003.

[137] D. P. Kumah, S. Shusterman, Y. Paltiel, Y. Yacoby, and R. Clarke, 'Atomic-scale mapping of quantum dots formed by droplet epitaxy', *Nat. Nanotechnol.*, vol. 4, no. 12, pp. 835–838, Dec. 2009.

[138] M. Davanço, C. S. Hellberg, S. Ates, A. Badolato, and K. Srinivasan, 'Multiple time scale blinking in InAs quantum dot single-photon sources', *Phys. Rev. B*, vol. 89, no. 16, Apr. 2014.

[139] A. Lyamkina, D. Dmitriev, Y. G. Galitsyn, V. Kesler, S. Moshchenko, and A. Toropov, 'The Investigation of Intermediate Stage of Template Etching with Metal Droplets by Wetting Angle Analysis on (001) GaAs Surface', *Nanoscale Res Lett*, vol. 6, no. 1, p. 42, 2010.

[140] P. Frigeri *et al.*, 'Effects of the quantum dot ripening in high-coverage InAs/GaAs nanostructures', *J. Appl. Phys.*, vol. 102, no. 8, p. 83506, 2007.

[141] M. B. Ward *et al.*, 'Coherent dynamics of a telecom-wavelength entangled photon source', *Nat. Commun.*, vol. 5, Feb. 2014.

[142] C. L. Salter, 'Development and application of an entangled-light-emitting-diode', University of Cambridge, 2010.

[143] R. J. Young, R. M. Stevenson, A. J. Hudson, C. A. Nicoll, D. A. Ritchie, and A. J. Shields, 'Bell-Inequality Violation with a Triggered Photon-Pair Source', *Phys. Rev. Lett.*, vol. 102, no. 3, Jan. 2009.

[144] N. Ha *et al.*, 'Size-dependent line broadening in the emission spectra of single GaAs quantum dots: Impact of surface charge on spectral diffusion', *Phys. Rev. B*, vol. 92, no. 7, Aug. 2015.

[145] K. Kuroda *et al.*, 'Distribution of exciton emission linewidth observed for GaAs quantum dots grown by droplet epitaxy', *J. Lumin.*, vol. 130, no. 12, pp. 2390–2393, Dec. 2010.

[146] T. Mano *et al.*, 'Ultra-narrow emission from single GaAs self-assembled quantum dots grown by droplet epitaxy', *Nanotechnology*, vol. 20, no. 39, p. 395601, Sep. 2009.

[147] M. Benyoucef *et al.*, 'Single-photon emission from single InGaAs/GaAs quantum dots grown by droplet epitaxy at high substrate temperature', *Nanoscale Res. Lett.*, vol. 7, no. 1, pp. 1–5, 2012.

[148] L. Besombes, K. Kheng, L. Marsal, and H. Mariette, 'Acoustic phonon broadening mechanism in single quantum dot emission', *Phys. Rev. B*, vol. 63, no. 15, Mar. 2001.

[149] B. Urbaszek *et al.*, 'Temperature-dependent linewidth of charged excitons in semiconductor quantum dots: Strongly broadened ground state transitions due to acoustic phonon scattering', *Phys. Rev. B*, vol. 69, no. 3, Jan. 2004.

[150] S. Rudin, T. L. Reinecke, and M. Bayer, 'Temperature dependence of optical linewidth in single InAs quantum dots', *Phys. Rev. B*, vol. 74, no. 16, Oct. 2006.

[151] M. J. Holmes, K. Choi, S. Kako, M. Arita, and Y. Arakawa, 'Room-Temperature Triggered Single Photon Emission from a III-Nitride Site-Controlled Nanowire Quantum Dot', *Nano Lett.*, vol. 14, no. 2, pp. 982–986, Feb. 2014.

[152] M. Reischle *et al.*, 'Electrically pumped single-photon emission in the visible spectral range up to 80 K', *Opt Express*, vol. 16, no. 17, pp. 12771–12776, Aug. 2008.

[153] X. M. Dou *et al.*, 'Single-photon-emitting diode at liquid nitrogen temperature', *Appl. Phys. Lett.*, vol. 93, no. 10, 2008.

[154] R. P. Mirin, 'Photon antibunching at high temperature from a single InGaAs/GaAs quantum dot', *Appl. Phys. Lett.*, vol. 84, no. 8, p. 1260, 2004.

[155] Ł. Dusanowski *et al.*, 'Single photon emission up to liquid nitrogen temperature from charged excitons confined in GaAs-based epitaxial nanostructures', *Appl. Phys. Lett.*, vol. 106, no. 23, p. 233107, Jun. 2015.

[156] Ł. Dusanowski *et al.*, 'Single-photon emission of InAs/InP quantum dashes at 1.55 μm and temperatures up to 80 K', *Appl. Phys. Lett.*, vol. 108, no. 16, 2016.

[157] D. Gammon, S. Rudin, T. L. Reinecke, D. S. Katzer, and C. S. Kyono, 'Phonon broadening of excitons in GaAs/AlxGa1−xAs quantum wells', *Phys. Rev. B*, vol. 51, no. 23, pp. 16785–16789, Jun. 1995.

[158] Ł. Dusanowski, A. Musiał, G. Sęk, and P. Machnikowski, 'The Phonon-Assisted Radiative Recombination of Excitons Confined in InAs Quantum Dashes', *Acta Phys. Pol. A*, vol. 124, no. 5, pp. 813–816, Nov. 2013.

[159] S. Moehl, F. Tinjod, K. Kheng, and H. Mariette, 'Reduction of exciton-phonon interaction due to stronger confinement in single quantum dots', *Phys. Rev. B*, vol. 69, no. 24, Jun. 2004.

[160] W. Ouerghui, A. Melliti, M. A. Maaref, and J. Bloch, 'Dependence on temperature of homogeneous broadening of InGaAs/InAs/GaAs quantum dot fundamental transitions', *Phys. E Low-Dimens. Syst. Nanostructures*, vol. 28, no. 4, pp. 519–524, Sep. 2005.

[161] Y. P. Varshni, 'Temperature dependence of the energy gap in semiconductors', *Physica*, vol. 34, no. 1, pp. 149–154, 1967.

[162] G. Gélinas, A. Lanacer, R. Leonelli, R. A. Masut, and P. J. Poole, 'Carrier thermal escape in families of InAs/InP self-assembled quantum dots', *Phys. Rev. B*, vol. 81, no. 23, Jun. 2010.

[163] Z. Y. Xu *et al.*, 'Thermal activation and thermal transfer of localized excitons in InAs self-organized quantum dots', *Superlattices Microstruct.*, vol. 23, no. 2, pp. 381–387, 1998.

[164] D. Xiu-Ming *et al.*, 'Single-photon emission at liquid nitrogen temperature from a single InAs/GaAs quantum dot', *Chin. Phys. Lett.*, vol. 25, no. 9, p. 3231, 2008.

[165] J. Skiba-Szymanska *et al.*, 'Universal Growth Scheme for Quantum Dots with Low Fine-Structure Splitting at Various Emission Wavelengths', *Phys Rev Appl.*, vol. 8, no. 1, p. 14013, Jul. 2017.

[166] A. Nysteen, P. Kaer, and J. Mork, 'Proposed Quenching of Phonon-Induced Processes in Photoexcited Quantum Dots due to Electron-Hole Asymmetries', *Phys Rev Lett*, vol. 110, no. 8, p. 87401, Feb. 2013.

[167] S. Bounouar, M. Müller, A. M. Barth, M. Glässl, V. M. Axt, and P. Michler, 'Phonon-assisted robust and deterministic two-photon biexciton preparation in a quantum dot', *Phys. Rev. B*, vol. 91, no. 16, Apr. 2015.

[168] M. Bayer and A. Forchel, 'Temperature dependence of the exciton homogeneous linewidth in InGaAs/GaAs self-assembled quantum dots', *Phys Rev B*, vol. 65, no. 4, p. 41308, Jan. 2002.

[169] I. Favero *et al.*, 'Temperature dependence of the zero-phonon linewidth in quantum dots: An effect of the fluctuating environment', *Phys Rev B*, vol. 75, no. 7, p. 73308, Feb. 2007.

[170] K. Brunner, G. Abstreiter, G. Böhm, G. Tränkle, and G. Weimann, 'Sharp-line photoluminescence and two-photon absorption of zero-dimensional biexcitons in a GaAs/AlGaAs structure', *Phys. Rev. Lett.*, vol. 73, no. 8, p. 1138, 1994.

[171] M. Glässl *et al.*, 'Biexciton state preparation in a quantum dot via adiabatic rapid passage: Comparison between two control protocols and impact of phonon-induced dephasing', *Phys. Rev. B*, vol. 87, no. 8, Feb. 2013.

[172] L. Monniello *et al.*, 'Excitation-Induced Dephasing in a Resonantly Driven InAs / GaAs Quantum Dot', *Phys. Rev. Lett.*, vol. 111, no. 2, Jul. 2013.

[173] Y.-J. Wei *et al.*, 'Deterministic and Robust Generation of Single Photons from a Single Quantum Dot with 99.5% Indistinguishability Using Adiabatic Rapid Passage', *Nano Lett.*, vol. 14, no. 11, pp. 6515–6519, Nov. 2014.

[174] A. M. Barth, S. Lüker, A. Vagov, D. E. Reiter, T. Kuhn, and V. M. Axt, 'Fast and selective phonon-assisted state preparation of a quantum dot by adiabatic undressing', *Phys Rev B*, vol. 94, no. 4, p. 45306, Jul. 2016.

[175] R. Winik *et al.*, 'On-demand source of maximally entangled photon-pairs using the biexciton-exciton radiative cascade', *ArXiv170304380 Quant-Ph*, Mar. 2017.

[176] S. Stufler *et al.*, 'Two-photon Rabi oscillations in a single InGaAs/GaAs quantum dot', *Phys. Rev. B*, vol. 73, no. 12, Mar. 2006.

[177] R. Keil *et al.*, 'Solid-state ensemble of highly entangled photon sources at rubidium atomic transitions', *ArXiv E-Print*, 2016.

[178] D. Huber *et al.*, 'Highly indistinguishable and strongly entangled photons from symmetric GaAs quantum dots', *ArXiv E-Print*, 2016.

[179] A. V. Kuhlmann *et al.*, 'A dark-field microscope for background-free detection of resonance fluorescence from single semiconductor quantum dots operating in a set-and-forget mode', *Rev. Sci. Instrum.*, vol. 84, no. 7, 2013.

[180] Y.-M. He *et al.*, 'On-demand semiconductor single-photon source with near-unity indistinguishability', *Nat. Nanotechnol.*, vol. 8, no. 3, pp. 213–217, Feb. 2013.

[181] J. H. Quilter *et al.*, 'Phonon-Assisted Population Inversion of a Single InGaAs / GaAs Quantum Dot by Pulsed Laser Excitation', *Phys. Rev. Lett.*, vol. 114, no. 13, Mar. 2015.

[182] P.-L. Ardelt *et al.*, 'Dissipative preparation of the exciton and biexciton in self-assembled quantum dots on picosecond time scales', *Phys. Rev. B*, vol. 90, no. 24, Dec. 2014.

[183] T. H. Stievater *et al.*, 'Rabi Oscillations of Excitons in Single Quantum Dots', *Phys Rev Lett*, vol. 87, no. 13, p. 133603, Sep. 2001.

[184] J. R. Schaibley *et al.*, 'Direct detection of time-resolved Rabi oscillations in a single quantum dot via resonance fluorescence', *Phys Rev B*, vol. 87, no. 11, p. 115311, Mar. 2013.

[185] P. Machnikowski, 'Two-photon processes in quantum dots: biexciton Rabi oscillations and exciton polarization flipping', *Phys. Status Solidi C*, vol. 5, no. 7, pp. 2486–2489, 2008.

[186] P. Machnikowski, 'Theory of two-photon processes in quantum dots: Coherent evolution and phonon-induced dephasing', *Phys Rev B*, vol. 78, no. 19, p. 195320, Nov. 2008.

[187] J. M. Villas-Bôas, S. E. Ulloa, and A. O. Govorov, 'Decoherence of Rabi Oscillations in a Single Quantum Dot', *Phys Rev Lett*, vol. 94, no. 5, p. 57404, Feb. 2005.

[188] Q. Q. Wang *et al.*, 'Decoherence processes during optical manipulation of excitonic qubits in semiconductor quantum dots', *Phys Rev B*, vol. 72, no. 3, p. 35306, Jul. 2005.

[189] B. Patton, U. Woggon, and W. Langbein, 'Coherent Control and Polarization Readout of Individual Excitonic States', *Phys Rev Lett*, vol. 95, no. 26, p. 266401, Dec. 2005.

[190] A. J. Ramsay *et al.*, 'Damping of Exciton Rabi Rotations by Acoustic Phonons in Optically Excited InGaAs / GaAs Quantum Dots', *Phys. Rev. Lett.*, vol. 104, no. 1, Jan. 2010.

[191] A. Krügel, V. M. Axt, T. Kuhn, P. Machnikowski, and A. Vagov, 'The role of acoustic phonons for Rabi oscillations in semiconductor quantum dots', *Appl. Phys. B*, vol. 81, no. 7, pp. 897–904, 2005.

[192] M. E. Reimer *et al.*, 'Overcoming power broadening of the quantum dot emission in a pure wurtzite nanowire', *Phys Rev B*, vol. 93, no. 19, p. 195316, May 2016.

[193] J. Förstner, C. Weber, J. Danckwerts, and A. Knorr, 'Phonon-Assisted Damping of Rabi Oscillations in Semiconductor Quantum Dots', *Phys Rev Lett*, vol. 91, no. 12, p. 127401, Sep. 2003.

[194] H. Jayakumar, A. Predojević, T. Huber, T. Kauten, G. S. Solomon, and G. Weihs, 'Deterministic Photon Pairs and Coherent Optical Control of a Single Quantum Dot', *Phys. Rev. Lett.*, vol. 110, no. 13, Mar. 2013.

[195] M. Müller, S. Bounouar, K. D. Jöns, M. Glässl, and P. Michler, 'On-demand generation of indistinguishable polarization-entangled photon pairs', *Nat. Photonics*, vol. 8, no. 3, pp. 224–228, Feb. 2014.

APPENDIX

Chapter 4

States	Secure key rate (one way error correction)
6-state protocol [17] states: [H,V,D,A,L,R]	-1.38
6-state protocol [18] states: [HA,HD,VA,VD,L,R]	-1.67
4-state protocol [19] states: [H,V,D,A]	**-0.37**
4-state protocol [19] states: [HA,HD,VA,VD]	-0.67

A- 1: Secure key rate extracted from the preliminary quantum teleportation results using the various quantum relay protocols and their input states that were considered for the quantum relay implementation. The secure key rate is based on one-way error correction, as in the actual experiment. The highest secure key rate was obtained for the 4-state protocol with input states H,V,D & A. (The negative values indicate that the average fidelity was lower from these tests than from the relay results).

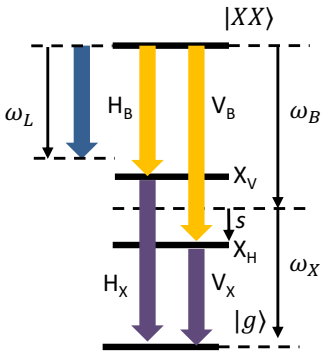

A-2: From [114]. Energy level diagram with the energy transitions and states of the biexciton system cascade. The frequencies of the photons (laser, exciton, biexciton) are denoted by ω. From [114].

Theoretical analysis by R. M. Stevenson, from [114]: The calculation of the time-dependent $g^{(3)}$ correlations takes the experiment schematic in A-2 into account. The notation for the laser and quantum dot states has the form of:

$$\psi_j = A_j(t_j)C_j(t_j)\left|\Psi_j(t_j)\right\rangle$$

where $A_j(t_j)$ is the time dependent real amplitude, $C_j(t_j)$ is the overall phase, and $|\Psi_j(t_j)\rangle$ the polarisation, and any polarisation dependent phase. The overall phase term is further defined as

$$C_j(t_j) = e^{i\omega_j t_j} e^{i\phi_j(t_j)}$$

The first exponent is coherent, and contributes to the final solutions only through detuning of ω_j to the primary frequencies ω_B and ω_X. Decoherence is represented by random fluctuations of the phase ϕ_j as a function of time t_j, such that $e^{i[\phi_j(t_j)-\phi_j(t_j+\Delta)]} = e^{-\frac{|\Delta|}{T_j}}$, where T_j is the coherence time of photon j [9], [87].

The laser input state polarization is defined by real parameters *a* and *b*:

$$\psi_L = A_L(t_L)C_L(t_L)|\Psi_L\rangle$$
$$\Psi_L = \cos(a)\,|H\rangle + e^{ib}\sin(a)\,|V\rangle$$

The QD photon pairs are represented by:

$$\psi_{BX} = A_{BX}(t_B, t_X)C_B(t_B)C_X(t_X)|\Psi_{BX}(t_B, t_X)\rangle$$

The ideal quantum dot biphoton amplitude and state are given by;

$$A_{BXe}(t_B, t_X)$$

$$and\ \Psi_{BXe} = \left(e^{is(t_X-t_B)}|HH\rangle + e^{-is(t_X-t_B)}|VV\rangle\right)/\sqrt{2}$$

In practice however, the emission from the quantum dot is partially mixed. We approximate this with the amplitude $A_{BXu}(t_B, t_X)$ and equal mixture of the polarisation states:

$$\Psi_{HH} = e^{is(t_X-t_B)}|HH\rangle$$

$$\Psi_{HV} = e^{is(-t_X-t_B)}|HV\rangle$$

$$\Psi_{HV} = e^{is(t_X+t_B)}|VH\rangle$$

$$\Psi_{HV} = e^{is(-t_X+t_B)}|VV\rangle$$

Finally, terms corresponding to a pair of laser photons, and a single exciton photon, and three photon emission from the quantum dot only are also considered:

$$\psi_{LL} = A_{LL}(t_{L1}, t_{L2})C_L(t_{L1})C_L(t_{L2})|\Psi_L\rangle|\Psi_L\rangle$$
$$\psi_X = A_X(t_X)C_X(t_X)|X(t_X)\rangle$$
$$\psi_{BBX} = A_{BBX}(t_{B1}, t_{B2}t_X)C_B(t_{B1})C_B(t_{B2})C_X(t_X)|\Psi_{BBX}(t_{B1}, t_{B2}, t_X)\rangle$$

Field amplitude at detectors

The joint amplitude of the electric field at the three photon detectors $|Z\rangle$ is given by the following equation, where four-photon contributions and higher are disregarded due to their relatively small probability compared to three-photon events.

$$Z(t_1,t_2,t_3) = \langle H|\psi_L(t_1)\rangle\langle VQ|\psi_{BX}(t_2,t_3)\rangle + \langle V|\psi_L(t_2)\rangle\langle HQ|\psi_{BX}(t_1,t_3)\rangle + \langle HV|\psi_{LL}(t_1,t_2)\rangle\langle Q|\psi_X(t_3)\rangle + \langle HVQ|\psi_{BBX}(t_1,t_2,t_3)\rangle$$

The first two terms are the desired three-photon amplitudes originating from a single laser, biexciton, and exciton photon. The third and fourth terms originate from two laser photons plus one exciton photon, and two biexciton photons plus one exciton photon respectively.

The intensity of the 3-photon field given by $Z(t_1,t_2,t_3)Z^*(t_1,t_2,t_3)$ is integrated over the arrival of the exciton photon t_3. The following substitutions are made:

$$\eta_j I_j(t_j) = A_j^2(t_j)$$

$$\eta_j\eta_k g_{jk}^{(2)}(t_j,t_k) = A_{jk}^2(t_j,t_k)$$

$$\eta_j\eta_k\eta_l g_{jkl}^{(3)}(t_j,t_k,t_l) = A_{jkl}^2(t_j,t_k,t_l)$$

where η_j is the time averaged intensity of photon j, and $I_j(t_j)$ the normalised intensity of photon j as a function of time. The final expression for the third order correlation is:

$$\begin{aligned}
g^{(3)}(\tau_2,\tau_3) = {} & \frac{1}{2}\cos^2(a)\sin^2(x)\int_0^p I_L(t-\tau_2)g_{BXe}^{(2)}(t-\tau_3,t)\,dt \\
& + \frac{1}{2}\sin^2(a)\cos^2(x)\int_0^p I_L(t-\tau_3)g_{BXe}^{(2)}(t-\tau_2,t)\,dt \\
& + \frac{1}{4}\sin(2a)\sin(2x)\,e^{\frac{-|\tau_1|}{T_L}}e^{\frac{-|\tau_1|}{T_B}}\times\cos\big((\omega_B-\omega_L)\tau_1 - s(\tau_3+\tau_2)+y+b\big) \\
& \times\int_0^p \sqrt{I_L(t-\tau_2)I_L(t-\tau_3)g_{BXe}^{(2)}(t-\tau_2,t)g_{BXe}^{(2)}(t-\tau_3,t)}\,dt \\
& + \frac{1}{4}\cos^2(a)\int_0^p I_L(t-\tau_2)g_{BXu}^{(2)}(t-\tau_3,t)\,dt \\
& + \frac{1}{4}\sin^2(a)\int_0^p I_L(t-\tau_3)g_{BXu}^{(2)}(t-\tau_2,t)\,dt \\
& + \frac{\eta_L}{\eta_B}\frac{1}{4}\cos^2(a)\sin^2(a)\int_0^p I_{LL}^{(2)}(t-\tau_2,t-\tau_3)I_X(t)\,dt \\
& + \frac{\eta_B}{\eta_L}\int_0^p g_{BBX}^{(3)}(t-\tau_2,t-\tau_3,t)\,dt
\end{aligned}$$

Note the final term containing $g_{BBX}^{(3)}(t-\tau_2,t-\tau_3,t)$ is evaluated from by substitution with chains of two-photon correlations, for different ordering of the two biexciton and one exciton photons. This is justified as detection of the first photon places the system to a well-defined state, which serves as

the starting point for a correlation to a second photon, which after detection again places the system into another well-defined state, which is the starting point with correlation to a third photon.

Chapter 6

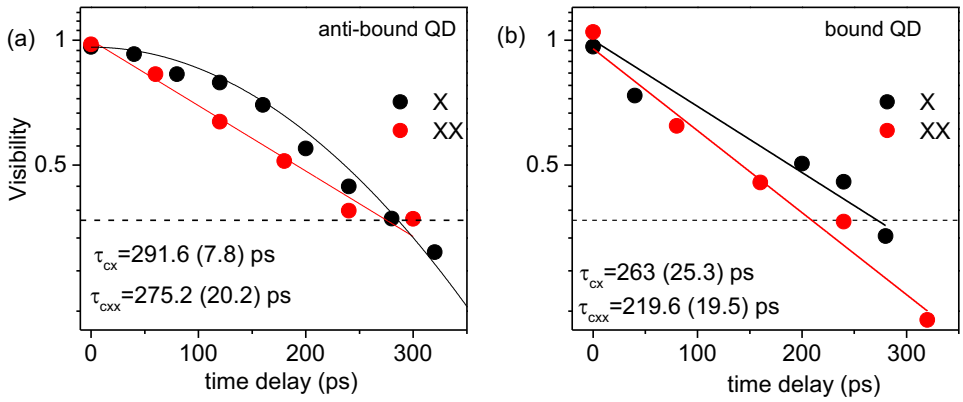

A- 3: Coherence time measurements for (a) an S-K anti-bound QD and (b) an S-K bound QD. (a) X: Gaussian fit, XX: exponential decay fit. (b) exponential decay fits.